# Enhancements to the Long Term Evolution (LTE) Standard for Facilitating the Internet of Things (IoT)

by

Naveen Mysore Balasubramanya

M.S., University of Colorado, Boulder, USA, 2010
B.E., The National Institute of Engineering, Mysore, India, 2005

A THESIS SUBMITTED IN PARTIAL FULFILLMENT OF
THE REQUIREMENTS FOR THE DEGREE OF

DOCTOR OF PHILOSOPHY

in

The Faculty of Graduate and Postdoctoral Studies

(Electrical and Computer Engineering)

THE UNIVERSITY OF BRITISH COLUMBIA
(Vancouver)

May 2017

# Abstract

The world is evolving towards an Internet of Things (IoT) where a large number of devices interact to realize different applications that constitute smart electricity grids, intelligent transportation systems, ubiquitous healthcare solutions, etc. Machine Type Communications (MTC) provide the substrate for the connectivity and service mechanisms of these devices. Many services associated with the MTC applications such as smart metering and location tracking require the cellular network as the backbone for communication and are instrumental in driving the growth of the Third Generation Partnership Project (3GPP) Long Term Evolution (LTE)/LTE-Advanced (LTE-A) standards. A substantial number of MTC User Equipment (UE) hosting IoT applications are expected to be low cost, low data rate devices requiring prolonged battery life.

In the downlink, the current LTE/LTE-A standards adopt Discontinuous Reception (DRX) mechanism for power reduction, which requires the UE to wake up periodically to check for a paging message from the base station. The LTE/LTE-A standardization activities have identified that intricate paging decode procedures increase the energy consumption for low complexity MTC UEs, necessitating enhancements to the current mechanisms. This encourages us to investigate novel energy efficient mechanisms for LTE MTC systems. Specifically, we develop DRX with Quick Sleeping Indication (QSI), which enables the MTC UEs to go back to sleep quickly and save power, when there is no impending page from the base sta-

tion. We also design the enhanced Primary Synchronization Signal (ePSS) for faster timing resynchronization, which can be used as QSI for additional improvements in the downlink energy efficiency of MTC UEs in low coverage. Further, LTE/LTE-A standardization activities in the uplink are examining different procedures to reduce UE data retransmissions for improved energy efficiency. To this end, we develop a Maximum Likelihood (ML) based uplink Carrier Frequency Offset (CFO) estimation technique for the LTE/LTE-A base station, which is robust and accurate in low coverage, enhancing the uplink energy efficiency of MTC UEs.

The MTC mechanisms described in this thesis are not only simple to implement, but also require minimal changes to the present LTE/LTE-A standardization framework, promoting smooth integration into the current LTE/LTE-A networks.

# Lay Summary

The Internet is advancing into an extensive, smart platform inter-connecting a variety of devices leading to an Internet of Things (IoT). A significant portion of the IoT devices are expected to be low-cost, low-complexity User Equipment (UE) like sensors and smart meters. Current wireless communication technologies like the Long Term Evolution (LTE) are defining novel Machine Type Communications (MTC) mechanisms to effectively host such devices. In this thesis, we propose enhancements to the power saving mechanism currently adopted for reception by the LTE MTC UEs and present a strategy to reduce UE data retransmissions. Our solutions address battery operated UEs, especially those in low network coverage and result in improved energy efficiency, thus increasing their battery life. Moreover, our enhanced mechanisms can be easily integrated into the current LTE platforms, since they require minimal changes to the present LTE standardization framework.

# Preface

The material presented in this thesis is entirely based on research performed by myself under the supervision of Prof. Lutz Lampe in the Department of Electrical and Computer Engineering (ECE) at the University of British Columbia (UBC), Vancuver, Canada.

The co-authors in my publications, Mr. Gustav Vos and Mr. Steve Bennett, from Sierra Wireless Inc.[1], Richmond, BC, Canada, have assisted me towards the problem formulation and in determining the relevance of the solutions with respect to the ongoing standardization efforts in the Third Generation Partnership Project (3GPP) Long Term Evolution (LTE).

Below is a list of publications related to the work presented in this thesis.

## Publications Related to Chapter 2

- Naveen Mysore Balasubramanya, Lutz Lampe, Gustav Vos, and Steve Bennett, "Introducing quick sleeping using the broadcast channel for 3GPP LTE MTC," *IEEE Globecom Workshops*, 2014, pp. 606-611.

- Naveen Mysore Balasubramanya, Lutz Lampe, Gustav Vos, and Steve Bennett, "DRX with quick sleeping: A novel mechanism for energy-efficient IoT using LTE/LTE-A," *IEEE Internet of Things Journal (Special Issue on Internet of*

[1] `https://www.sierrawireless.com`

*Things Over LTE/LTE-A Network: Theory, Methods, and Case Studies)*, vol. 3, no. 3, pp. 398-407, 2016.

- Naveen Mysore Balasubramanya, Lutz Lampe and Gustav Vos,"Quick Paging Method and Apparatus in LTE, *US Patent App. 14/799513*, filed in 2014.

## Publications Related to Chapter 3

- Naveen Mysore Balasubramanya, Lutz Lampe, Gustav Vos, and Steve Bennett, "On Timing Reacquisition and Enhanced Primary Synchronization Signal (ePSS) Design for Energy Efficient 3GPP LTE MTC," *IEEE Transactions on Mobile Computing*, In print.

- Gustav Vos, Naveen Mysore Balasubramanya, Steve Bennett and Lutz Lampe, "Method and System for providing and using Enhanced Primary Synchronization Signal for LTE," *US Patent App. 15/010, 192*, filed in 2015.

## Publications Related to Chapter 4

- Naveen Mysore Balasubramanya, Lutz Lampe, Gustav Vos, and Steve Bennett, "Low SNR Uplink CFO Estimation for Energy Efficient IoT Using LTE," *IEEE Access (Special Section: The Plethora of Research on the Internet of Things)*, vol. 4, pp. 3936-3950, 2016.

- Naveen Mysore Balasubramanya, Lutz Lampe, Gustav Vos and Steve Bennett,"Method and System for Carrier Frequency Offset Estimation in LTE MTC Device Communication," *US Provisional Patent App. 62/307, 327*, filed in 2016.

# Table of Contents

# List of Tables

# List of Figures

# List of Abbreviations

| | |
|---|---|
| eNB | evolved Node B |
| ePSS | enhanced Primary Synchronization Signal |
| 3GPP | Third Generation Partnership Project |
| 5G | Fifth Generation |
| ARQ | Automatic Repeat reQuest |
| AWGN | Additive White Gaussian Noise |
| BLER | Block Error Rate |
| BPSK | Binary Phase Shift Keying |
| C-RNTI | Connected Mode - Radio Network Temporary Identifier |
| CAT-0 | Category-0 |
| CAT-1 | Category-1 |
| CAT-M1 | Category-M1 |
| CAZAC | Complex Amplitude Zero AutoCorrelation |
| CC | Convolution Coding |
| CCA | Clear Channel Assessment |
| CDF | Cumulative Distribution Function |
| CDMA | Code Division Multiple Access |
| CE | Coverage Enhancement |
| CFO | Carrier Frequency Offset |
| CP | Cyclic Prefix |

| | |
|---|---|
| CQI | Channel Quality Indication |
| CRC | Cyclic Redundancy Checksum |
| CSI | Channel State Information |
| CTC | Convolution Turbo Code |
| D2D | Device-to-Device |
| DCI | Downlink Control Information |
| DFT | Discrete Fourier Transform |
| DMRS | Demodulation Reference Signals |
| DRX | Discontinuous Reception |
| EPA | Extended Pedestrian A |
| ETSI | European Telecommunications Standards Institute |
| FDMA | Frequency Division Multiple access |
| FEC | Forward Error Correction |
| FFT | Fast Fourier Transform |
| GMSK | Gaussian Minimum Shift Keying |
| H-SFN | Hyper - System Frame Number |
| H2H | Human-to-Human |
| ICI | Inter Carrier Interference |
| IEEE | Institute of Electrical and Electronics Engineers |
| IFFT | Inverse Fast Fourier Transform |
| IMSI | International Mobile Subscriber Identity |
| IoT | Internet of Things |
| IP | Internet Protocol |
| ISM | Industrial, Scientific and Medical |
| LAA | Licensed Assisted Access |

| | |
|---|---|
| LBT | Listen Before Talk |
| LC | Low-Cost, Low-Complexity, Low-Coverage |
| LoRa | Long Range |
| LoRaWAN | Long Range Wireless Access Network |
| LOS | Line Of Sight |
| LPWA | Low Power Wide Area |
| LRLP | Long Range Low Power |
| LTE | Long Term Evolution |
| LTE-A | LTE-Advanced |
| LTE-U | LTE-Unlicensed |
| LTN | Low Throughput Network |
| M2M | Machine-to-Machine |
| MAC | Medium Access Control |
| MCS | Modulation and Coding Scheme |
| MIB | Master Information Block |
| MIMO | Multi-Input-Multi-Output |
| ML | Maximum Likelihood |
| MSE | Mean Squared Error |
| MTC | Machine Type Communications |
| MU-MIMO | Multi-User MIMO |
| MUI | Multi-user Interference |
| NB-IoT | Narrowband Internet of Things |
| NLOS | Non Line Of Sight |
| NR | New Radio |
| OFDM | Orthogonal Frequency Division Multiplexing |

| | |
|---|---|
| OFDMA | Orthogonal Frequency Division Multiple Access |
| P-RNTI | Paging - Radio Network Temporary Identifier |
| PBCH | Physical Broadcast Channel |
| PDCCH | Physical Downlink Control Channel |
| PDSCH | Physical Downlink Shared Channel |
| PHICH | Physical Hybrid ARQ Indicator Channel |
| PO | Paging Occasion |
| PRACH | Physical Random Access Channel |
| PRB | Physical Resource Block |
| PSS | Primary Synchronization Signal |
| QAM | Quadrature Amplitude Modulation |
| QoS | Quality of Service |
| QPSK | Quaternary Phase Shift Keying |
| QSI | Quick Sleeping Indication |
| RACH | Random Access Channel |
| RAN-1 | Radio Access network - Layer 1 |
| RE | Resource Element |
| RNC | Radio Network Controller |
| RNTI | Radio Network Temporary Identifier |
| RRC | Radio Resource Configuration |
| RV | Redundancy Version |
| S-TMSI | System Architecture Evolution - Temporary Mobile Subscriber Identity |
| SC-FDMA | Single Carrier - Frequency Division Multiple Access |
| SFN | System Frame Number |

| | |
|---|---|
| SIB | System Information Block |
| SINR | Signal-to-Interference-plus-Noise Ratio |
| SISO | Single-Input-Single-Output |
| SNR | Signal-to-Noise Ratio |
| SON | Self Organizing Network |
| SSS | Secondary Synchronization Signal |
| TBS | Transport Block Size |
| TTI | Transmit Time Interval |
| UE | User Equipment |
| UEGI | UE Group Indicator |
| UEID | UE Identifier |
| UMTS | Universal Mobile Telecommunications System |
| VCO | Voltage Controlled Oscillator |
| VCTCXO | Voltage Controlled Temperature Compensated Crystal Oscillator |
| WiFi | Wireless Fidelity |
| WiMax | Wireless Interoperability for Microwave Access |
| WLAN | Wireless Local Area Network |
| ZC | Zadoff-Chu |

# Acknowledgments

Firstly, I would like to express my sincere gratitude to my advisor Prof. Lutz Lampe for the continuous support during the course my Ph.D. I thank him for being a patient listener and a constant source of motivation. His knowledge, work ethic and perseverance are truly inspiring and his guidance has helped me in every stage of my research and in the writing of this thesis. I could not have imagined having a better advisor and mentor for my Ph.D work.

Besides my advisor, I would like to thank the rest of my thesis committee: Prof. Victor Leung, Prof. Satish Gopalakrishnan, Prof. Ian Blake and Prof. Cyril Leung, for their time and effort in evaluating my work and providing insightful comments.

My sincere thanks also goes to Mr. Gustav Vos and Mr. Steve Bennett from Sierra Wireless Inc., Richmond, BC, Canada, for their valuable inputs and frequent feedback throughout my Ph.D. research. I would like to thank them for presenting our research in various meetings of the Third Generation Partnership Project (3GPP) Long Term Evolution (LTE) standardization and for their extended support in filing patents from our research.

I am grateful to MITACS, Canada for supporting this research under the MITACS Accelerate Fellowship program with the title “New Carrier Types and Services for Long-term Evolution (LTE) Machine-Type Communication(MTC)”and to the Natural Science and Engineering Research Council of Canada (NSERC) for their support through the Strategic Project Grant ”Technologies for 5G Wireless Systems:

Software-defined Networks, Massive MIMO, and Full Duplexing".

I thank my fellow labmates for the stimulating discussions and all my friends for their encouragement. I would like to thank my family: my parents and my wife, who have been the biggest support pillars of my life, for lovingly, morally and spiritually guiding me towards my goals.

Last but not the least, I would like to thank my idols - Late Dr. A.P.J Abdul Kalam, former president of India and the legendary Indian cricketer Sachin Tendulkar. I have been highly influenced by Dr. Kalam's books, his lifestyle and words of wisdom. Sachin Tendulkar constantly met huge expectations from a billion people with great determination and sustained excellence, inspiring me to never give up and keep chasing my dreams.

# Dedication

To my parents and my wife.

# Chapter 1

# Introduction

The Internet is evolving from connecting computers and dedicated terminals to a quintessential medium that can engulf a plethora of "smart" devices like mobile phones, electronic meters, location sensors, etc. The reducing size of silicon on chip and continuously declining price of components have increased the ease of integration of "smart" sensing and decision-making devices into everyday objects, leading to the emergence of the Internet of Things (IoT). Diverse applications within the IoT umbrella are not only promising to the consumer, but also appealing to researchers across various fields. The IoT relies on advancements in different fields such as communication technologies, microelectronics, data mining, big data handling, etc. Figure 1.1 summarizes the different applications. A brief account of these applications is presented below.

- **Security and public safety** - This category includes applications like home security, building access control, surveillance systems and other public safety mechanisms enabling "smart cities" [1].

- **Tracking** - Numerous applications related to tracking and monitoring are visualized over the IoT ranging from monitoring the status of critical infrastructure (nuclear reactors, transport, bridges, etc.) and industrial fleet management [2] to pet tracking for households, wildlife monitoring and cattle tracking in agriculture [3].

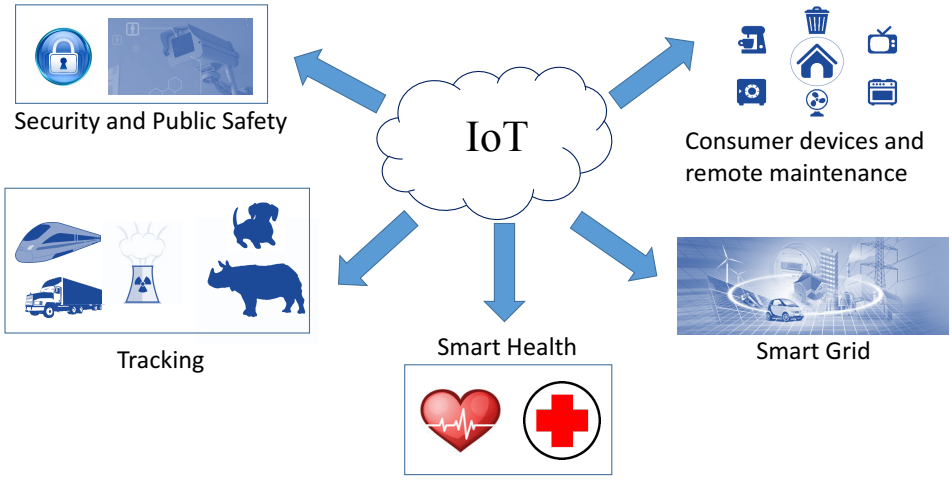


Figure 1.1: IoT applications.

- **Smart grid** - This corresponds to a number of smart applications related to the distribution and management of power, water, gas and heating. Smart metering is an appropriate example in this regard [4].

- **Smart health** - Many applications related to automatic monitoring and tracking of patients, personnel and biomedical devices within hospitals are envisioned under the "smart health" category [5].

- **Consumer devices and remote maintenance** - Another vital application of IoT is in controlling sensors used for vending machine operations, vehicle diagnostics, remote home appliance control, etc. [6].

While some of these applications, like driving the sensors that control a nuclear reactor are critical in terms of the latency and reliability, others like pet/cattle tracking, smart metering can be more delay tolerant. However, the number of devices supporting non-critical applications can be massive [7].

Wireless communications have been a primary candidate in ensuring the connectivity and in satisfying the service requirements of the new, smart devices over the

Internet. The changing landscape of Internet based services has been driving the evolution of wireless communication. As wireless communication technologies step into the Fifth Generation (5G), one of the major challenges faced by them is to effectively support the diverse requirements of the IoT world. Considering the application diversity and the variety of network scenarios envisioned over the IoT platform, it would be difficult to have a single solution to answer the requirements of all the applications.

The need to design efficient mechanisms for the IoT devices is being addressed by different standardization committees. The prominent solutions include the Institute of Electrical and Electronics Engineers (IEEE) 802.15.4 Bluetooth [8, 9] and IEEE 802.11 Wireless Local Area Network (WLAN) [10, 11], which mainly rely on Device-to-Device (D2D) communication and a distributed network architecture. However, these technologies are limited by low coverage and capacity. The support for IoT is also being considered by the Third Generation Partnership Project (3GPP) standardization committee through the Long Term Evolution (LTE)/LTE-Advanced (LTE-A) standards [12]. The LTE/LTE-A standards use the cellular network for enabling long-range operation, but enhancements to the current mechanisms are essential for effectively support the IoT [12].

Recently, heterogeneous networks and small cell base-stations [13, 14] are being deployed to serve regions where the network traffic is high. Although these solutions are successful in managing the network load and improving the user throughput, the additional infrastructure and operational expenses required to realize these solutions are high. IoT solutions also include Self Organizing Networks (SONs), which have the ability to improve the network efficiency by adapting, managing and optimizing their operations based on the network behaviour [15, 16]. However, SONs require

complex algorithms and new network equipment to operate efficiently.

## 1.1 Machine Type Communications (MTC)

A large number of IoT based services such as automated security systems with monitoring and reporting features, pet trackers, agriculture-based applications, etc. are expected to require wireless network access. Moreover, the devices deployed to realize these services are expected to be small sized, cost effective and battery operated. Machine-to-Machine (M2M) or Machine Type Communications (MTC) involves the definition, design and development of communication and service mechanisms that assist in the connectivity of such IoT devices.

The MTC mechanisms face a variety of challenges depending on the application for which the MTC device is being used. These challenges can be completely different from those faced by conventional Human-to-Human (H2H) communication mechanisms. The key challenges to be addressed in MTC are listed below.

### 1.1.1 Challenges in MTC

- **Supporting low data rate, delay tolerant operations** - While the current communication networks are adept at managing the demands of H2H devices, the IoT scenario requires the network to handle MTC devices with contrasting demands. For example, an LTE network that is able to provide a good quality of service to a high data rate, low latency, videoconferencing application over few devices using H2H communication, may not be able to use resources efficiently for serving low data rate, delay tolerant MTC devices deployed for smart meter data reporting.

- **Handling a massive number of devices** - A predominant feature of the IoT is the massive increase in the number of devices requiring network access. For example, it is predicted that the cellular IoT has to grow at an average rate of 35% annually to reach a potential volume of seven billion units by 2025 [17]. Thus, handling massive access, minimizing outage and providing the necessary Quality of Service (QoS) for different categories of devices would be highly challenging.

- **Reducing the energy consumption** - MTC devices do not require to be constantly "connected" or "active", since their data transmission is not continuous and the amount of data to be sent per transmission is small. Furthermore, low-cost and low data rate devices operating with extended battery life (lasting 10 or more years) form a substantial part of the IoT equipment. Therefore, it is important to tune the MTC mechanisms so that the energy consumption of the MTC devices is reduced [18].

- **Improving coverage** - MTC devices may be located in areas where the network coverage is very low, such as basements of buildings, underground parking facilities at malls, interiors of hospitals, etc. For example, MTC devices can be used for medical monitoring, where vital biological parameters of patients such as blood pressure, heart rate and body temperature are sensed and exchanged with a server [19]. The patients have limited mobility within the hospital premises and can be present in a closed, indoor environment where the network requires enhanced coverage to reach them. Due to the restrictions on the total available power and the maximum power allowed for transmission in the channel (arising from the spectral mask constraints), the MTC device cannot arbitrarily increase its transmission power to reach the base-station. This

results in a very low operating Signal-to-Noise Ratio (SNR) at the base station. Therefore, it is necessary to design and develop MTC mechanisms that can enhance the performance of devices in low network coverage areas.

The contributions of this thesis address energy efficiency and improved coverage aspects of the IoT MTC devices.

### 1.1.2 MTC Solutions

In order to drive the IoT, enhanced MTC support is being considered by many current wireless communication technologies. The traditional short-range communication technologies like Bluetooth and ZigBee [8, 9] satisfy the low power requirements of MTC, but have limited coverage and capacity. While WLAN improves the capacity at the expense of power, it falls behind in terms of coverage [10, 11]. Many IoT applications like smart cities, logistics and health require long range of operation. The range of these technologies can be extended using multi-hop mesh networks, relays and gateways. Small-cell based IoT solutions are prominent candidates in this regard, however, they come at the expense of additional cost for network infrastructure/maintenance and backhaul provisioning [20]. The cellular technologies provide the desired range, but have higher power consumption. Therefore, it is essential to have energy efficient, cost-effective solutions addressing the requirements of potentially "hard to reach" devices in the network.

Although there is no consensus on the percentage of such low coverage, low power MTC devices in the network, forecasts indicate that they can be significant. Low Power Wide Area (LPWA) M2M connections are expected grow from 20 million to over 860 million by 2020 [21]. Moreover, smart meters are expected to be the largest LPWA application with a projected share of 45% of the total LPWA connections by

2020 [21]. Furthermore, low cost and extended coverage are considered to be the key features of LPWA technologies [20].

#### 1.1.2.1 Summary of LPWA Technologies

A hallmark of the LPWA networks is that they provide long range communication with reduced power consumption, the desired region of operation for IoT applications like smart meters and tracking. It is evident that the LPWA technologies evolve based on one of the two paths - by increasing the coverage of low power, short-range technologies or by reducing the power of cellular technologies. In this regard, various proprietary LPWA technologies as well as those driven by the standardization committees have emerged.

SIGFOX [22] is a patented LPWA technology that independently or by cooperation with its network partners offers an end-to-end LPWA connectivity solution. It operates in an ultra narrow band, i.e., 100 Hz Sub-GHz Industrial, Scientific and Medical (ISM) band carrier and uses Binary Phase Shift Keying (BPSK) modulation. The proprietary SIGFOX base station consists of cognitive software-defined radio, which is connected to an Internet Protocol (IP) based network at the back-end. The use of the ultra narrow band results in decreased noise levels, improved receiver sensitivity and low cost antenna design. However, the data rate provided is limited to 100 bps. SIGFOX uses unslotted ALOHA as the Medium Access Control (MAC) layer protocol and does not incorporate any encryption or Forward Error Correction (FEC) for the data packets.

Long Range (LoRa) is another prominent, proprietary LPWA technology developed by Semtech Corporation [23]. Similar to SIGFOX, LoRa also operates on the Sub-GHz ISM band and uses an unslotted ALOHA based MAC [24]. But, unlike SIGFOX, it supports data encryption and FEC. For the physical layer, it uses a chirp

spread spectrum technique, which results in noise and interference resilient signals. LoRa offers data rates up to 37.5 kbps. Moreover, the upper layers and the system architecture of LoRa are being standardized by LoRa Alliance under Long Range Wireless Access Network (LoRaWAN) specification [25], which supports different classes of IoT devices based on latency.

Ingenu is an LPWA technology which uses a variant of code division access called the random phase multiple access [26], operates in the ISM 2.4 GHz band and offers data rates up to 68 kbps. Telensa [27] is a candidate similar to SIGFOX. Weightless [28] is another major LPWA technology, operating with three variants - Weightless-W, Weightless-N and Weightless-P. Weightless-W operates in shared TV white-spaces using 16-ary Quadrature Amplitude Modulation (QAM) and differential-BPSK, providing data rates from 1 kbps to 10 Mbps. Weightless-N operates on ultra narrow band, uses differential-BPSK and can achieve data rates up to 1 kbps. Weightless-P uses a narrow band with Gaussian Minimum Shift Keying (GMSK) and Quaternary Phase Shift Keying (QPSK) modulation techniques to provide data rates from 0.2 kbps to 100 kbps.

LPWA has been a regime of interest for distinguished standardization bodies, like the IEEE, the European Telecommunications Standards Institute (ETSI) and the 3GPP. Efforts are in progress for extending the range of IEEE 802.11 standards under the Long Range Low Power (LRLP) topic by the Task Group AH. Although some use cases and functional requirements for the LRLP technology have been defined, the standardization and development activities are in the nascent stage [29]. ETSI aims to standardize an LPWA technology called the Low Throughput Network (LTN), which is bidirectional low data rate communication protocol. Specifications have been defined for the use cases [30], functional architecture [31] and protocols/interfaces [32],

which include the support for user cooperation and ultra narrow-band operation. SIGFOX, Telensa and LoRa are actively involved in standardizing their technologies under ETSI LTN label.

While the aforementioned technologies are from the path of extending the range of short-range communications, the second path of reducing the power of the long range communications has been the mode of development for the 3GPP cellular standardization committee. The leading 3GPP standard in this regard is the LTE/LTE-A, which is expected to occupy more than 75% of the world's cellular market by 2020 [7]. Various improvements to the LTE/LTE-A standard spanning from the network layer to the physical layer are being considered to support the IoT. These include efficient routing protocols, parameterization of transmission and reception mechanisms in terms of packet size, modulation schemes, sleep duration, etc.

This thesis suggests improvements to the MTC mechanisms in the physical layer of the LTE/LTE-A standards to effectively support the IoT. The motivation behind considering physical layer stems from the fact that it is the lower-most layer reflecting the modifications from the higher layers and the first medium of contact for baseband signal processing. Improvements to physical layer is essential to leverage the efficiency of higher layer protocols to host the IoT.

#### 1.1.2.2 MTC in LTE/LTE-A for Facilitating the IoT

With the IoT services emerging as the constitutive driver for the growth of cellular network and MTC assisting the communication mechanisms, 3GPP has initiated the standardization of MTC from Release 11 of the LTE standard. The major advantages of using MTC over the LTE network for IoT are that it uses the existing network infrastructure to serve the devices, thereby reducing the operational costs and it enables the network operator to harness the higher capacity, coverage and ease of

integration aspects of LTE to serve the devices efficiently. For example, it is shown in [33] that LTE offers significant capacity for smart metering even when low-cost devices are used. The results indicate that approximately 2% of the system resources are required to support advanced metering infrastructure in an urban deployment scenario using LTE. Although LTE provides high capacity, the current LTE/LTE-A networks are designed for efficient H2H communications. In order to utilize the high capacity aspects in an efficient manner, the network architecture needs to be revamped to support MTC applications [34–40].

In [34], the MTC network architecture is envisioned with simplified physical and medium access layers that provide sufficient scalability and flexibility for the underlying MTC application. An overview of M2M communications supported by LTE/LTE-A is provided in [35] and a grouping-based radio resource management is proposed to achieve the most critical QoS guarantees for MTC devices. The importance of congestion control and network overload avoidance for a MTC network architecture and potential solutions to address these problems are discussed in [36]. The user scheduling aspects for 3GPP MTC are presented in [37] and a low complexity scheduler using a QoS based clustering algorithm is proposed for MTC. The different application scenarios and the challenges in 3GPP MTC network with respect to massive access, reliable transmission and energy management are summarized in [38]. For the smart metering example mentioned above, the works in [39,40] provide a detailed assessment of the uplink traffic generated by such applications and develop a comprehensive analytical model (inclusive of random access, control and data channels with retransmissions) to determine the meter outages. A downlink group-based paging procedure for smart meters is discussed in [41].

In this thesis, we consider the physical layer aspects of low cost, low power, low

data rate MTC devices in LTE/LTE-A. The 3GPP has identified various categories of MTC devices [17, 42].

- **Category-1 (CAT-1)** - This category exists from the initial release of LTE (Release 8). A CAT-1 User Equipment (UE) can support date rates up to 10 Mbps in the downlink and 5 Mbps in the uplink with a maximum bandwidth of 20 MHz.

- **Category-0 (CAT-0)** - Release 12 of the LTE standard introduced CAT-0 UEs, which support a maximum data rate of 1 Mbps in both the downlink and the uplink, since the modulation is restricted to QPSK. This was the first step by 3GPP towards improving the support for low data rate IoT devices. The CAT-0 UE still supports bandwidths up to 20 MHz. However, the complexity of CAT-0 UEs is reduced to 50% of CAT-1 UEs.

- **Category-M1 (CAT-M1)** - The first reduced-bandwidth device category introduced by the 3GPP is the CAT-M1, introduced in Release 13 of the LTE/LTE-A standards. A CAT-M1 UE has a bandwidth of 1.4 MHz, which the lowest possible bandwidth supported by traditional LTE standards. A CAT-M1 UE has 75-80% reduction in complexity when compared to CAT-1 UEs and supports data rates up to 1 Mbps.

- **Narrowband Internet of Things (NB-IoT)** - Release 13 of the LTE/LTE-A standards also introduced the first narrowband device category in the form of NB-IoT. An NB-IoT UE occupies a bandwidth of 180 kHz and supports data rates up to 0.2 Mbps.

In addition to the support for different categories of MTC UEs, MTC UE operation with Coverage Enhancement (CE) is recognized as a "work item" in Release 13

of the LTE standard, aiming to provide 12 dB to 20 dB of additional coverage [43,44]. Moreover, the LTE/LTE-A standardization activities have identified that improvements to the current power saving mechanisms are necessary for efficient operation of MTC UE intending to support the IoT. In this thesis, we focus on suggesting enhancements to the Discontinuous Reception (DRX) mechanism, which is used for reduced power consumption in the downlink and the NB-IoT transmission mechanism in the uplink [45–48].

### 1.1.3 Thesis Outline and Major Contributions

The objective of our research is to provide mechanisms in the downlink and the uplink for facilitating the IoT using 3GPP LTE MTC. Our solutions are designed such that the changes required to the current LTE/LTE-A framework are kept minimal. In the following, we provide an outline of the thesis, highlighting the major contributions.

The rest of this chapter is organized as follows. In Section 1.2, we provide the essential background on the DRX and the NB-IoT mechanisms in LTE. This is followed by a review of the prior works on power saving modes in the downlink and energy efficient transmission mechanisms in the uplink in Section 1.3. Chapter 2 and Chapter 3 focus on energy efficient mechanisms for MTC UEs in the downlink, while Chapter 4 concentrates on such mechanisms in the uplink.

The LTE/LTE-A standardization activities have recognized that the current DRX mechanism is not entirely efficient for MTC UEs, since it requires the UEs to periodically check for the paging information, which is computationally intensive and power consuming. In Chapter 2, we propose a modified DRX mechanism incorporating quick sleeping for energy efficient IoT using LTE/LTE-A [49–51]. Our contributions in this regard involve the design of DRX with quick sleeping indication techniques

for two categories of low-mobility MTC UEs - a) normal coverage and b) extended coverage. For the former case, we develop the solutions by utilizing the existing resources on the physical downlink synchronization and the broadcast channels. For the latter case, we identify that in addition to the paging decode process, the UE resynchronization in the downlink also increases the power consumption. To alleviate this problem, we develop solutions using dedicated resources on the physical downlink data channel, ensuring that the resource overhead is minimal.

In Chapter 3, we explore the impact of timing reacquisition on the MTC UE energy consumption in greater detail. We demonstrate that legacy methods for resynchronization in Orthogonal Frequency Division Multiplexing (OFDM) systems using Cyclic Prefix (CP) autocorrelation and reference signal detection are not effective for the low complexity MTC UEs requiring extended coverage. Our main achievement in this chapter is design of the enhanced Primary Synchronization Signal (ePSS); a new signal aiding fast resynchronization and improved energy efficiency of the UE in the downlink [52,53]. In the process, we also designed a new DRX mechanism, which uses the ePSS as a quick sleeping mechanism, enabling us to harness the benefits of both faster reacquisition and simplified paging decode for further improvement in the energy efficiency of the MTC UEs.

Chapter 4 considers the MTC mechanisms under low network coverage for energy efficient uplink transmission in the realm of NB-IoT. We illustrate that the reduction in residual Carrier Frequency Offset (CFO) improves data decoding at the base station, which results in a reduction in the number of data retransmissions, thereby reducing the energy consumption of the UEs. Our major contribution in this chapter is to develop a maximum likelihood based CFO estimation mechanism for NB-IoT uplink, which works robustly in low coverage [54, 55]. We also demonstrate that the

performance of the large transport block transmission scheme (a novel technique being considered by 3GPP for improved uplink data rates) is further improved when used along with our proposed CFO estimation technique.

Finally, the conclusions and potential avenues for further research are presented in Chapter 5.

## 1.2 Background

### 1.2.1 DRX and Paging Mechanism in LTE/LTE-A

In the DRX mode of operation, the UE follows a periodic cycle called the DRX cycle involving sleep intervals and wake-up intervals. The current LTE/LTE-A standards support different DRX cycle lengths with a maximum length of 2.56 s. Recently, extended DRX cycle lengths starting from 5.12 s to a maximum of 2621.44 s have been approved by the 3GPP [56]. In this section, we review the DRX and paging decode mechanisms in the current LTE/LTE-A standards.

#### 1.2.1.1 Current Paging Reception Mechanism for UE in DRX

The paging information in LTE/LTE-A consists of the control part and the data part. The control information for an upcoming paging block is indicated to the UE by a Physical Downlink Control Channel (PDCCH) containing the Paging - Radio Network Temporary Identifier (P-RNTI). This is followed by the paging data on the Physical Downlink Shared Channel (PDSCH). The paging data consists of a list of the System Architecture Evolution - Temporary Mobile Subscriber Identity (S-TMSI) or the International Mobile Subscriber Identity (IMSI) of the UEs being paged. If the UE successfully decodes a PDCCH with P-RNTI and the paging block on PDSCH

and finds its S-TMSI or IMSI in the paging list, then it stays awake to decode an impending data transmission. Otherwise, it goes back to sleep.

For decoding the PDCCH, the UE requires a Discrete Fourier Transform (DFT) whose size corresponds to the base station (called the evolved Node B (eNB) in LTE) bandwidth. The UE also incorporates a blind decoding scheme where it hypothesizes over 44 options of PDCCH locations [57, 58]. This renders the PDCCH decoding procedure to be computationally intensive and power consuming. The 3GPP standardization committee is in the process of defining a new control channel for the low-cost, low-complexity devices so that the number of blind decodes required to detect the paging identifier on the control channel is reduced [56]. But the process of looking for a page in each wake-up cycle is still retained.

#### 1.2.1.2 DRX Modes Supported in LTE/LTE-A

The LTE/LTE-A standard supports two variants of DRX - a) Connected Mode DRX and b) Idle Mode DRX [57,59,60]. These modes are categorized based on the handling of the Radio Resource Configuration (RRC) connection. In the Connected Mode DRX, the UE does not relinquish the RRC connection for the entire duration of the DRX cycle and in the Idle Mode DRX, the UE releases the RRC connection before it goes back to sleep.

In Connected Mode DRX, the ON time of the UE is 100 ms typically. LTE subframes are 1 ms long and PDCCH is sent every subframe (see Figure 1.2). Hence, the UE monitors PDCCH for 100 subframes and a valid PDCCH is received on only one subframe [57, 59]. Such a mechanism is beneficial to the UEs that receive a valid PDCCH early during their ON time. They can process the paging information, go back to sleep quicker and save power.

In the Idle Mode DRX, each UE checks for PDCCH periodically, albeit only in

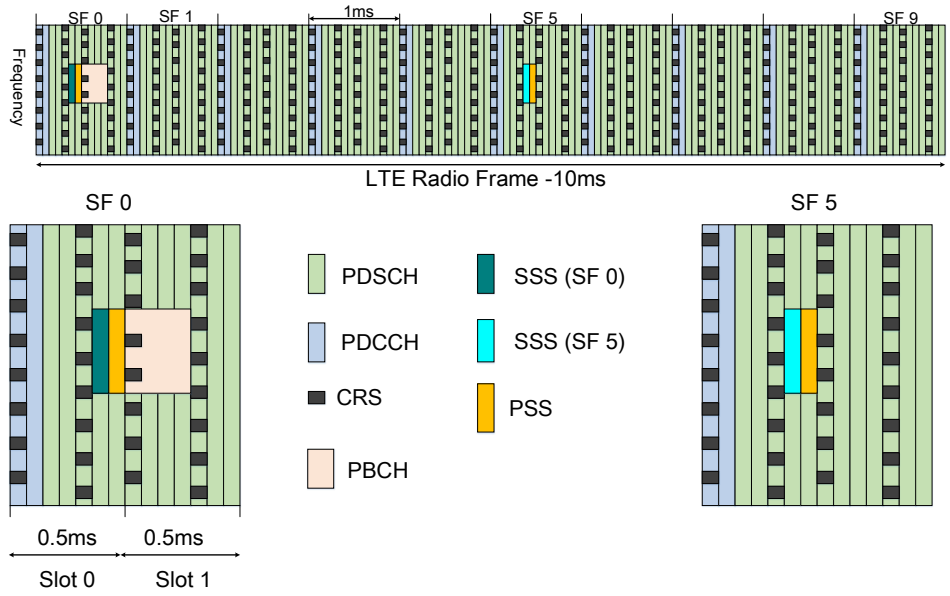


(a) Physical channels

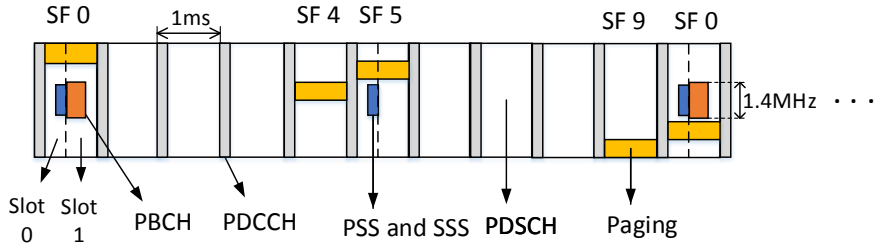


(b) Physical channels with paging blocks

Figure 1.2: LTE radio frame structure showing the different physical channels and paging transmission.

one pre-assigned subframe per DRX cycle called the Paging Occasion (PO) [60]. The PO subframe number is determined based on the UE Identifier (UEID) [60] and it can be either subframe 0, 4, 5 or 9 as shown in Figure 1.2. This can provide significant power savings compared to the Connected Mode DRX. Ideally, it can reduce the ON time of the UE to just 1 ms if the SNR is good and if the timing synchronization of the UE is so accurate that it can wake up exactly at the PO. However in practice, the Voltage Controlled Oscillator (VCO) used for the UE clock will possess a drift

that can affect the symbol timing accuracy and SNR may not always be favourable. If the subframe timing is not accurate, the UE will have to re-acquire it using the Primary Synchronization Signal (PSS) and the Secondary Synchronization Signal (SSS). Similarly, if the frame timing is lost, the UE will have to reacquire frame synchronization by decoding the System Frame Number (SFN) transmitted on the Physical Broadcast Channel (PBCH) [58].

Moreover, the computational complexity is substantial, since the UE is still required to decode the PDCCH. The PDCCH is transmitted on 2, 3 or 4 OFDM symbols depending on the system bandwidth [57]. The UE has to search the different possible locations over the complete bandwidth to find its PDCCH. This requires a full-scale DFT and blind decoding over 44 possible options of PDCCH locations [57, 58] which consumes significant amount of UE processing power. Although the new control channel definition for low complexity devices can reduce computational complexity for decoding of the paging control information [43], they would still require multiple repetitions of the control information in order to successfully decode the paging identifier owing to the low operating SNR. Furthermore, this decoding has to performed on each wake-up occasion of the DRX cycle, regardless of whether the device has a valid upcoming page or not, thereby increasing the energy consumption of the devices.

Figure 1.3 shows the different states traversed by a legacy UE implementing the present Idle Mode DRX mechanism. The UE is initially in a "Deep Sleep" state where only the UE clock is active and all other processing units including the radio are OFF. At the wake up time instant, the UE wakes up from DRX and resynchronizes with the eNB by detecting PSS/SSS and PBCH (if the UE timing has drifted more than half a subframe). After synchronization, the UE transitions to a "Light Sleep" state

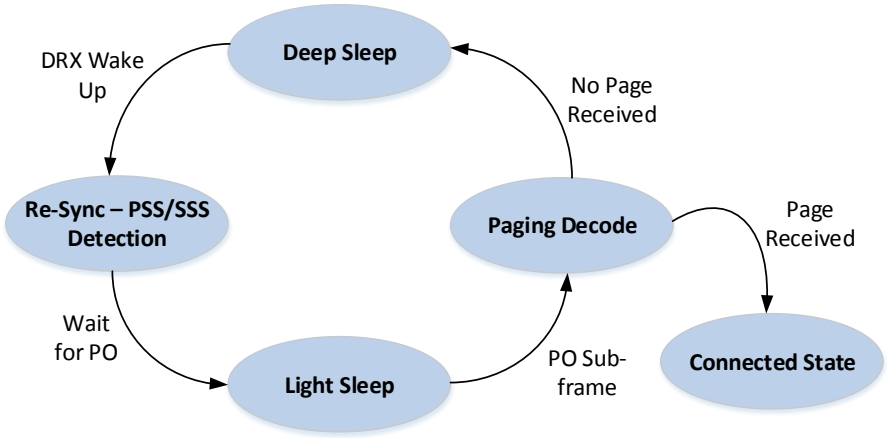


Figure 1.3: Current DRX model in LTE/LTE-A.

where only the clock, radio and channel estimation blocks are ON and the Tx/Rx processing blocks are OFF. The duration of light sleep depends on the PO. If the PO corresponds to the PSS/SSS subframe (i.e. on subframe 0 or 5), the UE proceeds to the "Paging Decode" state immediately (see Figure 1.2). But if the PO is on subframe 4 or 9, the UE waits for the PO by moving to the "Light Sleep" state and it transitions to "Paging Decode" state on the PO subframe. In the "Paging Decode" state, the UE decodes the PDCCH and the PDSCH (if the PDCCH contains the P-RNTI) for the paging information and moves to the "Connected State" if there is a valid page. Otherwise, it goes back to the "Deep Sleep" state.

Modified DRX mechanisms for improved energy efficiency are described in Chapter 2 and Chapter 3 of this thesis.

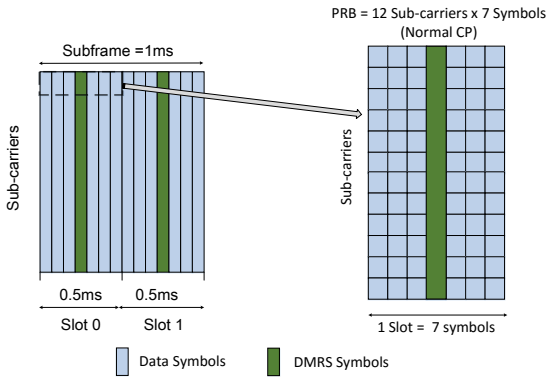


Figure 1.4: Uplink subframe and PRB in LTE/LTE-A.

### 1.2.2 Narrow-Band Internet of Things (NB-IoT) in LTE/LTE-A

With a large number of MTC devices requiring the cellular network for operation and a substantial portion of these devices being deployed in areas with bad network coverage, the 3GPP is in the process of standardizing the procedures for optimal operation of such UEs. The research activities in this domain have been categorized as NB-IoT and various mechanisms in downlink and uplink are being analyzed to address the requirements of MTC UEs [45–48]. In this section, we describe the NB-IoT transmission mechanism being standardized in the 3GPP LTE/LTE-A uplink and analyze the energy efficiency of the MTC UEs using this mechanism.

The basic unit of resource allocation in LTE/LTE-A is a Physical Resource Block (PRB). Considering a system with normal CP, one PRB consists of 12 subcarriers $\times$ 7 symbols (see Figure 1.4). Therefore, a PRB pair spans 12 subcarriers $\times$ 14 symbols = 12 subcarriers $\times$ 1 subframe [57, 58, 61, 62]. Since the subcarrier spacing in LTE/LTE-A is 15 kHz, a PRB pair occupies a bandwidth of $15 \times 12 = 180$ kHz. The current LTE/LTE-A standards support UE transmission over multiple PRBs. However, considering that the MTC UEs are low data rate and low power devices,

the 3GPP has proposed the use of a single PRB pair transmission scheme for NB-IoT MTC UEs. Also, the modulation supported by these devices is restricted to QPSK.

LTE/LTE-A has allowed the use of sub-PRB transmission, where the UE uses less than 12 subcarriers for its transmission. For example, the UE can adopt a single-tone transmission scheme, where the UE uses 1 subcarrier $\times$ 1 subframe transmission and occupies a bandwidth of only 15 kHz [46–48]. Although using a single subcarrier reduces the data rate, it can still be effective for MTC UEs that are delay tolerant and only require occasional small bursts of data to be transmitted. Furthermore, when MTC UEs are in low coverage, the operating SNR at the eNB is very low (around -15 dB). Consequently, in the uplink, the UE has to transmit multiple repetitions of the data block to be successfully decoded by the eNB, thereby increasing the ON time and the energy consumption of the UE. Therefore, identifying signal processing techniques that can reduce the number of repetitions is necessary.

In LTE/LTE-A, a data block at the physical layer is called the transport block. The transport block is encoded using a Convolution Turbo Code (CTC) before transmission and 4 Redundancy Version (RV)s are generated [58,59]. One RV of the transport block is transmitted in one subframe. Each RV includes a 24-bit header from the upper layers [58, 59]. Therefore, the effective data rate is given by

$$R_{\text{eff}} = \frac{(\text{TBS} - 24)}{(N_{\text{SF}} \times t_{\text{SF}})} \tag{1.1}$$

where TBS is transport block size, $N_{\text{SF}}$ is the number of subframes required by the eNB to successfully decode the data and $t_{\text{SF}} = 1$ ms, is the duration of a subframe in LTE/LTE-A. In the case of low data rate MTC UEs, the transmission consists of a burst of data packets followed by a long idle duration. When the effective data rate increases, the UE can complete its data transmission quickly and switch to the

idle mode sooner, thereby saving power. For a given Transport Block Size (TBS), the effective data rate increases if the number of subframes required for successful decoding decreases. This depends on the SNR, the underlying channel and the offset in UE's timing/frequency estimation at the eNB.

The UE timing/frequency offset is derived from the detection of the random access signal transmitted by the UE when it first requests network access and/or the periodic Demodulation Reference Signals (DMRS) transmitted by the UE in every subframe [58]. Both the random access and DMRS signals are Zadoff-Chu (ZC) sequences, which possess good detection properties (good autocorrelation, low cross-correlation) [58, 59]. However these estimates are not perfect and there will be some residual timing and frequency offset in the system. The effective data rate and hence the energy efficiency of the UE can be improved if these residual offsets are reduced to a negligible level.

The residual timing offset can be estimated with a sufficient degree of accuracy using the CP [63, 64]. The eNB ensures that all UE transmissions are time synchronized using the timing advance indication mechanism after the initial random access request procedure in LTE/LTE-A and minor deviations in the received frame timing are tracked using CP autocorrelation [58]. However, the residual CFO of each UE might be different and tracking each UE's CFO using CP autocorrelation is complex. Therefore, the eNB needs a separate mechanism to compensate for this CFO and improve the energy efficiency of the UE.

In Chapter 4 of this thesis, a robust ML based CFO estimation algorithm, which outperforms the conventional CP autocorrelation method is demonstrated to improve the energy efficiency of the MTC UEs for the NB-IoT uplink.

## 1.3 Literature Review

With the necessary background information established from the previous section, in the following, we review the prior works elated to the energy efficient mechanisms in the downlink and the uplink across different wireless communication technologies.

### 1.3.1 Prior Work on Power Saving Mode and DRX Analysis

The study of the performance of the power-saving mode of operation in wireless communication systems has gathered the interest of researchers in various technical communities.

The power-saving mode supported by the IEEE 802.16 standard for Wireless Interoperability for Microwave Access (WiMax) has been analyzed in [65–71]. Initial work on analyzing the sleep mode in the IEEE 802.16 e standard was carried out in [65], where the authors determine the packet dropping probability and the mean waiting times of packets in the base-station buffer for Poisson packet arrival process and a general distribution for service time. An analytical model to determine the sleep mode energy savings was developed in [66], assuming only incoming messages and a Poisson distribution for the frame arrival rate. In [67], the authors extend the work in [66] by considering the effects of both the incoming frames and outgoing frames on the sleep time. These queueing theory based models were adopted for IEEE 802.16 m standard in [68] (for uncorrelated traffic) and [69] (for correlated traffic) by incorporating the duration of the awake state and a close down timer indicating the end of the awake state. In [70], the authors proposed an efficient power-saving mechanism involving periodic traffic indications, which is also resource-efficient for IEEE 802.16 e/m. The analysis of the power-saving mode in terms of the trade-off

between the power consumption and the packet transmission delay for heterogeneous traffic (real time and non-real time) was carried out in [71].

The term "DRX" for power-saving was first introduced in the Universal Mobile Telecommunications System (UMTS) standard. In [72], the authors investigated the UMTS DRX mechanism for reduced power consumption using two parameters - the inactivity timer threshold and the length of the DRX cycle. The inactivity timer is a timer initiated by the Radio Network Controller (RNC), when there is no packet to send to the mobile device. The mobile device can go to "sleep" only after the inactive timer has expired. If a packet arrives at the RNC before the inactivity timer expires, then the link moves to"busy" state. A variant of the $M/G/1$ queueing mode with vacations was presented in [72] to analyze the UMTS DRX performance in terms of the expected queue length, the expected packet waiting time, and the power saving factor. This work was extended in [73], where an adaptive algorithm called dynamic DRX was devised to dynamically adjust the inactivity timer threshold and the DRX cycle length values to enhance the performance of the UMTS DRX. An adaptive DRX mechanism for UMTS was developed in [74]. Here, the DRX period for each UE was individually and adaptively controlled by the UMTS base-station using the extended paging indicator, which in-turn was configured based on the current traffic situation for each UE. The aforementioned works on the UMTS DRX considered Poisson traffic. In [75], the authors proposed a novel semi-Markov process to model the UMTS DRX with bursty packet data traffic. The study provided the selection guidelines for the inactivity timer and DRX cycle values under various packet traffic patterns. The study of the power consumption and the mean packet waiting time of a dual-mode mobile device (a device that supports both UMTS and WLAN radio technologies) is conducted in [76].

#### 1.3.1.1 Prior Work on LTE DRX

With the advent of LTE as a leading wireless communication standard, the study of the DRX mechanism in LTE has gained a lot of interest over the past few years. The LTE DRX operation and directions towards improving the DRX parameter selection was provided in [77]. In [78], the DRX mechanism is modeled for bursty packet data traffic using a semi-Markov process. The power saving and wake-up delay performance of the LTE DRX mechanism are evaluated and compared against the UMTS DRX mechanism. It is shown that the LTE DRX always achieves better power saving performance at the cost of longer wake-up delay. The LTE/LTE-A standards support two types of DRX based on the cycle length - short DRX and long DRX, whose performance in terms of user throughput, power consumption, and network performance is evaluated in [79].

In [78] as well as the references analyzing the UMTS DRX (see [72–75]), the procedure followed to obtain the power-saving factor is quite complex, requiring the differentiation of Laplace transform equations. This complexity is avoided in [80], where the authors provide a numerical analysis of the DRX by dividing the operation into several independent parts and combining the result obtained from each part.

The next line of interest in LTE DRX analysis is in determining the best set of DRX parameters, such as the inactivity timer duration and cycle length, for the optimal performance of a particular application. In [81], a web-browsing session as the underlying application and different algorithms for optimizing the balance among user throughput and power saving is obtained. The optimization of LTE DRX for mobile Internet applications over is considered in [82] and an algorithm is proposed to efficiently select DRX parameters to ensure a balanced trade-off between two conflicting performance parameters - application delay and UE power savings. In [83],

an analytical model for LTE DRX based on a semi-Markov process is developed to provide new, simple and exact formula relevant for the power saving efficiency. The paper also investigated the LTE DRX performance with bursty packet data traffic and the effects of different DRX parameters on the power saving and wake-up delay. The evaluation of the influences of the Transmit Time Interval (TTI) sizes and the effects of LTE DRX Light and Deep Sleep mode on power consumption for voice and web traffic has been carried out in [84]. The work in [85] investigated the use of adjustable and non-adjustable DRX cycle frame duration in LTE for reduced power consumption based on a semi-Markov model for bursty traffic. A model to analyze the latency incurred by the DRX mechanism for active and background mobile traffic is developed in [86]. The paper also proposed a mechanism to switch DRX configuration based on traffic running at UE. Recently, an in-depth analysis of the average delay and power consumption of the DRX mode adopting recursive deduction and Markov models is provided in [87]. The paper presented the analysis using mixed DRX short and long cycles and Poisson packet arrival.

From the MTC perspective, in [88], a semi-Markov chain model is developed to analyze the DRX mechanism for MTC applications, which can be used to estimate the choice of DRX parameters. The LTE DRX performance for MTC was evaluated in [89], where the authors incorporate a model with different parameter settings corresponding to potential future M2M devices. The results indicate that extending the maximum DRX cycle length would lead to significant improvement in the energy efficiency of M2M devices. The work in [90] also suggested the benefits of an extended DRX cycle for MTC devices and analyzed the impact of introducing the extended DRX feature on the operation of the networks, thereby providing a guideline to facilitate extended DRX. A new approach of augmenting the extended DRX mechanisms

with the single-packet-active state embedded in the sleep cycle was presented in [91]. This technique is shown to not only improve the power saving obtained from the DRX but also reduce the wake-up delays compared to the standard DRX method because it is sensitive to the underlying traffic pattern and able to shift between the active and sleep states rapidly.

However, all these works address the DRX operation for UEs in normal coverage and assume perfect timing synchronization. For the low-complexity MTC UEs with coverage enhancement, the authors in [92] demonstrate a new mechanism where the UE does not check for the page periodically and turns ON its radio only for data transmission, thereby reducing the energy consumption of the UE. This mechanism is only applicable to transmit driven UEs and cannot be used by UEs which require timely information from the eNB to operate successfully.

In Chapter 2 and Chapter 3 of this thesis, we elaborate on our modified DRX mechanism, which improves the downlink energy efficiency of MTC UEs in normal coverage and low coverage. These mechanisms require a minimum bandwidth of 1.4 MHz and are therefore applicable to the UE categories of CAT-M1, CAT-0 and above. However, the ideas can be easily modified to suit devices with smaller bandwidths and will serve as a medium to design novel power saving and paging mechanisms in the downlink for the upcoming 5G New Radio (NR) standard.

### 1.3.2 Prior Work on Energy Efficient M2M Uplink Mechanisms

The uplink is considered to be the most critical channel for M2M communication, especially with the increasing number of IoT M2M devices. The design and development of energy efficient mechanisms for M2M uplink has been studied in various

previous works.

An optimized signal flow in the uplink for M2M devices, radio access networks and core networks was proposed in [93]. The paper suggested the use of simplified uplink mechanisms at the M2M device, such as reduced Channel State Information (CSI) feedback for 3GPP MTC UEs to conserve power. In [94], an access control algorithm using K-means based grouping and coordinator selection is proposed to reduce the uplink energy consumption and alleviate the loading at the base-station occurring from the massive access requests from the M2M devices.

The effect of the large number of M2M devices on the random access channel has been analyzed in [95–98]. In [95], the problem of radio access network overload is addressed using a prioritized random access scheme. The proposed scheme also ensures the QoS constraints of the different classes of the LTE MTC devices by pre-allocating the Random Access Channel (RACH) resources for the different MTC classes, defining the class-dependent backoff procedures and by using dynamic access barring (see [96]) to prevent a large number of simultaneous RACH attempts. An evaluation methodology fully compatible with the 3GPP test cases is proposed in [97], which incorporates a thorough analysis of RACH performance in overloaded MTC scenarios. The work presents an analytical model for RACH including the energy consumption aspect along with the conventional performance metrics, such as the access delay and the collision probability. In [98], a reinforcement learning-based eNB selection algorithm is proposed that allows the MTC devices to transmit packets in a self-organized manner to the chosen eNB.

The energy efficiency aspect with respect to MTC data transmission has been addressed in [99–102]. Joint massive access control and resource allocation schemes are proposed in [99], which perform machine node grouping, coordinator selection and

coordinator resource allocation. The proposed schemes consider a two-hop transmission protocol and determine the number of groups required to minimize total energy consumption under both flat fading and frequency-selective fading channels. For small data transmission, a novel contention-based LTE transmission mechanism is proposed in [100]. The performance results demonstrate reduced network resource consumption, shorter mean data delay and improved device energy efficiency. In [101], it is demonstrated that the energy-efficiency of the transmissions of small data blocks strongly depends on the transmission power and the adaptive modulation and coding procedure used. The authors propose a scheme to determine the optimal Modulation and Coding Scheme (MCS) for small data transmission utilizing the LTE uplink power control mechanism. The work in [102] focuses on developing a systematic framework to study the power and energy optimal system design for M2M. The optimal transmit power, energy per bit, and the maximum load supported by the base station are derived for a variety of coordinated and uncoordinated transmission strategies. It is demonstrated that Frequency Division Multiple access (FDMA), including equal bandwidth allocation, is sum-power optimal for the low spectral efficiency regime and the performance of uncoordinated Code Division Multiple Access (CDMA) is comparable to FDMA when the base station is lightly loaded.

The aforementioned works have only been evaluated for UEs under normal coverage. For UEs in low coverage, several TTI bundling enhancement schemes are proposed in [103] based on the parameterization of the bundle size, round trip time and the maximum number of HARQ retransmissions. These schemes are evaluated using link-level simulations and shown to improve the LTE uplink coverage. In [104], the TTI bundling enhancement, frequency hopping, increased number of base-station receiver antennas and power boosted uplink reference signals have been considered as

potential candidates for coverage enhancement in the LTE uplink. In [105], a flexible TTI bundling scheme with CDMA support us demonstrated to improve the coverage of LTE MTC devices.

Chapter 4 of this thesis focuses on NB-IoT based uplink transmission mechanisms combined with robust CFO estimation for enhancing the energy efficiency of the MTC UEs in the uplink. Since these mechanisms are designed for the lowest possible bandwidth supported by the LTE MTC standard, it is applicable to all the UE categories (NB-IoT, CAT-M1 and above) and the design principles can be adopted for the forthcoming 5G NR standard.

# Chapter 2

# Discontinuous Reception (DRX) with Quick Sleeping

## 2.1 Introduction

The current LTE/LTE-A standards use the DRX mechanism to reduce the power consumption of the UE during which it follows a sleep and wake-up cycle (as explained in Section 1.2.1). The UE wakes up periodically to check for the paging information from the eNB. Though the DRX procedure results in significant power reduction, the amount of power spent by the UE during the wake-up time or the ON time is still considerable, since the decoding of paging information is computationally intensive. Also, the UE may need to reacquire timing synchronization due to the drift in the UE clock, which further increases the ON time. Moreover, in the IoT scenario, due to the presence of a huge number of devices, the probability of the UE receiving a page during each ON period is substantially low. However, the UE still looks for paging information every time it wakes up and expends a significant amount of power.

In this chapter, we propose the Quick Sleeping Indication (QSI) mechanism to indicate to the UE whether it can sleep early, since there is no valid incoming page. When our QSI mechanism is used, the UE would first decode the QSI message and if it indicates "sleep", the UE goes back to sleep immediately. If the QSI indicates "stay-awake", the UE remains ON for decoding the subsequent paging block.

It would be helpful to the UE if the QSI mechanism is simple and structured such that the UE can decode it with low complexity and reduced power consumption. To this end, we provide the QSI design mechanisms for two categories of MTC UEs - a) without CE and b) with CE. Our QSI mechanisms are not only simple to implement, but also require minimal changes to the present 3GPP LTE/LTE-A standardization framework. We show that we can obtain a substantial improvement in energy efficiency and a significant reduction in computational complexity using our novel QSI mechanisms for MTC UEs with and without CE.

The rest of the chapter is outlined as follows. In Section 2.2, we introduce the QSI mechanism and explain our modified DRX with QSI. In Section 2.3, we discuss the QSI mechanisms for MTC UEs without CE. In Section 2.4, we consider the case of MTC UEs with CE and demonstrate our QSI mechanisms for this case. We follow up with the energy efficiency and computational complexity analysis in Section 2.5 and the simulation results in Section 2.6. The conclusions are presented in Section 2.7.

## 2.2 Details of the QSI Mechanism

In the IoT scenario, the eNB would have to communicate the paging message to a large set of MTC UEs. The paging message is transmitted in the downlink through a transport channel called the paging channel, which is mapped to the PDSCH physical channel. The paging channel can accommodate a maximum of 16 UE identities [59]. Thus, the eNB would have to schedule paging information multiple times, which would lead to an increase in the time required by an UE to receive the paging information. The MTC UEs might be able to handle the delay in receiving paging information, since they are delay tolerant. However, the UEs listen to multiple paging occasions before they receive a valid paging message resulting in increased power

consumption.

If a QSI mechanism is introduced, then it gives an indication of whether the UE can go back to sleep early since it does not have an impending paging message or stay awake to decode the PDCCH. Each UE decodes the QSI and processes the PDCCH only if the QSI inhibits it from sleeping early. In this section, we describe our QSI mechanism and propose DRX with quick sleeping for energy efficient IoT using LTE/LTE-A.

### 2.2.1 QSI Working Mechanism

One method that the eNB can adopt to address a large number of UEs is to divide the UEs into multiple groups and allocate resources to one or more groups at each scheduling interval [43]. We propose to group the UEs using some unique UE identifier. Let us consider that the UEs have to be divided into $N_{\text{grp}}$ groups. A unique UE identifier can be used to determine the UE Group Indicator (UEGI) by the relation $UEGI = < Unique\ UE\ Identifier > \ mod\ N_{\text{grp}}$. The following identifiers can be used to determine the UE Group:

1. IMSI - The IMSI is a unique identifier assigned to every UE during the equipment manufacturing phase.

2. UEID - It is given by $UEID = IMSI\ mod$ 1024 and it is being used to determine the paging occasion in Idle Mode DRX [60].

3. Connected Mode - Radio Network Temporary Identifier (C-RNTI) - The C-RNTI is a unique number assigned to each UE when it establishes a connection with the eNB.

The device grouping techniques are out of the scope of our work. Therefore, we do

not elaborate on the device grouping strategies in MTC. We assume that the UEs are divided into groups using a known device grouping strategy and introduce the QSI mechanism. The proposed QSI works as follows:

1. The UEs are divided into $N_{\text{grp}}$ groups.

2. QSI is sent $n$ subframes before the paging occasion where $n$ is determined by the QoS constraints of the MTC UE group. It indicates one or more UE groups which will not be paged in the paging occasion.

3. The UE decodes QSI and if it indicates that its group will not be paged, the UE goes back to sleep. Otherwise, the UE prepares to decode PDCCH on the paging occasion.

After we divide the UEs into multiple groups, we assign $M$ bits for the QSI message which would put one or more UE groups to sleep when there is no impending page for the group. The network has the flexibility to configure the manner in which the QSI addresses the UE groups. One configuration that the network can use is a bit-map addressing mode where one bit is assigned exclusively to one UE group and the network can address up to $M$ groups. For example, with $M = 4$, we can address 4 UE groups and the QSI message "1010" indicates that the UE groups 1 and 3 can be put to sleep.

It should also be noted that the UE in Idle Mode DRX cannot directly wake up at the paging occasion to decode PDCCH since it has to acquire timing synchronization and update the SFN. The frame timing and synchronization is achieved by detecting the PSS and the SSS [61]. The SFN is obtained by processing the PBCH and decoding the Master Information Block (MIB) [61].

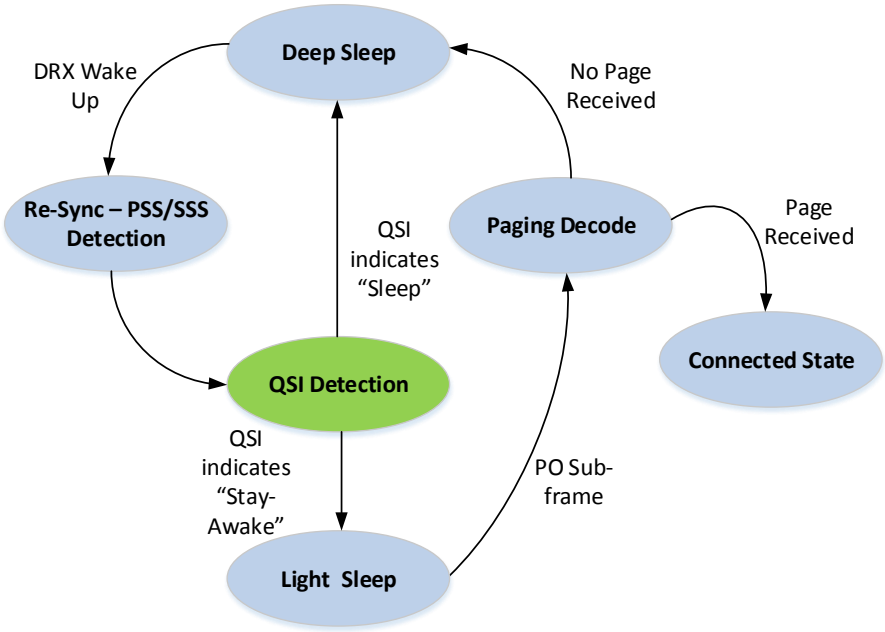


(a) Proposed DRX model with QSI (without CE)

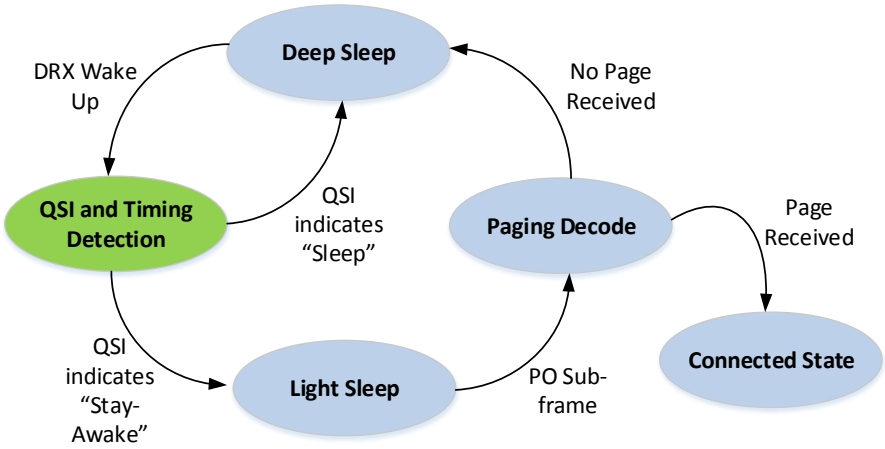


(b) Proposed DRX model with QSI (with CE)

Figure 2.1: Proposed DRX models.

### 2.2.2 DRX and Paging with QSI

Figure 2.1a demonstrates our first model for DRX and paging with QSI, which we use for MTC UEs without CE. In this model, the UE begins its paging detection operation similar to the legacy UE, by transitioning from the "Deep Sleep" state to the "Re-sync State" to acquire the symbol boundary when it wakes up from the DRX cycle. However, after the timing acquisition, the UE transitions to the "QSI Detection" state, where it detects the QSI signal. If the QSI conveys "sleep" since there is no valid upcoming page, then the UE immediately transitions into the "Deep Sleep" state. However, if the QSI signals indicates "stay-awake" or if the QSI is not detected successfully, the UE resumes the legacy operation for decoding the paging information and transitions to the "Light Sleep" state.

The MTC UEs can be deployed in places like interiors of buildings and basements where the network coverage is low. When the SNR is low, multiple PSS/SSS copies will have to be combined for successful detection and timing synchronization. The PSS/SSS is transmitted every 5 ms and the UE has to stay ON longer if it requires multiple copies of PSS/SSS. Also, the PDCCH and PDSCH decoding might require multiple repetitions to be decoded successfully which would further increase the ON time and the computational complexity for paging decode. Therefore, it is beneficial to have a QSI signal which can also be used for subframe synchronization for MTC UEs with CE. In this case, the different combinations of $M$ QSI bits are mapped to different sequences, thereby resulting in $2^M$ QSI sequences. The sequence corresponding to the QSI message is transmitted periodically. The UE receiver detects the transmitted QSI sequence by hypothesizing over the set of $2^M$ QSI sequences and decodes the QSI message as well as the timing information.

Figure 2.1b depicts our second model for DRX and paging with QSI for CE. The

UE begins its paging detection operation by transitioning from the "Deep Sleep" state to the "QSI and Timing Detection" state where it jointly obtains the timing and sleeping indication. If the QSI conveys "sleep", the UE moves back to the "Deep Sleep" state immediately and if the QSI indicates "stay-awake", the UE transitions to the "Light Sleep" state and decodes the page by moving to the "Paging Decode" state on the PO. If the QSI is not detected, then the UE follows legacy DRX operation in order to decode the paging information.

In the following, we present different implementations for the proposed DRX and paging with QSI for MTC UEs without CE and with CE. Our QSI solutions are designed such that they are compatible with the LTE/LTE-A framework and help in energy efficient operation of MTC UEs for IoT.

## 2.3 Quick Sleeping Solutions for MTC UEs Without CE

In this section, we discuss the QSI mechanisms for MTC UEs without CE. This is applicable to the IoT scenario of pet tracking or weather sensing in which the UEs have low-mobility and are located in regions where the network coverage is good. In this case, we design the QSI such that it reuses the resources that are already being allocated by the eNB. We choose to transmit the QSI on those physical channels whose locations on the subframe grid do not change so that the UE is aware of the location of the QSI. The physical channels for synchronization and broadcast comply with our requirement.

The key feature of PSS, SSS and PBCH is that they always occupy a constant bandwidth of 1.4 MHz regardless of the system bandwidth. The PSS and SSS are

transmitted every 5 ms on subframe 0 and subframe 5 (see Figure 1.2) [57]. They occupy one symbol and the UE can use a correlation decoder to detect these synchronization signals and adjust the frame timing [58]. The PBCH occupies 4 symbols on subframe 0 (see Figure 1.2) and is transmitted every 10 ms and has 4 repetitions. Therefore, a new PBCH is transmitted every 40 ms. The construction of PBCH block is such that the UE can decode each 10 ms transmission independently or combine multiple repetitions for decoding PBCH [61]. Due to smaller bandwidth, the UE can use a smaller Fast Fourier Transform (FFT) size to decode the PBCH. Therefore, an early sleeping indication or QSI during the synchronization or the PBCH detection phase would help the UE to determine if it has to go back to sleep or proceed to decode PDCCH decoding. Hence, we develop simple and efficient techniques to transmit QSI on PBCH and PSS/SSS.

### 2.3.1 Quick Sleeping Solutions Using the PBCH

First, we present a brief overview of the PBCH transmission in the current 3GPP LTE standard. Then, we demonstrate four methods for incorporating the QSI mechanism into the PBCH.

#### 2.3.1.1 PBCH in 3GPP LTE

PBCH carries the MIB, which is 24 bits of information. As depicted in Figure 2.2, it indicates the eNB bandwidth, the Physical Hybrid ARQ Indicator Channel (PHICH) duration, the PHICH resolution and the SFN [12, 62]. The SFN in LTE has 10 bits. Since the MIB has only 8 bits to represent SFN, this field it indicates 8 most significant bits of SFN. From the PBCH processing in Figure 2.2, it can be seen that a 16 bit Cyclic Redundancy Checksum (CRC) is attached to the 24 information bits

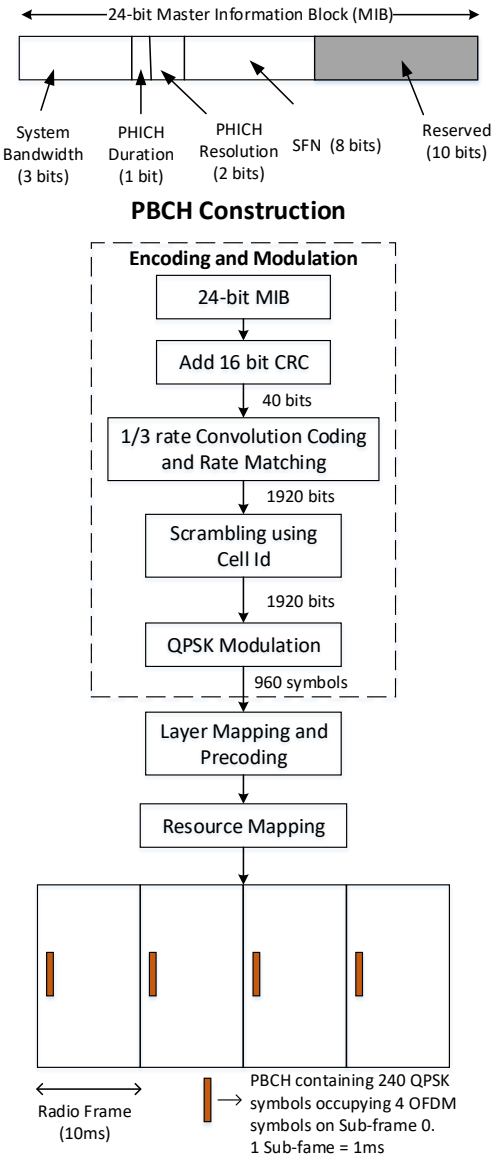


Figure 2.2: MIB and PBCH construction.

transforming MIB into a 40 bit block. This is followed by rate 1/3 Convolution Coding (CC) and rate matching so that the encoded MIB is 1920 bits. The modulation used for PBCH is QPSK and these modulated symbols have to be transmitted in 40 ms. This corresponds to 960 QPSK symbols every 40 ms which implies that there are 240

QPSK symbols in every 10 ms copy of PBCH.

#### 2.3.1.2 QSI Using Reserved Bits in MIB

Our first solution is to use the reserved bits in MIB for QSI. The MIB transmitted on PBCH contains 10 reserved bits out of the 24 information bits. Considering that the UEs are divided into groups, these bits can be used to indicate the UEGI. Using $M$ reserved bits, $2^M$ UE groups can be addressed. For example, by using 4 out of 10 reserved bits, we can address 16 UE groups. Alternatively, $M$ reserved bits can be used to indicate multiple UE groups. For example, QSI bit 0 would indicate UE groups 1 to 4, QSI bit 1 would indicate UE groups 5 to 8 and so on. Using reserved bits in MIB ensures that QSI is decoded along with PBCH without affecting the performance of PBCH decoding.

#### 2.3.1.3 Spreading QSI Using Orthogonal Sequences

Our second solution is to transmit the QSI over PBCH using sequences that are orthogonal to PBCH. That is, the $M$ bits of QSI are mapped to $2^M$ sequences which are orthogonal to the PBCH transmission. The orthogonal sequence corresponding to the QSI message is sent along with the PBCH at a very low power to ensure that the loss in the power of PBCH is small. This method is illustrated in Figure 2.3, where QSI modulated sequence denotes the orthogonal QSI sequence. Let $S_{\text{ref}}$ denote the power of the PBCH signal without QSI, $N$ denote the noise power and $S_{\text{p}}$ denote the power of the orthogonal QSI sequence. The SNR of the PBCH signal without QSI is $\text{SNR}_{\text{ref}} = \frac{S_{\text{ref}}}{N}$ and the SNR of the QSI signal is $\text{SNR}_{\text{p}} = \frac{S_{\text{p}}}{N}$. When the QSI signal is added to PBCH, the power of the PBCH signal becomes $S_{\text{new}} = (1-P)\cdot S_{\text{ref}}$, where $P$ is the fraction of the PBCH power used for QSI. Therefore, $\text{SNR}_{\text{new}} = (1-P)\cdot\text{SNR}_{\text{ref}}$ and the loss in PBCH detection performance is $(1 - P)$. For example, if $P = 0.05$,

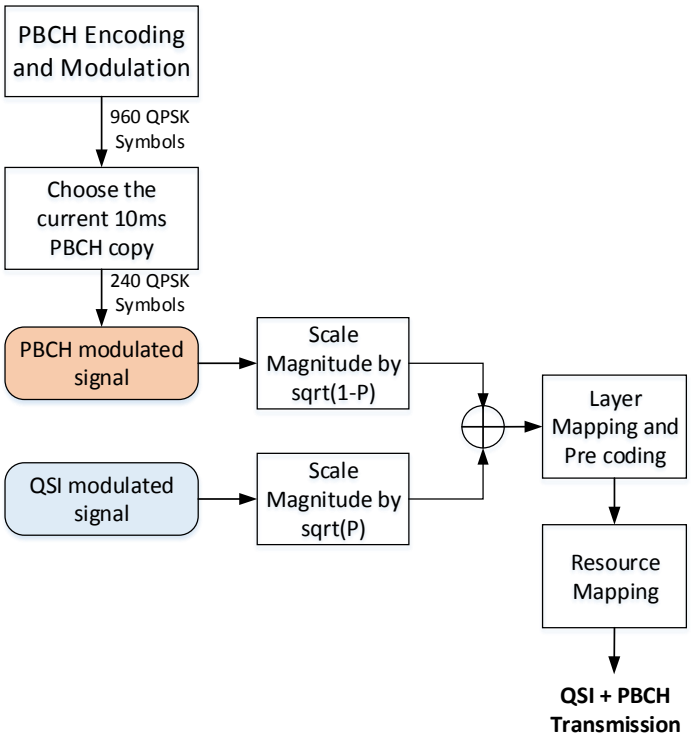


Figure 2.3: PBCH with QSI transmission

then $\text{SNR}_{\text{new}} = 0.95 \cdot \text{SNR}_{\text{ref}}$ and the loss in PBCH detection performance in dB is $10\log_{10}(0.95) = 0.22$ dB, which is small. This loss occurs since we formulate our QSI mechanism such that the total power available for PBCH transmission is unchanged. If the eNB can afford additional power for QSI transmission, there will be no loss in PBCH performance.

The QSI sequences should be orthogonal to the different possible PBCH transmissions. LTE supports 6 different eNB bandwidths (1.4 MHz, 3 MHz, 5 MHz, 10 MHz, 15 MHz, 20 MHz), 2 PHICH durations (normal, extended), 4 PHICH resolutions $\left(\frac{1}{6},\ \frac{1}{2},\ 1,\ 2\right)$ and an 8 bit field to indicate SFN [58]. This gives rise to $6 \times 2 \times 4 \times 2^8 = 12,288$ combinations. Additionally, there are 3 antenna configurations ($N_{\text{TX}} = 1$, 2 or 4) resulting in $12,288 \times 3 = 36,864$ combinations. Since

the PBCH symbols are scrambled by the Cell ID, there are 36,864 combinations per Cell ID. Therefore, for a given Cell ID and a 10 ms copy of PBCH, we have a $36,284 \times 240$ complex matrix representing all the possible combinations of PBCH. We generated this matrix in MATLAB and observed that the rank of this matrix is pretty low (approximately 100). This suggests that sequences orthogonal to PBCH combinations per Cell ID can be derived from the null space of this matrix. There are 504 Cell Ids. Therefore, the total number of QSI sequences is $504 \times 2^M$, each being a complex vector of length 240. Also, there are 4 different 10 ms copies of PBCH. If each complex number is represented using 32 bits, this scheme would require a table of $(4 \times 504 \times 2^M \times 240 \times 4)$ bytes . For example, with 4 QSI bits, there are $504 \times 16 = 8064$ QSI sequences and they would require a memory of 29.53 MB which is large. In the following, we describe the QSI methods which eliminate the need for orthogonal sequences and hence does not require extra memory.

#### 2.3.1.4 Spreading QSI Using Repetition Only

In this method, the QSI bits are repeated at a very low power across the PBCH symbols similar to the solution using orthogonal sequences. But in this case, the QSI modulated signal in Figure 2.3 is generated as shown in Figure 2.4a. The $M$ bits of QSI are spread over 480 bits of 10 ms copy of the PBCH. Hence the spreading factor $SPF = \frac{480}{M}$. The QSI bits are also modulated using QPSK. Due to the large spreading gain, the QSI signal can be detected after we subtract the detected PBCH signal from the received signal. The SNR to decode QSI signal considering that the PBCH signal is subtracted from the received signal is $P \cdot \mathrm{SNR_p} \cdot SPF$. For example, with $M = 4$ and $P = 0.05$, $SPF = 120$ and the SNR to decode QSI will be $6 \times \mathrm{SNR_p}$ which is $10\log_{10}(6) = 7.78$ dB more the original QSI SNR. In addition to repetition, a randomizing sequence (RS) of length 240 symbols is used to

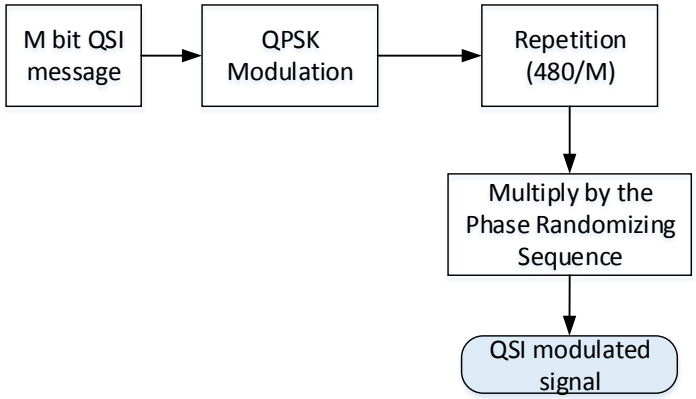


(a) Spreading QSI using repetition only

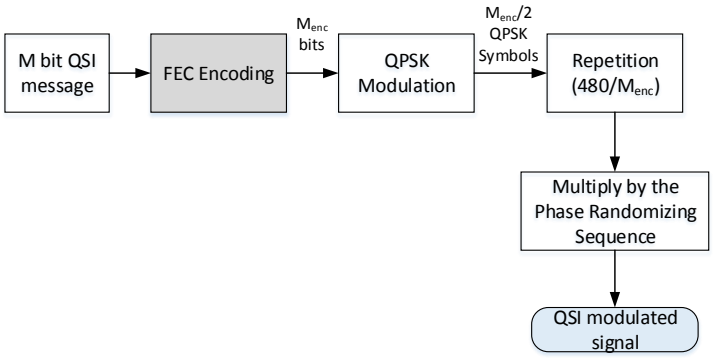


(b) Spreading QSI using repetition and FEC

Figure 2.4: Illustration of QSI mechanisms on PBCH.

ensure uniform distribution of phase of the QSI modulated signal. The transmitted constellation is determined by

$$T(n) \;=\; \sqrt{1-P}\mathrm{e}^{\mathrm{j}\theta(n)} + \sqrt{P}\mathrm{e}^{\mathrm{j}\beta(n)}\mathrm{e}^{\mathrm{j}\phi(n)} \tag{2.1}$$

where $\theta(n)$ is the phase of the $n^{th}$ PBCH modulated signal, $\phi(n)$ is the phase of the $n^{th}$ QSI modulated signal, $\beta(n)$ is the phase of the $n^{th}$ complex number in the randomizing sequence and $n \;=\; 0, 1, \ldots 239$. The Signal-to-Interference-plus-Noise

Ratio (SINR) is given by

$$\begin{aligned} \text{SINR} &= \frac{(1 - P) \cdot S_{\text{ref}}}{P \cdot S_{\text{p}} + N} \\ &= \frac{(1 - P) \cdot \text{SNR}_{\text{ref}}}{P \cdot \text{SNR}_{\text{p}} + 1} \end{aligned} \tag{2.2}$$

Therefore, we expect that the loss in performance is the factor $\frac{(1 - P)}{(P \cdot SNR_p + 1)}$. Again, the loss occurs since we model the QSI mechanism such that the total power available for PBCH transmission is unchanged.

#### 2.3.1.5 Spreading QSI Using Repetition and Forward Error Correction (FEC)

This solution is similar to the previous one, but the QSI bits are encoded using an error correction coding scheme (see Figure 2.3 and Figure 2.4b). Here, the $M$ QSI bits result in $M_{\text{enc}}$ encoded bits and the spreading factor is $SPF = \frac{480}{M_{\text{enc}}}$. The SNR to decode the QSI signal considering that the PBCH signal is subtracted from the received signal is reduced by a factor of $\frac{M}{M_{\text{enc}}}$, but the FEC makes up for the loss in SNR. Also, if the number of QSI sequences is small, a Maximum Likelihood (ML) decoding scheme can be used for FEC decoding. For example, with $M = 4$, $P = 0.05$ and an (8,4) extended Hamming code for FEC, $M_{\text{enc}} = 8$ and $SPF = 60$.

Next, we discuss our QSI solutions using the synchronization channels (PSS/SSS).

### 2.3.2 QSI on PSS/SSS

PSS and SSS are the synchronization signals used in LTE/LTE-A transmitted on the centre band. The PSS is a 63-length ZC sequence which is sent with a periodicity of 5 ms on the last symbol of the first slot in subframe 0 and subframe 5. The 32$^{\text{nd}}$

Table 2.1: QSI transmission methods using unused subcarriers on PSS and SSS

| Method | $C_{\mathrm{m}}$ | FEC Used | $N_{\mathrm{s}}$ | $N_{\mathrm{r}}$ |
|---|---|---|---|---|
| 1 | BPSK | No | 1 | 2 |
| 2 | BPSK | No | 2 | 4 |
| 3 | BPSK | Yes | 1 | 1 |
| 4 | BPSK | Yes | 2 | 2 |

carrier corresponds to the DC subcarrier and it is set to zero [58]. The SSS consists of two 31-length m-sequences on either side of the DC subcarrier. The SSS is also sent in subframe 0 and subframe 5 one symbol before the PSS. But the SSS on subframe 0 is not the same as the one on subframe 5 and this helps the UE determine if it is on the first half of the radio frame or the second half during acquisition [58]. The centre band spanning 1.4MHz consists of 72 subcarriers including the DC subcarrier. The key feature of both PSS and SSS transmissions is that they use only 62 out of the 72 subcarriers. Thus, excluding the DC subcarrier, we still have 9 unused subcarriers. We therefore propose to transmit $M$ QSI bits using 8 out of the 9 unused subcarriers.

For this mechanism, we consider the case where $M \leq 4$ and build a 4-bit QSI message. When $M \leq 2$, the bits can be repeated and when $M = 3$, a zero can be appended as the most significant bit in order to obtain the 4-bit QSI message. Let $C_{\mathrm{m}}$ and $N_{\mathrm{s}}$ denote the modulation scheme and the number of synchronization symbols used for QSI transmission respectively. The number of repetitions required to accommodate the 4-bit message on the unused subcarriers is $N_{\mathrm{r}} = \frac{8 \cdot N_{\mathrm{s}}}{4} = 2N_{\mathrm{s}}$. Table 2.1 summarizes variants for the proposed QSI transmission on PSS/SSS using different repetition factors without and with FEC. For the latter, we suggest a (8,4) extended Hamming code, because we use 8 unused subcarriers per synchronization symbol to accommodate the 4-bit QSI message.

We assume that the eNB has to use a part of the available power for transmitting the QSI. When there is no QSI, the eNB transmission power is uniformly distributed

over 62 subcarriers and in the presence of QSI, it is distributed uniformly over 70 subcarriers. Therefore, the loss in PSS/SSS SNR when QSI is transmitted can be computed as $10\log_{10}(\frac{62}{70}) = -0.53$ dB, which is a small degradation from the original value. If the eNB can afford additional power for QSI transmission, there will be no degradation in PSS/SSS performance.

## 2.4 Quick Sleeping Solution for MTC UEs With CE

In the case of IoT, the UEs may be located in places like underground parking lots to sense vacant parking spots or in the interior of buildings such as hospitals to monitor the status of the patients where the network coverage is very low. The solutions discussed in Section 2.3 do not work effectively in this case, because the UE will need multiple repetitions of PSS/SSS to determine the timing since the SNR is very low. And if the UE needs to re-acquire PBCH, it would need multiple copies of PBCH to accurately determine the SFN. Similarly, decoding the paging on PDCCH, PDSCH and the QSI will also require multiple repetitions, which increases the ON time of the UE. Therefore, it is preferable to design a robust QSI signal which not only indicates whether a group of UEs can be put to sleep quickly, but also helps in faster timing synchronization. A UE decoding such a QSI signal would obtain both the paging and timing information in parallel which could reduce the ON time and paging decoding complexity, thereby saving energy. In this section, we present the QSI signal design mechanism for MTC UEs with CE using dedicated resources in the PDSCH space.

In particular, we propose to use ZC sequences to create QSI signals which possess good auto-correlation and cross-correlation properties and thus enable robust signal

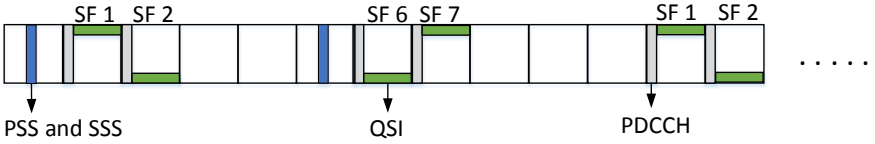


Figure 2.5: QSI transmission mechanism on PDSCH.

detection. ZC sequences are Complex Amplitude Zero AutoCorrelation (CAZAC) sequences and cyclically shifted versions of these sequences are orthogonal to each other [58]. Also, the cross-correlation of two ZC sequences of length $N$ is limited by $\frac{1}{\sqrt{N}}$. They are already being used in LTE/LTE-A for PSS and random access. The proposed QSI ZC sequence is of the form

$$\mathrm{QSI}_{\mathrm{ZC}}(p) = \mathrm{e}^{\left(\frac{-j\pi pn(n+1)}{N}\right)} \tag{2.3}$$

where, $N = 131$ is the length of the ZC sequence and $p$ is the root of the ZC sequence chosen such that it is co-prime with $N$. We choose $p \in [2 + 8 \cdot (q-1)]$ where $q = 1, 2, \cdots 16$. The QSI sequence occupies 131 subcarriers. This length is chosen because a legacy paging block would take at least 1 PRB pair and considering 2 symbol-PDCCH, this would occupy 132 subcarriers [57,59]. One could always choose a longer length sequence to improve the performance since the cross-correlation peak is inversely proportional to the length of the sequence, but a longer sequence would require more resources.

Our proposed QSI transmission mechanism in the PDSCH space uses 1 PRB pair in subframes 1, 2, 6 and 7 of a radio frame. These subframes are chosen to provide time diversity to the QSI signal and ensure that it is periodic. We use the centre 1.4 MHz band and transmit the QSI ZC sequence on the top PRB pair of subframes 1 and 7 and the bottom PRB pair of subframes 2 and 5, thereby introducing some

frequency diversity to the QSI signal. This also ensures that the QSI pattern has a periodicity of 10 ms and the UE can determine the exact subframe number when it detects the QSI. Figure 2.5 illustrates the proposed QSI signaling pattern.

## 2.5 Energy Consumption and Computational Complexity Analysis

In this section, we analyze the reduction in UE energy consumption and the number of UE computations for our different QSI solutions. Prior to this work, the energy consumption of the UE in DRX mode has been analyzed using a semi-Markov chain model [78, 88] or a queueing based model [80]. In our work, we use a simpler model where the energy consumption is derived from the ON time of the UE similar to [89] and the computational complexity is determined using the number of FFT operations performed by the UE.

### 2.5.1 Energy Consumption Analysis

Let $t_{\mathrm{DRX}}$, $t_{\mathrm{Sync}}$ and $t_{\mathrm{Paging}}$ denote the total time of UE DRX cycle, time taken by the UE for synchronization and the UE ON time for paging decode respectively. The time spent by the UE in the "Light Sleep" state and the drift time of the UE clock are represented by $t_{\mathrm{LS}}$ and $t_{\mathrm{Drift}}$ respectively. $P_{\mathrm{ON}}$, $P_{\mathrm{LS}}$ and $P_{\mathrm{DS}}$ denote the power consumed by the UE during the ON state, the "Light Sleep" state and the "Deep Sleep" state respectively.

#### 2.5.1.1 Legacy UE in Idle Mode DRX

Firstly, we consider the case of a legacy UE without CE at an operating SNR good enough to decode PSS/SSS and PBCH in the first attempt. For PSS/SSS detection, we assume that the UE is ON for a duration of one subframe since the UE has to search for PSS/SSS within the buffered subframe, which gives $t_{\text{Sync}} = 1$ ms. When the paging subframe is 0 or 5, the legacy UE does not wait for PO and $t_{\text{LS}} = 0$. However, if the paging subframe is 4 or 9, the UE decodes the PSS/SSS on subframe 0 or on subframe 5 and has to wait 3 more subframes for its PO. The UE goes into "Light Sleep" for these subframes, which gives $t_{\text{LS}} = 3$ ms. In the case of MTC for IoT, due to the large number of UEs being paged, we can assume that the POs are equally likely and compute the average light sleep time $t_{\text{LS}}^{\text{avg}} = \frac{0+3+0+3}{4} = 1.25$ ms. The total ON time of the legacy UE is given by $t_{\text{ON}}^{\text{Legacy}} = t_{\text{Drift}} + t_{\text{Sync}} + t_{\text{Paging}}$. Therefore, the energy consumed by the legacy UE can be calculated as

$$E_{\text{Legacy}} = t_{\text{ON}}^{\text{Legacy}} P_{\text{ON}} + t_{\text{LS}}^{\text{avg}} P_{\text{LS}} + (t_{\text{DRX}} - t_{\text{ON}}^{\text{Legacy}} - t_{\text{LS}}^{\text{avg}}) P_{\text{DS}}. \tag{2.4}$$

Secondly, we consider the case of a legacy UE with CE. In this case, the SNR is low and multiple repetitions are required for successful detection of PSS/SSS and paging. Therefore, the total energy consumed by the legacy UE with CE can be calculated using Eq. (2.4) with $t_{\text{ON}}^{\text{Legacy}} = t_{\text{Drift}} + t_{\text{Sync}}^{\text{CE}} + t_{\text{Paging}}^{\text{CE}}$, where $t_{\text{Sync}}^{\text{CE}}$ and $t_{\text{Paging}}^{\text{CE}}$ denote the ON time required for PSS/SSS detection and paging decode with CE, respectively.

#### 2.5.1.2 MTC UE without CE Adopting Our DRX with QSI mechanism

Here, the QSI is transmitted on PBCH or on PSS/SSS. In both the cases, similar to the legacy case, $t_{\text{Sync}} = 1$ ms, but the average light sleep time varies depending on

where the QSI is transmitted and whether PBCH decoding is necessary. If the QSI is transmitted on PSS/SSS and PBCH decoding is not necessary, then the average light sleep time is the same as that of the legacy UE, that is, $t_{\mathrm{LS}}^{\mathrm{avg}} = 1.25$ ms. However, if the QSI is transmitted on PBCH or if the UE has slept long enough so that PBCH decoding is necessary, then the UE wakes up at subframe 0 regardless of the PO, detects PSS/SSS on subframe 0, decodes the PBCH, obtains the QSI and goes into "Light Sleep" until the PO subframe. Therefore, $t_{\mathrm{LS}}$ can be 0 ms, 3 ms, 4 ms or 8 ms and the average light sleep time $t_{\mathrm{LS}}^{\mathrm{avg}} = 3.5$ ms. Let $p$ indicate the probability of successful QSI detection and $q$ indicate the probability that the QSI conveys "sleep". Then, the probability of successful QSI detection and UE going back to sleep is $pq$ and the total ON time for the UE in this case will be $t_{\mathrm{QSI}} = t_{\mathrm{Drift}} + t_{\mathrm{Sync}}$. The corresponding energy consumed by the UE is

$$E_1 = t_{\mathrm{QSI}} P_{\mathrm{ON}} + (t_{\mathrm{DRX}} - t_{\mathrm{QSI}}) P_{\mathrm{DS}}. \tag{2.5}$$

If the QSI is detected successfully and the UE has to stay awake for paging or if the QSI signal is not detected, the UE resumes legacy mode of operation. This occurs with probability $(1 - pq)$ and the energy consumed by the UE is $E_{\mathrm{Legacy}}$ given by (2.4). Therefore, the total energy consumption of the UE without CE adopting QSI can be calculated as

$$E_{\mathrm{QSI}} = pqE_1 + (1 - pq)E_{\mathrm{Legacy}}. \tag{2.6}$$

#### 2.5.1.3 MTC UE with CE Adopting Our DRX with QSI Mechanism

In this case, the UE attempts to decode the QSI transmitted on PDSCH which gives the UE both the timing information as well as sleeping indication. The QSI signal detection, PSS/SSS detection and paging decode operations will take $t_{\mathrm{Q}}$, $t_{\mathrm{Sync}}^{\mathrm{CE}}$ and

$t^{\mathrm{CE}}_{\mathrm{Paging}}$ amount of time respectively since the SNR is low and multiple repetitions are required for successful detection. The UE has to wake up at least $t_{\mathrm{Q}} + t^{\mathrm{CE}}_{\mathrm{Sync}}$ before the PO since it has to first detect QSI and if it fails, the UE should fall back to legacy operation, detect PSS/SSS followed by paging decode. The ON time for QSI detection will be $t^{\mathrm{CE}}_{\mathrm{QSI}} = t_{\mathrm{Drift}} + t_{\mathrm{Q}}$. The energy consumed by the UE if it detects QSI successfully and the QSI indicates "sleep" (which occurs with probability $pq$) is given by

$$E^{\mathrm{CE}}_1 = t^{\mathrm{CE}}_{\mathrm{QSI}} P_{\mathrm{ON}} + (t_{\mathrm{DRX}} - t^{\mathrm{CE}}_{\mathrm{QSI}}) P_{\mathrm{DS}}. \tag{2.7}$$

If the QSI is detected successfully and it indicates "stay-awake", the UE goes into the "Light Sleep" state until the PO subframe and then decodes the paging on the PO subframe. This occurs with probability $p(1-q)$ and the energy consumed by the UE is

$$E^{\mathrm{CE}}_2 = (t^{\mathrm{CE}}_{\mathrm{QSI}} + t^{\mathrm{CE}}_{\mathrm{Paging}}) P_{\mathrm{ON}} + (t^{\mathrm{CE}}_{\mathrm{Sync}} + t^{\mathrm{avg}}_{\mathrm{LS}}) P_{\mathrm{LS}} + (t_{\mathrm{DRX}} - t^{\mathrm{CE}}_{\mathrm{QSI}} - t^{\mathrm{CE}}_{\mathrm{Paging}} - t^{\mathrm{CE}}_{\mathrm{Sync}} - t^{\mathrm{avg}}_{\mathrm{LS}}) P_{\mathrm{DS}}. \tag{2.8}$$

If the UE is unable to detect the QSI signal, then it resumes legacy operation and this scenario occurs with probability $(1-p)$. The energy consumed is

$$E^{\mathrm{CE}}_3 = (t^{\mathrm{CE}}_{\mathrm{QSI}} + t^{\mathrm{CE}}_{\mathrm{Sync}} + t^{\mathrm{CE}}_{\mathrm{Paging}}) P_{\mathrm{ON}} + t^{\mathrm{avg}}_{\mathrm{LS}} P_{\mathrm{LS}} + (t_{\mathrm{DRX}} - t^{\mathrm{CE}}_{\mathrm{QSI}} - t^{\mathrm{CE}}_{\mathrm{Sync}} - t^{\mathrm{CE}}_{\mathrm{Paging}} - t^{\mathrm{avg}}_{\mathrm{LS}}) P_{\mathrm{DS}}. \tag{2.9}$$

Therefore, the total energy consumption of the UE adopting QSI can be calculated as

$$E^{\mathrm{CE}}_{\mathrm{QSI}} = pq E^{\mathrm{CE}}_1 + p(1-q) E^{\mathrm{CE}}_2 + (1-p) E^{\mathrm{CE}}_3. \tag{2.10}$$

### 2.5.2 Computational Complexity Analysis

The paging decoding requires PDCCH decoding as its first step regardless of whether the UE is being paged or not. PDCCH requires a full eNB bandwidth size FFT which requires $O(N \log_2 N)$ computations, $N$ being the FFT size.

#### 2.5.2.1 Legacy UE in Idle Mode DRX

First, we consider the case of a legacy UE without CE which takes one subframe for PSS/SSS detection to reacquire the timing and one subframe to decode the paging block. The PSS/SSS and the PBCH require a 128 point FFT [58]. Considering that for normal CP length, we have 14 symbols in a subframe, the number of FFT operations for synchronization is $n_{\text{Sync}} = 14 \times 128 \log_2(128) = 12544$. Assuming that the PDCCH occupies $m$ symbols, the UE would require $n_{\text{PDCCH}} = m \cdot O(N \log_2 N)$ operations for PDCCH FFT. If the PDCCH indicates P-RNTI, the UE has to proceed to decode the PDSCH which will add to the number of FFT operations of the UE. For this analysis, we take into account only the synchronization and PDCCH FFT operations for the legacy UE since we model the scenario where a UE is very rarely paged and the contribution of PDSCH FFT to the total number of FFT operations is not significant. The total number of FFT operations for the legacy UE is computed as

$$n_{\text{Legacy}} = n_{\text{Sync}} + n_{\text{PDCCH}}. \tag{2.11}$$

For the legacy UE with CE, the total number of FFT operations will be

$$n_{\text{Legacy}}^{\text{CE}} = n_{\text{Sync}} r_{\text{Sync}} + n_{\text{PDCCH}} r_{\text{PDCCH}}. \tag{2.12}$$

where $r_{\text{Sync}}$ and $r_{\text{PDCCH}}$ is the number of PSS/SSS and PDCCH repetitions required

for successful decoding respectively.

#### 2.5.2.2 MTC UE without CE Adopting Our DRX with QSI Mechanism

Here, the QSI is sent on PBCH or on PSS/SSS and does not require additional FFT compared to the legacy UE. The number of FFT operations for the UE without CE using QSI will be $n_{\text{Sync}}$ with probability $pq$ when QSI is detected and indicates "sleep". Otherwise, the UE resumes legacy operation and number of FFT operations will be equal to $n_{\text{Legacy}}$. Therefore, the total number of FFT operations for the UE implementing QSI on PBCH or QSI on PSS/SSS is given by

$$n_{\text{QSI}} = pqn_{\text{Sync}} + (1 - pq)n_{\text{Legacy}}. \tag{2.13}$$

#### 2.5.2.3 MTC UE with CE Adopting Our DRX with QSI Mechanism

In this case, the QSI signal is transmitted on PDSCH. The UE buffers the entire QSI subframe and tries to detect the QSI signal. Since we transmit the QSI on 1 PRB pair in the PDSCH space, the minimum FFT size in LTE/LTE-A which is a 128 point FFT, is sufficient to obtain the QSI signal. Thus, the number of FFT operations for detecting the QSI signal can be calculated as $n_{\text{Q}} = 14 \times 128 \log_2(128) \times r_{\text{Q}} = 12544 r_{\text{Q}}$, where $r_{\text{Q}}$ is the number of repetitions required to decode the QSI signal successfully. If the QSI signal is detected successfully and if it indicates "sleep", the number of FFT operations will be equal to $n_{\text{Q}}$ which occurs with a probability $pq$. If the QSI signal is detected successfully and if it indicates "stay-awake", it will be $n_{\text{Q}} + n_{\text{PDCCH}} r_{\text{PDCCH}}$ which happens with probability $p(1-q)$. If the QSI is not detected, then the number of FFT operations will be $n_{\text{Q}} + n_{\text{Legacy}}^{\text{CE}}$. Therefore, the total number of FFT operations

for UE with CE adopting QSI is

$$n_{\mathrm{QSI}}^{\mathrm{CE}} = pqn_{\mathrm{Q}} + p(1-q)(n_{\mathrm{Q}} + n_{\mathrm{PDCCH}} r_{\mathrm{PDCCH}}) + (1-p)(n_{\mathrm{Q}} + n_{\mathrm{Legacy}}^{\mathrm{CE}}). \quad (2.14)$$

## 2.6 Simulation Results and Analysis

In this section, we highlight the benefits of the proposed QSI solutions for LTE/LTE-A for IoT through simulation results and detailed analysis of the UE energy efficiency and computational complexity when our QSI mechanisms are used.

### 2.6.1 Simulation Results

First, the methods discussed in Section 2.3.1 were implemented and simulations were run for an Additive White Gaussian Noise (AWGN) channel. The AWGN channel was chosen since it is sufficient to determine performance differences for QSI and PBCH for the different proposed methods. The key simulation parameters are summarized in Table 2.2.

Figure 2.6 shows the PBCH Block Error Rate (BLER) and also indicates the expected BLER curves when QSI is introduced. The SNR denotes the SNR on each PBCH symbol. The PBCH symbol also contains the cell specific reference signals and the QSI signal. The expected BLER curves are obtained with the assumption that QSI does not interfere with the PBCH signal. and the loss in PBCH detection performance is $(1 - P)$SNR as discussed in Section 2.3.1.

It can be observed that the QSI using orthogonal sequences shows 0.22 dB degradation in PBCH BLER performance when compared to the legacy UE PBCH BLER performance which matches the analytical results. However, there is a small difference between the expected BLER and actual BLER when the QSI signal is not orthogonal

Table 2.2: Simulation parameters

| **eNB Parameters** | **Value** |
|---|---|
| Antenna Configuration | 2Tx × 1Rx |
| Number of downlink RBs | 6 |
| PHICH duration | Normal |
| PHICH Group Multiplier | $\frac{1}{6}$ |
| System Frame Number | randi([0 255]) |
| Cell ID | 0 |
| No. PDCCH symbols, $m$ | 2 |
| **UE Parameters** | **Value** |
| Antenna Configuration | 1Tx × 1Rx |
| VCO accuracy | 10ppm |
| DRX cycle length, $t_{\text{DRX}}$ | [1.28 s, 2.56 s, 10.24 s, 1 min, 10 min] |
| Drift time, $t_{\text{Drift}}$ | VCO accuracy × $t_{\text{DRX}}$ |
| ON time for paging decode, $t_{\text{Paging}}$ | 1 ms (normal coverage) 10 ms (CE mode) |
| ON state power, $P_{\text{ON}}$ | 500 mW |
| "Light Sleep" power, $P_{\text{LS}}$ | 250 mW |
| "Deep Sleep" power, $P_{\text{DS}}$ | 0.0185 mW |
| Probability of successful QSI detection, $p$ | 0.9 |
| Probability that QSI indicates "sleep", $q$ | 0.9 |

to the PBCH signal, i.e., for the methods using spreading and repetition or repetition plus FEC. The non-orthogonality of the QSI signal leads to interference with the PBCH signal, which in turn leads to degradation in PBCH BLER performance.

Figure 2.7 indicates the QSI BLER performance. As expected, QSI using orthogonal codes gives the best performance. It would be preferred if the MTC UE can afford to have significant amount of memory to store the different orthogonal QSI sequences. From an implementation perspective, the MTC UEs have a high speed, high cost working memory space and a low speed, low cost permanent memory space. The UEs can store the orthogonal QSI sequences for all the Cell IDs in the perma-

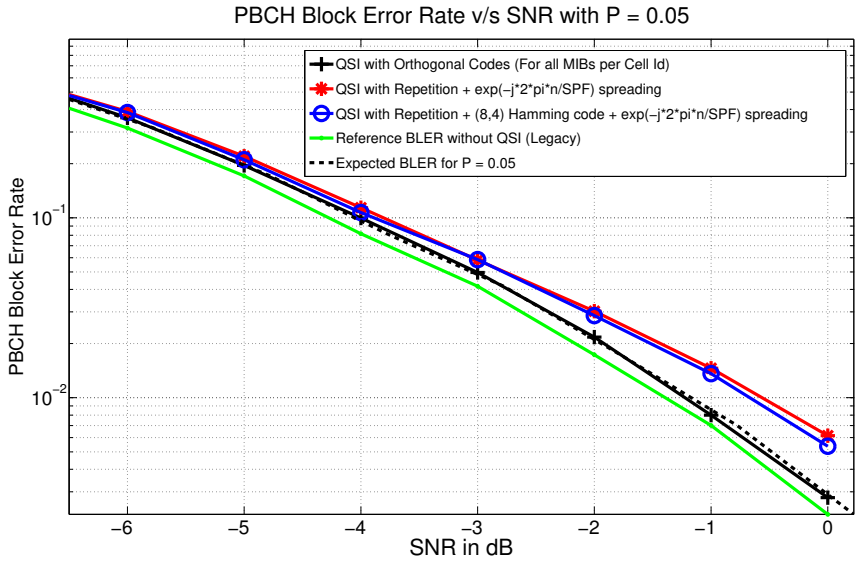


Figure 2.6: PBCH BLER performance for AWGN channel.

nent memory and can have only the sequences corresponding to the detected Cell ID in the working memory so that the low cost feature of the MTC UE is not largely compromised.

It can be seen that QSI methods using repetition coding only and repetition coding with FEC also demonstrate good QSI BLER performance. These methods are straight-forward to implement and unlike the QSI mechanism using orthogonal sequences, these methods do not require extra memory. However, there is about 0.9 dB degradation in PBCH BLER performance at 1% BLER when compared to the legacy UE PBCH BLER performance considering that the total power available for PBCH is unaltered. The degradation will not occur if the eNB can afford extra power for QSI transmission.

Next, the different QSI solutions were simulated using the LTE system toolbox on MATLAB for the Extended Pedestrian A (EPA) channel model with a Doppler Spread of 1 Hz and the number of QSI bits, $M = 4$. This channel model was selected

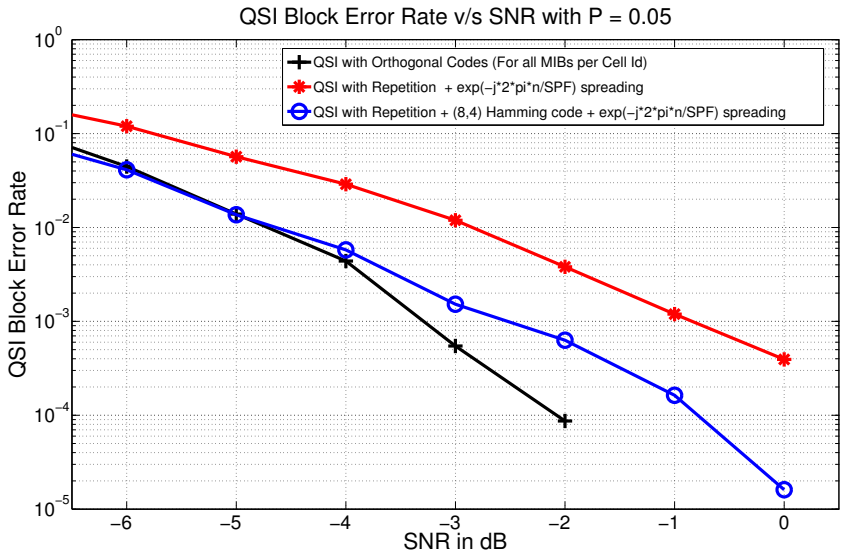


Figure 2.7: QSI BLER performance for AWGN channel.

since it is recommended by the 3GPP for testing low UE mobility [106] and is suitable for the IoT scenarios considered in this work such as pet tracking and weather sensing in the case of normal coverage or patient monitoring in case of enhanced coverage. Other simulation parameters are the same as in Table 2.2.

The QSI solutions for MTC UEs without CE discussed in Section. 2.3 were analyzed using the BLER performance considering the minimum SNR required for 10% BLER ($S_{10\%}$) as the performance indicator. For MTC UEs with CE, we considered 15 dB CE and obtained the operating SNR for the synchronization channel as $-14.2$ dB [43]. We evaluated the performance based on the accumulation time required for 90% detection ($t_{\text{Acc}}$) of the desired signal (PSS/SSS for the legacy UE and the QSI signal for UE with QSI) for false alarm (FA) rates of 10% and 1%. Table 2.3 summarizes the performance results for the different QSI solutions.

The results for QSI on PBCH and QSI on PSS/SSS are shown in Figure 2.8a and Figure 2.8b, respectively. For QSI on PBCH, method 1 corresponds to spreading

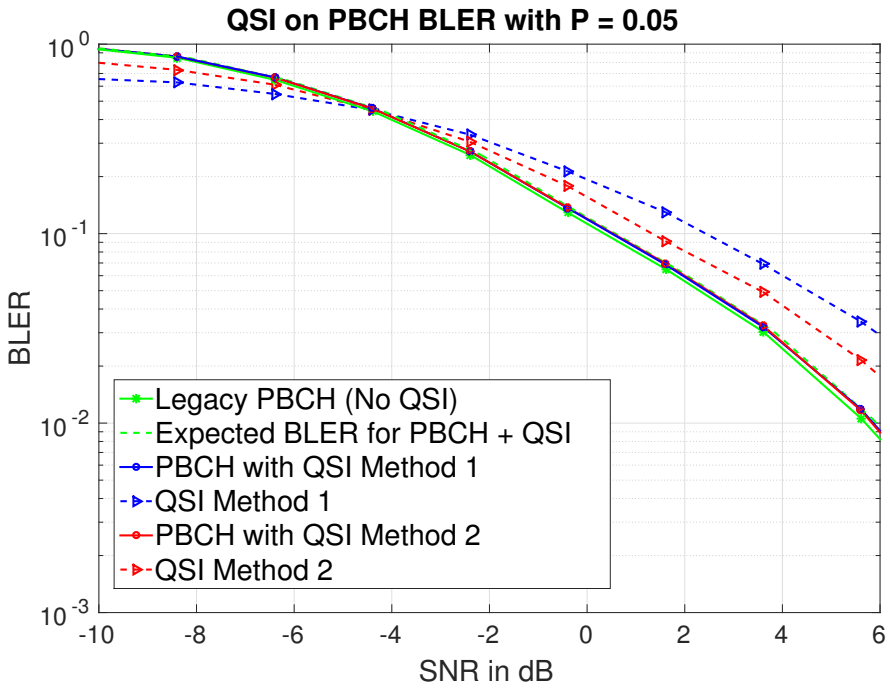


(a) QSI on PBCH

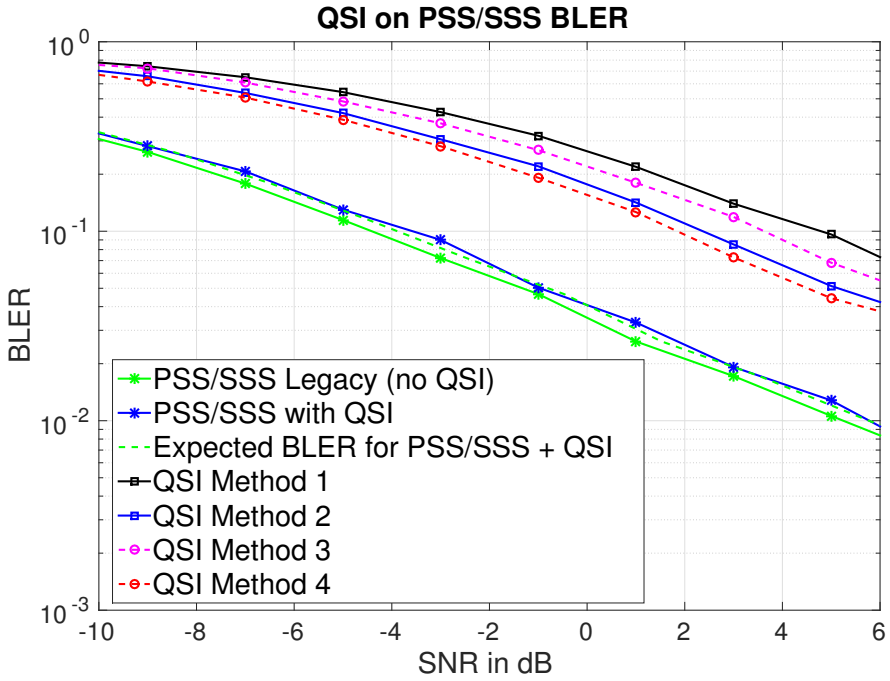


(b) QSI on PSS/SSS

Figure 2.8: Performance results for QSI without CE using the EPA channel model.

Table 2.3: Performance summary using $S_{10\%}$ (without CE) and $t_{\text{Acc}}$ (with CE)

| PBCH $S_{10\%}$ (No CE) | QSI on PBCH (No CE) | PSS/SSS $S_{10\%}$ (No CE) | QSI on PSS/SSS $S_{10\%}$ (No CE) | Legacy PSS/SSS $t_{\text{Acc}}$ (CE) | QSI on PDSCH $t_{\text{Acc}}$ (CE) |
|---|---|---|---|---|---|
| Legacy: 0.35 dB<br>With QSI:<br>Met 1: 0.53 dB<br>Met 2: 0.55 dB | Met 1:<br>2.43 dB<br>Met 2:<br>1.33 dB | Legacy:<br>-4.41 dB<br>With QSI:<br>-3.62 dB | Met 1: 4.79 dB<br>Met 2: 2.37 dB<br>Met 3: 3.62 dB<br>Met 4: 1.85 dB | FA 10%:<br>90 ms<br>FA 1%:<br>200 ms | FA 10%:<br>20 ms<br>FA 1%:<br>50 ms |

QSI using repetition only (see Section 2.3.1.4) and method 2 corresponds to spreading QSI using repetition and FEC (see Section 2.3.1.5). From Table 2.3, we note that the two QSI on PBCH solutions show 0.18 dB and 0.2 dB degradation in PBCH detection performance respectively for 10% BLER, which is close to the expected loss calculated as $10\log_{10}(1-P) = 0.22$ dB with $P = 0.05$ in Section 2.3. For the AWGN channel results, the QSI signal using our proposed methods acted as interference to the PBCH signal and degraded the PBCH detection performance by more than 0.5 dB. The same is true in the current simulation too, but the EPA channel is not a static channel like AWGN and the degradation in PBCH detection performance is not as pronounced as it was for AWGN. For QSI on PSS/SSS, the expected loss in PSS/SSS detection performance when QSI is transmitted on the unused subcarriers is 0.54 dB as computed in Section 2.3. From Table 2.3, we observe that the loss obtained from our simulation is 0.79 dB for 10% BLER, which is close to our expected results.

We observe that for QSI on PBCH using spreading, repetition and (8,4) extended Hamming code (method 2) gives the best performance and for QSI on PSS/SSS, the method of transmitting QSI using the unused carriers of both PSS and SSS along with (8,4) extended Hamming code (method 4) gives the best performance. Comparing the $S_{10\%}$ for these two methods, we can see that QSI on PBCH (method 2) is 0.52 dB better than QSI on PSS/SSS (method 4) owing to the SNR gain due to spreading.

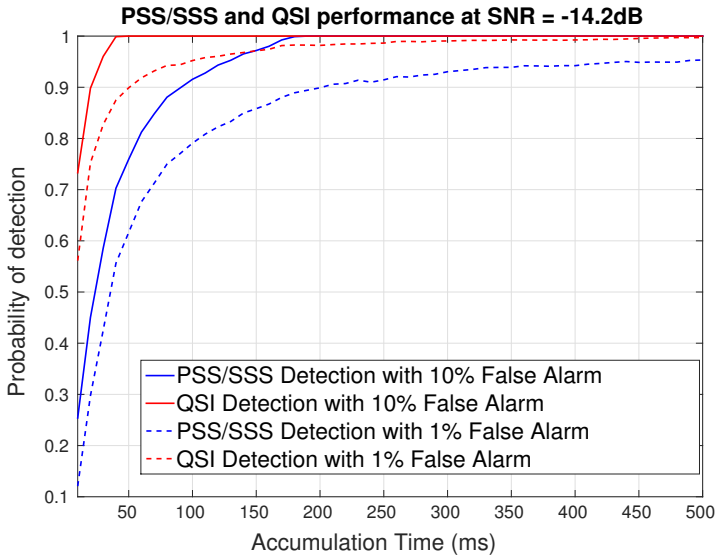


Figure 2.9: Re-Sync and QSI on PDSCH for CE using the EPA channel model.

In the case of MTC UEs with CE, we determined the number of PSS/SSS repetitions required to reacquire the symbol timing when the UE wakes up for the legacy UE. Since we look at the case where the UE had already obtained the cell identifier before it went to sleep, the PSS/SSS is known to the UE. Therefore, the UE need not hypothesize over all combinations of PSS/SSS and has to re-acquire the same PSS/SSS combination which it detected before. Since the SSS and PSS are on consecutive symbols, we considered them as one long sequence and used differential auto-correlation to detect this long sequence and obtain the symbol boundary. A successful detection is registered when we detect the correct symbol boundary, otherwise it is regarded as a false alarm. Similarly, we obtained the QSI detection performance with the QSI transmitted on PDSCH. Figure 2.9 indicates the re-sync performance of the legacy UE and the QSI detection performance for MTC UE with CE. Using the 15dB CE results summarized in Table 2.3, we observe that for the legacy UE requires $t_{\text{Acc}} = 200$ ms (40 PSS/SSS repetitions), while the UE adopting our QSI on PDSCH mechanism requires $t_{\text{Acc}} = 50$ ms (20 QSI repetitions) at a false alarm rate

Table 2.4: Reduction in energy consumption for UE with QSI

| DRX length | QSI on PBCH (No CE) | QSI on PSS/SSS (No CE) | QSI on PDSCH (15 dB CE) |
|---|---|---|---|
| 1.28 s | 45.67% | 51.74% | 63.88% |
| 2.56 s | 44.67% | 50.61% | 63.86% |
| 10.24 s | 39.48% | 44.73% | 63.75% |
| 1 min | 22.52% | 25.52% | 63.05% |
| 10 min | 7.36% | 7.36% | 56.49% |

of 1%. Therefore, the re-acquisition time of the UE is reduced by a factor of 4 at this false alarm rate when our QSI mechanism is adopted, which improves the energy efficiency.

### 2.6.2 Energy Efficiency Results

The energy efficiency is calculated as the ratio of the energy consumed by the UE using our QSI solution to the energy consumed by the legacy UE. The energy consumed by the legacy UE was computed using (2.4) and the energy consumed by the UE using QSI was computed using (2.6) or (2.10) depending on whether it is in normal coverage mode or coverage enhancement mode with the parameters listed in Table 2.2. For QSI on PDSCH, we considered 15 dB CE and used $t_{\mathrm{Q}} = 50$ ms and $t_{\mathrm{Sync}}^{\mathrm{CE}} = 200$ ms corresponding to $t_{\mathrm{Acc}}$ at a false alarm rate of 1%.

Table 2.4 summarizes the reduction in energy consumption obtained by using QSI for different DRX cycle lengths. With the VCO drift of 10 ppm, the UE would require to decode the PBCH if it sleeps more than 8.2 minutes. When PBCH decoding is not required, QSI on PSS/SSS is more energy efficient than QSI on PBCH for MTC UEs without CE. If PBCH decoding is required, the energy efficiency obtained by both the QSI mechanisms is equivalent. For MTC UEs with CE, QSI on PDSCH demonstrates considerable improvement in energy efficiency since the ON time of the

UE is reduced significantly. The energy efficiency is obtained by the reduction in the ON time of the UE which depends on the SNR and not on the length of the DRX cycle. Therefore, at a given SNR, the ratio of ON time to the DRX cycle length decreases with increasing DRX cycle length which leads to a decrease in the energy efficiency.

### 2.6.3 Computational Complexity Results

The computational reduction is calculated as the ratio of the number of FFT computations consumed by the UE using our QSI solutions to that of the legacy UE. We obtained the number of FFT computations for the legacy UE using Eq. (2.11) for normal mode and Eq. (2.12) for coverage enhancement mode. For the UE using our QSI solutions, we obtained the numbers from Eq. (2.13) and Eq. (2.14) for normal mode and CE mode respectively. The number of repetitions, $r_{\text{Sync}}$, $r_{\text{Q}}$ and $r_{\text{PDCCH}}$, were chosen corresponding to $t_{\text{Sync}}$, $t_{\text{QSI}}$ and $t_{\text{Paging}}$ respectively. The computational reduction obtained for different QSI solutions is summarized in Table 2.5. The PDCCH FFT size is directly proportional to the eNB bandwidth while QSI FFT size is always 128 point. Therefore, the computational efficiency increases for higher eNB bandwidths. This is true even for the CE case. Additionally, since the QSI detection requires a lesser number of repetitions than legacy PSS/SSS detection, the computational efficiency obtained for the CE case is higher than that for the non-CE case.

It should be noted that along with the full scale FFT, PDCCH message block decoding also requires Viterbi decoding and hypothesizing over 44 different possible locations, which is computationally intensive, but the QSI either uses correlation with $2^M$ different sequences or uses simple despreading and repetition combining (plus ML

Table 2.5: FFT computation reduction for UE with QSI

| eNB Bandwidth | FFT Size (No CE) | QSI on PBCH or PSS/SSS (No CE) | QSI on PDSCH (15 dB CE) |
|---|---|---|---|
| 1.4 MHz | 128 | 10.69% | 65.15% |
| 5 MHz | 512 | 36.21% | 65.73% |
| 10 MHz | 1024 | 53.02% | 66.55% |
| 20 MHz | 2048 | 66.88% | 68.12% |

decoding for $2^M$ sequences in case of FEC), which are simpler methods compared to PDCCH blind decoding. This leads to further improvement in computational savings.

## 2.7 Conclusion

In this chapter, we considered the problem of improving the current DRX and paging mechanism for energy efficient IoT using LTE/LTE-A. We proposed a modified DRX mechanism incorporating quick sleeping as a novel, simple and efficient solution for this problem. For the MTC UEs in normal coverage, we proposed QSI on PBCH and QSI on PSS/SSS mechanisms which do not require additional resources. For UEs requiring extended coverage, we introduced the QSI mechanism using dedicated resources on PDSCH. The different QSI solutions were simulated on the EPA-1 Hz channel model to address the case of low-mobility. We also determined the reduction in energy consumption and computational complexity for the MTC UEs using our QSI mechanisms when compared to the legacy UEs. For MTC UEs without CE using our QSI solutions, we showed 45% and 66% reduction in energy consumption and computational complexity respectively. For MTC UEs with 15 dB CE using QSI on PDSCH, we demonstrated that we could obtain 63% reduction in energy consumption and 68% reduction in computational complexity.

Our QSI solutions are in line with the standardization activities for MTC in

3GPP LTE/LTE-A to facilitate IoT and have minimal influence on the legacy UEs. The specific QSI solutions provided in this chapter are suitable for CAT-M1, CAT-0 and above UE categories, since they operate on a bandwidth of at least 1.4 MHz. However, the main idea behind the QSI, i.e., simplifying the paging decode process when there is no valid page and reducing the resynchronization time of MTC UEs, is applicable to all UE categories and would essentially aid the design of a more efficient paging and power saving mechanisms in the downlink for the forthcoming 5G NR standard.

# Chapter 3

# Enhanced Primary Synchronization Signal (ePSS)

## 3.1 Introduction

In a typical wireless communication system, it is important for the mobile device, or the so called UE to maintain accurate symbol timing synchronization with the base station in order to decode the downlink data. In the previous chapter, the timing resolution considered was at the symbol level, i.e., the timing was designated to be correct if the MTC UE supporting the IoT finds the correct symbol number. In this chapter, we examine the sensitivity of the paging decode operation to the timing offset and show that any deviation in timing beyond the CP length considerably degrades the decoding process.

Conventionally, in OFDM based systems, the UEs reacquire the timing using CP autocorrelation [63,64] and/or by detecting the synchronization reference signals [107–110] which are transmitted periodically by the base station. In this chapter, we show that the legacy methods for resynchronization using CP autocorrelation and reference signal detection are not effective for the Low-Cost, Low-Complexity, Low-Coverage (LC) MTC devices due to the increased ON time of the UE.

For faster timing reacquisition during the DRX wake-up interval, we introduce our novel enhanced Primary Synchronization Signal (ePSS) as the resynchronization

signal for the LC devices and demonstrate the reduction in energy consumption when the ePSS is used. Further, we also adopt DRX with QSI mechanism from Chapter 2 and illustrate that using the ePSS as QSI combines the advantages of faster timing reacquisition and quicker transition to sleep mode when there is no page, begetting further improvement in the energy efficiency of the LC devices.

As before, we ensure that our solutions are designed such that the changes required to the current LTE/LTE-A standards are kept minimal and the resource allocation respects the procedure followed in the current standards.

The rest of the chapter is outlined as follows. In Section 3.2, we demonstrate the importance of timing reacquisition for the LC devices and explore the conventional mechanisms for timing reacquisition. In Section 3.3, we describe the design and resource allocation aspects of our proposed ePSS mechanism and discuss how the ePSS can also be used as QSI to reduce the ON time of the MTC UE. In Section 3.4, we compare the detection performance of our ePSS signal and the legacy synchronization signals (PSS/SSS) and illustrate the energy efficiency obtained when our ePSS is adopted by the LC devices in DRX. The conclusions are drawn in Section 3.5.

## 3.2 UE Timing Accuracy and Legacy Timing Acquisition Algorithms

As discussed in Section 1.2.1, the paging message consists of the P-RNTI on the PDCCH, followed by the paging data on the PDSCH. The performance of the PDCCH and the PDSCH has been analyzed in many prior works. For example, in [111], the PDCCH performance is analyzed for M2M traffic and the scenario of excess load on the PDCCH due to large number of MTC devices is discussed. In [112]

and [113], the PDCCH BLER performance is analyzed for various channel models and the PDSCH BLER performance is discussed in [114]. These works assume perfect timing synchronization. However, the LC devices waking up to decode the paging message will have a clock drift depending on the quality of the oscillator used for the UE's clock.

If the UE uses a high quality oscillator, the timing drift will be small. This means that the UE can sleep for a longer duration without losing the timing synchronization. Typically, mobile devices like smartphones using a high quality Voltage Controlled Temperature Compensated Crystal Oscillator (VCTCXO) have an accuracy of ±1 ppm [115]. But, the low-complexity MTC UEs cannot incorporate a high quality oscillator for its clock since it increases the cost of the device. Hence, most of them use a VCO for their clock, which has an accuracy of ±10 ppm [116]. As an example, assuming that the symbol time is 72 $\mu$s and the tolerable timing drift is 5%, i.e. 3.6 $\mu$s, the MTC UE with a 10 ppm accurate clock can sleep up to $\frac{3.6\mu s}{10.10^{-6}} = 0.36$ s= 360 ms, while the device with a 1 ppm accurate clock can sleep up to $\frac{3.6\mu s}{1.10^{-6}} = 3.6$ s. However, the sleep time supported by the network can be longer. For example, in LTE/LTE-A, the sleep time supported by the network has been recently extended to 2621.44 s (43.69 minutes) [56]. Therefore, the assumption of perfect timing synchronization is not always true for both types of devices and timing reacquisition becomes important for successful communication between the UE and the eNB.

In this section, we first demonstrate the sensitivity of the PDCCH/PDSCH paging decode operation to the UE timing offset. Then, we explore the timing estimation and synchronization algorithms used widely in OFDM based systems. We examine the performance of two algorithms - a) CP autocorrelation [63,64] and b) Synchronization

Table 3.1: Simulation settings for Figure 3.1.

| Parameter | Setting |
|---|---|
| Downlink Bandwidth | 1.4 MHz |
| Sampling Rate | 1.92 MHz |
| Antenna Configuration | $2 \times 1$ |
| Channel Model | EPA |
| Max. Doppler Shift | 1 Hz |
| MIMO Correlation | Low |
| PDCCH Settings | Type = Format 2<br>RNTI used = P-RNTI<br>DCI Format = 1A |
| PDSCH Settings | MCS = 0<br>TBS = 16 bits<br>Number of PRBs = 1 |

signal detection [107–110] and determine their suitability for low-complexity MTC UEs in CE mode. The LTE toolbox in MATLAB was used for the simulations. The EPA 1 Hz channel was chosen since it is the recommended channel model to study the performance of MTC in LTE/LTE-A [43, 106] because it models the low mobility multi-path scenario quite well. Especially for the MTC UEs in low coverage, the 3GPP envisions the scenario where a significant portion of these devices are located in basements of buildings or underground parking lots and are mostly stationary, which is well characterized by the EPA 1 Hz channel model [43, 106]. The CFO value for timing reacquisition was chosen to be 1 kHz [43]. But for the PDCCH and the PDSCH decoding, the CFO was set to 100 Hz, since the initial CFO will be estimated and compensated after timing reacquisition and one has to account only for the residual CFO [43]. The other important simulation parameters are summarized in Table 3.1.

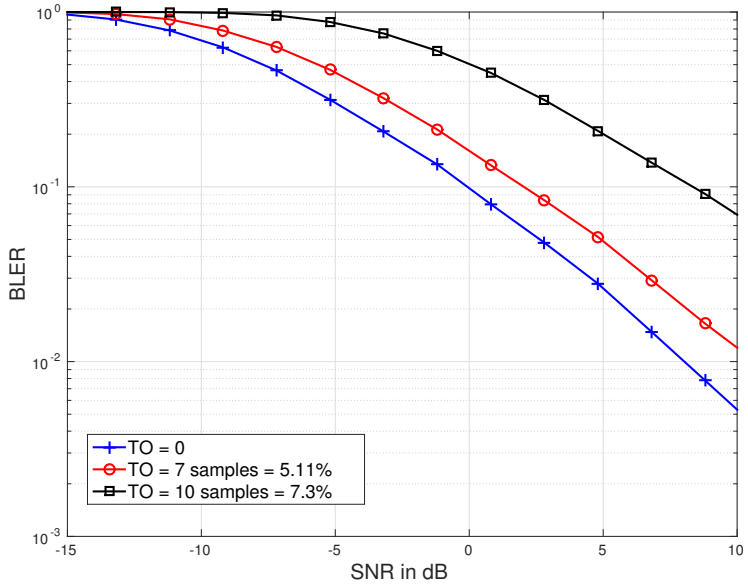


(a) PDCCH BLER performance

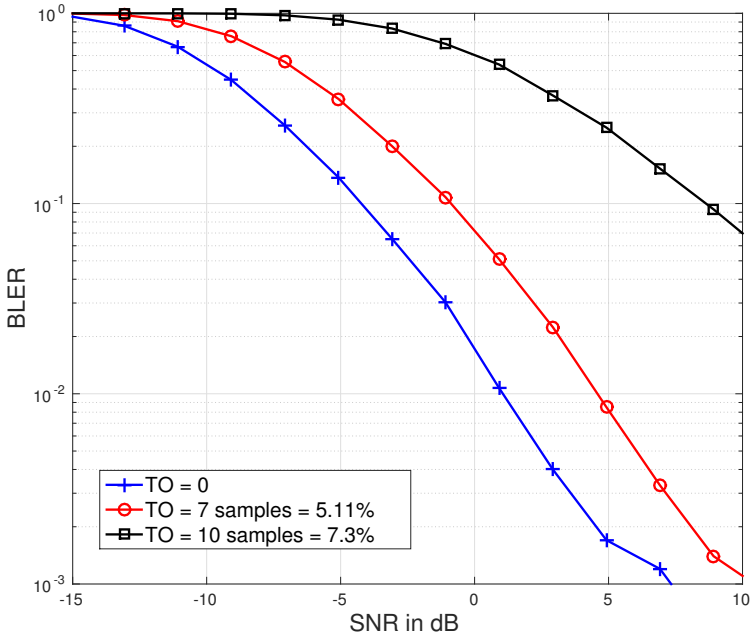


(b) PDSCH BLER performance

Figure 3.1: Illustration of the sensitivity of the PDCCH and the PDSCH decoding to timing offset (TO).

### 3.2.1 Importance of UE Timing Accuracy

The first step of the paging decode process is to check for the P-RNTI by decoding the PDCCH. If the P-RNTI is found, the UE decodes the PDSCH to check for the paging data. Otherwise, it goes back to sleep. It is important to analyze the sensitivity of the PDCCH and the PDSCH performance with respect to UE timing accuracy. Similar to the previous works in [113, 114], we use the BLER as the metric for analyzing the performance the PDCCH containing the P-RNTI and a PDSCH block containing paging data.

Figure 3.1a and Figure 3.1b demonstrate the BLER performance of the PDCCH and the PDSCH respectively. It is evident that both the PDCCH and the PDSCH are highly sensitive to timing offset. We consider the 10% BLER point to analyze the performance as suggested in [43] for LTE/LTE-A MTC. At 10% BLER, the PDCCH performance is degraded by about 8 dB for as little as 7.5% error in timing estimation and the corresponding degradation in the PDSCH performance is 12 dB. However, when the timing estimate is within 5% of the actual value, the degradation is less than 3 dB in both the cases. Therefore, the accuracy of UE timing plays a vital role in the success of the paging decode mechanism in LTE/LTE-A. Additionally, for the LC devices, the timing reacquisition algorithms would be required to provide accurate results at very low SNR. Next, we discuss the performance of legacy timing estimation algorithms for the LC devices operating at low SNRs.

### 3.2.2 Timing Reacquisition Using CP Autocorrelation

In this method, the symbol start position is obtained by finding the location of the peak of the CP autocorrelation [58, 63, 64]. For the illustration of the performance of CP autocorrelation, we accumulate the correlation results only on the symbols

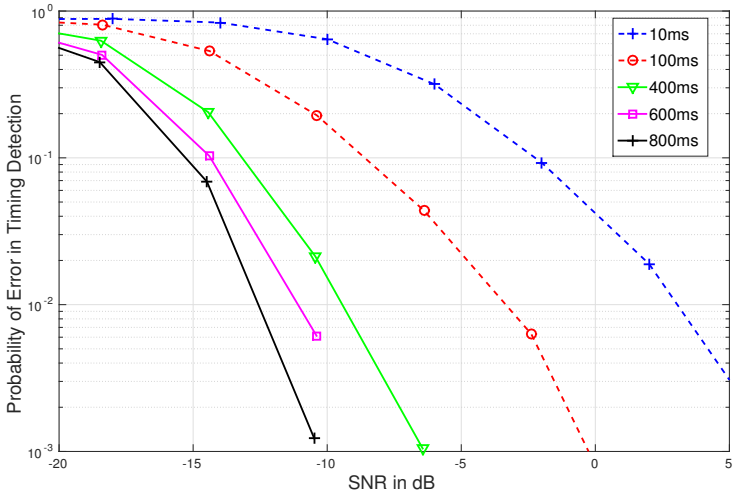


Figure 3.2: CP autocorrelation performance.

that are used to transmit the pilot signal. This is because the pilot signal is always transmitted on specific symbols regardless of whether the eNB has data or control information to send. However, on the other symbols, the subcarriers contain a valid signal only when they are used for control or data allocation. The pilot signal is transmitted on the first and fifth symbol of each slot (see Figure 1.2a) [58, 61].

Figure 3.2 depicts the performance of CP autocorrelation for different accumulation times. For the LC devices, the operating SNR for the synchronization channel at 10% BLER is -14.2 dB [43] and the error tolerance level of the estimated timing offset is set to ±5% based on the results obtained in Section 3.2.1. From Figure 3.2, we observe that about 600 subframes (corresponding to 600 ms) of accumulation time is required for 10% BLER at -14.2 dB which is large. This is because there are only 9 CP samples available for correlation at a sampling rate of 1.92 MHz (the sampling rate supported by the low-complexity MTC UEs [43]). This means that the MTC UE has to be on for 600 ms, which will lead to increased energy consumption. Therefore, we conclude that the classical method of CP autocorrelation is not an efficient

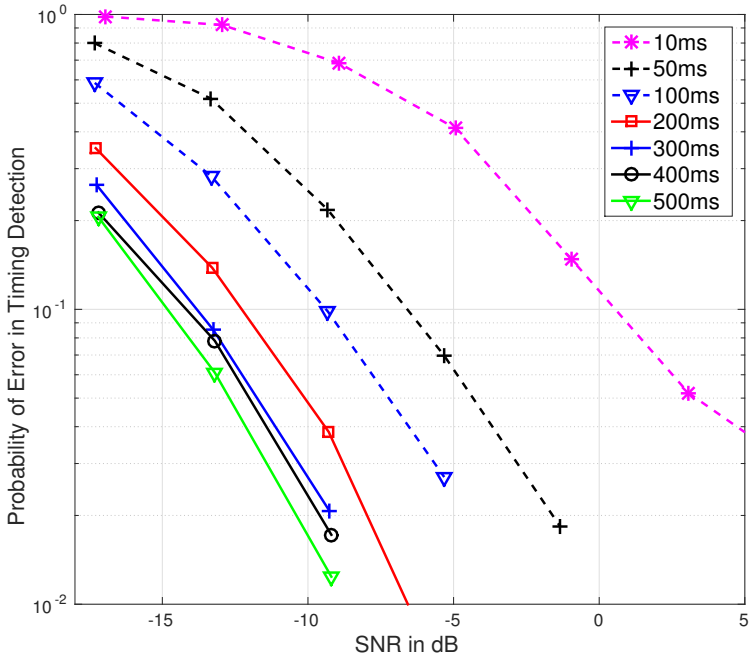


Figure 3.3: PSS/SSS detection performance.

mechanism for timing reacquisition for low-complexity MTC UEs in CE mode.

### 3.2.3 Timing Reacquisition Using Synchronization Signal Detection

For the synchronization signal detection, we consider the PSS and the SSS as one long sequence, since they are on consecutive symbols. For successful timing acquisition, we have to find the position of this sequence in a 10 ms radio frame within a tolerance level (set to $\pm 5\%$ in our implementation similar to Section 3.2.2). We use differential autocorrelation in frequency domain to detect the synchronization signal [107, 108].

Figure 3.3 gives the performance results for timing reacquisition using the legacy synchronization signal detection. Considering 10% BLER at the coverage enhancement SNR of -14.2 dB [43], we require around 400 ms, i.e., 80 repetitions of the legacy

synchronization signal to detect the correct timing offset. This is again significant, resulting in increased energy consumption of the UE. Therefore, we require a faster resynchronization mechanism to improve the energy efficiency of the LC devices.

## 3.3 Technicalities of the ePSS

In this section, we introduce our new, simple resynchronization signal specially catering the needs of the LC devices. Since this signal is designed similar to the PSS, it would be apt to call it the enhanced PSS (ePSS). We discuss the design and resource allocation aspects of our ePSS mechanism.

### 3.3.1 ePSS Design

The ePSS signal should be designed such that the MTC UE can detect it with considerable accuracy at very low SNRs (around -14 dB). Since the ePSS is used by LC devices, which have limited processing capabilities, it should be designed to provide robust detection with minimal complexity. This requires the ePSS signal to possess good autocorrelation and crosscorrelation properties. Such properties are demonstrated by the ZC sequences that are extensively used in the LTE/LTE-A standards, for example, in the case of the PSS in the downlink and the Physical Random Access Channel (PRACH) in the uplink. The ZC sequences are such that their cyclically shifted versions are orthogonal to each other and the crosscorrelation of two $N$ length ZC sequences is limited by $\frac{1}{\sqrt{N}}$ [58]. These properties make them the perfect candidates for the ePSS signal design.

Also, the location of the ePSS in the LTE/LTE-A radio frame should be such that the UE can unambiguously determine the subframe number upon successful detection, which necessitates the ePSS to occupy exclusive and invariable resources

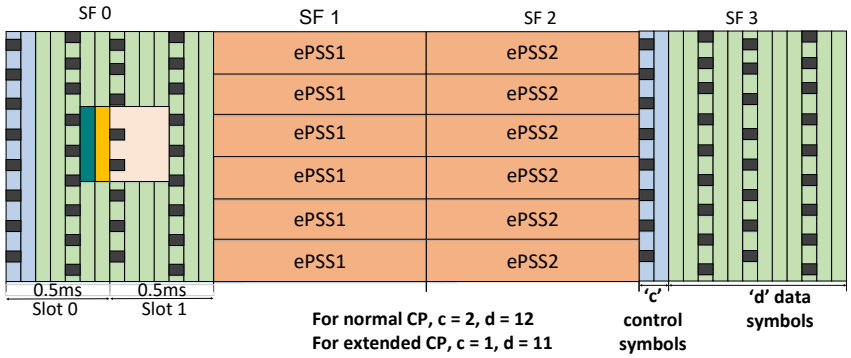


(a) ePSS subframe structure

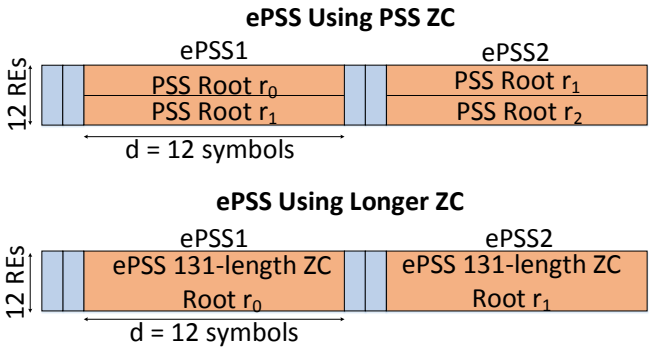


(b) Normal CP - Using only data symbols

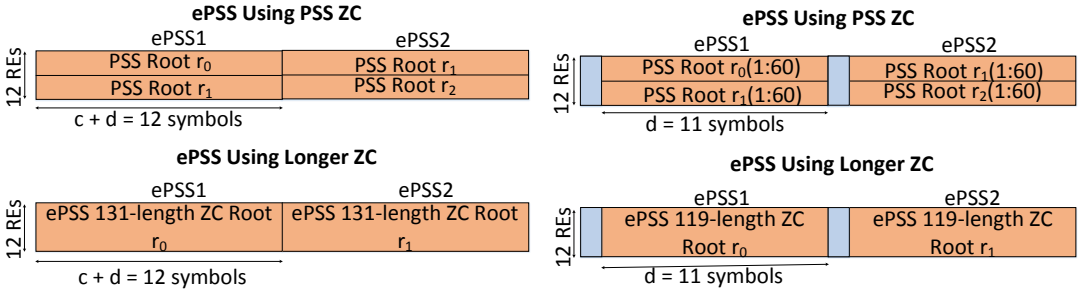


(c) Extended CP - Using both control and data symbols

(d) Extended CP - Using only data symbols

Figure 3.4: Illustration of ePSS subframe structure for normal and extended CP.

in time and frequency. In order to obey the mandate of resource allocation dictated by the current LTE/LTE-A framework, such dedicated resources can be accommodated only in the PDSCH space. The number of symbols available for the PDSCH is decided by the eNB.

We use the PDSCH on subframes 1 and 2 for transmitting the ePSS, so that its location is fixed in time as shown in Figure 3.4a. In LTE/LTE-A with normal CP, a subframe consists of 14 symbols. A Resource Element (RE) spans 1 subcarrier $\times$ 1 symbol and a PRB consists of 12 REs $\times$ 7 symbols = 84 REs. The minimum unit of allocation spans 12 REs $\times$ 1 subframe, which corresponds to a pair of PRBs = 168 REs. A commonly used configuration for LTE/LTE-A MTC using normal CP is a subframe consisting of a 12 symbol PDSCH preceded by a 2 symbol PDCCH [43]. In this scenario, there are 168 - 2 $\times$ 12 = 144 REs per PRB pair available for the PDSCH. Also, some REs in the PDSCH are reserved for pilot signals, which is 12 REs per PRB pair in this case. This gives us 132 REs per PRB pair for the PDSCH.

In the extended CP case, a subframe consists of 12 symbols and the minimum unit of allocation spans 12 REs $\times$ 1 subframe = 12 $\times$ 12 = 144 REs. As in the case of normal CP, 12 REs per PRB pair are required for pilot signal transmission. Hence, the total number of REs available per PRB pair is 144-12 = 132 REs. Typically, one symbol is used for the PDCCH [43]. Therefore, we have 132 - 12 = 120 REs available for the PDSCH for the extended CP case.

In the following, we present two methods to design the ePSS - a) Using multiple PSS and b) Using longer ZC sequences. The ePSS detection uses differential autocorrelation similar to the legacy synchronization signal detection mechanism discussed in Section 3.2.3.

#### 3.3.1.1 ePSS Construction Using Multiple PSS

In this method, the ePSS is formed by a burst of PSS copies occupying the REs in the PDSCH space. The advantage of re-using the existing PSS sequences is that they are readily available at the eNB and no additional processing/memory is required to generate/store a new sequence. An example for such an ePSS for normal CP

is shown in Figure 3.4b. An ePSS PRB consists of the concatenations of two PSS sequences of different roots. Unlike the regular PSS where the ZC sequence is spread across frequency, the PSS ZC sequence within our ePSS is spread across time (see Figure 3.4b). This ensures that the legacy UEs do not falsely detect this signal as the PSS. The PSS signal is a 63-length ZC sequence [58] and two such sequences will occupy 126 REs. The unused REs are set to zero. The low-complexity MTC UEs can operate on a maximum downlink bandwidth of 1.4 MHz which corresponds to 6 PRBs. Therefore, we transmit 6 copies of the ePSS in a subframe which is equivalent to transmitting 12 PSS copies.

In the ePSS design, we cannot have the same signal on both subframe 1 and subframe 2, since the ePSS will be used for timing resynchronization. If these two subframes have the same signal, the UE would not be able to uniquely determine the subframe number. Therefore, we have to judiciously re-use the PSS sequences so that the two subframes are different, but can be detected together to uniquely determine the subframe number. The LTE/LTE-A standards use 3 roots for the PSS sequence - $r \in [r_0 = 25, r_1 = 29, r_2 = 34]$. Each ePSS sequence consists of 2 of the 3 possible PSS roots. This gives us 6 possible ways to choose the roots for subframe 1. They are $(r_0, r_1)$, $(r_0, r_2)$, $(r_1, r_0)$, $(r_1, r_2)$, $(r_2, r_0)$ and $(r_2, r_1)$.

Let us say that subframe 1 has the sequence $(r_0, r_1)$ and call $r_0$ the top root and $r_1$ the bottom root. Since the ePSS is used for timing reacquisition, if both the subframes contain the same top and bottom roots, the UE using the ePSS to detect the timing will not know whether it detected the root on subframe 1 or on subframe 2. Therefore, we should have different sequences on subframe 1 and subframe 2. Hence, subfame 2 can only have $(r_1, r_0)$, $(r_1, r_2)$ or $(r_2, r_0)$ as the sequence. Similarly, if we start with a different sequence for subframe 1, we have 3 possibilities for subframe

2. Thus, in total we have $6 \times 3 = 18$ sequences to construct the ePSS using this method.

Moreover, there are only 3 legacy PSS sequences and one sequence is used per sector. Therefore, the frequency reuse for the legacy scheme is 3, which may result in the detection of the neighbour PSS. However, for ePSS constructed using this method, we have 18 possible sequences (greater than 7). Therefore, the ePSS can be used with a frequency re-use factor of 7, which reduces the probability of the neighbour ePSS detection.

For the extended CP case, the ePSS transmission uses one of the following schemes - a) using both the control and data symbols (as shown in Figure 3.4c) and b) using only the data symbols (as shown in Figure 3.4d). In the first scheme, there are 132 REs available per PRB pair (since the control symbols are also used) and the ePSS sequences are the same as that for normal CP. However in the second scheme, there are 120 REs available per PRB pair and the ePSS sequences are slightly shortened so that they can be accommodated within the available space with negligible loss in performance.

#### 3.3.1.2 ePSS Construction Using Different ZC Sequences

In this method, we use ZC sequences for the ePSS which are different from those used for the PSS. The ZC sequence is of the form $\mathrm{ZC}(r) = \mathrm{e}^{\left(\frac{-j\pi rn(n+1)}{N}\right)}$, where $n = 0, 1, \cdots N-1$, $r$ is the root of the ZC sequence and $N$ is the length. The root $r$ and the length $N$ are co-prime. As discussed earlier, for the PSS, $N = 63$ and $r \in [25, 29, 34]$. There are 33 more roots that are co-prime to 63 which can be used to construct different ZC sequences. The ePSS can be then constructed as described in Section 3.3.1.1.

Our second solution for using different ZC sequences consists of using a longer

length sequence for the ePSS. For example, in our scenario of using a PDSCH with 132 REs per PRB, we can use a ZC sequence of length 131 and set the single unused RE to zero. Also, using a longer length sequence provides a larger set of sequences since the number of roots co-prime with the length increases. Moreover, the cross-correlation between two ZC sequences is proportional to $\frac{1}{\sqrt{N}}$ and a longer length sequence should improve the performance. Figure 3.4b also depicts the construction of the ePSS using longer length ZC sequences for the normal CP case. Figure 3.4c and Figure 3.4d demonstrate the two ePSS transmission schemes for the extended CP case, where the former scheme uses the same 131-length ZC sequences as that of the normal CP and the latter uses a 119-length shortened ZC sequences.

Similar to Section 3.3.1.1, the signals on subframe 1 and subframe 2 should be different so that the MTC UE can clearly identify the subframe number on resynchronization. With a 131 length sequence, we have 130 possible roots and 130 $\times$ 129 = 16,770 sequences. This gives us a large set of sequences to choose for the ePSS signal design. Again, such an ePSS can also be used with a frequency re-use factor of 7 due to the availability of multiple sequences, which reduces the probability of detecting a neighbour ePSS.

### 3.3.2 ePSS Allocation

The ePSS will be used for resynchronization of the MTC UE with the same cell. Hence, the location(s) of the ePSS in the LTE frame structure should be known by the UE beforehand. Therefore, the ePSS cannot be scheduled using the PDCCH or the enhanced PDCCH (ePDCCH) [117]. We propose the following allocation schemes.

- **ePSS on centre band**: This is a fixed allocation scheme where the REs used for the ePSS always correspond to the centre band occupying 1.4 MHz. The

location of the ePSS in time is already fixed, i.e., on subframes 1 and 2 and it is transmitted every $t_{\mathrm{p}}$ seconds. This method is advantageous for the UE, because there is no additional signaling to indicate the location of the ePSS. The disadvantage is that it limits the flexibility of resource allocation optimization at the eNB, because it cannot use the ePSS REs for other data allocation at any scheduling interval.

- **ePSS on any contiguous band spanning 1.4 MHz**: In this variant of ePSS allocation, we use any contiguous band spanning 1.4 MHz within the available bandwidth at the eNB for the ePSS. The location of the ePSS can be broadcast within a System Information Block (SIB), which will be decoded by the UE when it connects to the cell initially and is updated every 3 hours [58]. This is feasible because the ePSS is only used for resynchronization, i.e., whenever the device wakes up from DRX and reacquires the timing. The initial synchronization is still done using the legacy synchronization signals. After initial synchronization, the device can decode the SIB, which will convey the ePSS location. Another way of conveying the location of the ePSS would be through higher layer signaling. Here, the initial location of the ePSS is obtained from SIB, but the subsequent location is indicated to the UE via higher layer signaling. This gives more flexibility for the eNB to optimize the resource allocation process.

### 3.3.3 ePSS as Quick Sleeping Indication (QSI)

Besides the time consumed by the MTC UE for resynchronization, it is highly possible that the UE can spend a significant amount of time and power trying to decode the paging control information on the PDCCH. This is because the LC devices require

multiple repetitions to successfully decode the paging control information due to very low operating SNR.

The DRX procedure necessitates the UE to wake-up and look for paging during each PO. However, the probability that a UE is paged on every PO instance is very low since the network consists of a large number of UEs. This problem is alleviated by the QSI mechanism for energy efficient DRX operation (discussed in Chapter 2). The QSI mechanism assumes that the UEs are categorized into multiple groups. The QSI signal will indicate "sleep" if there is no impending page for the UE group, otherwise it will indicate "stay-awake". The UE decodes the QSI and attempts to decode the paging information only if the QSI indicates "stay-awake". Otherwise, it goes back to sleep immediately and saves power.

The earliest phase to indicate the presence or absence of a page is when it is resynchronizing with the eNB. Therefore, it would be beneficial if the resynchronization signal can also serve as the QSI signal. The ePSS signal presented in the previous section can fulfill this role as follows.

- The LC devices are divided into $N_{\text{grp}}$ groups and assigned a pair of ePSS patterns denoted by $(ePSS_0, ePSS_1)$.
- The eNB schedules the POs one group at a time. It transmits $ePSS_0$ if the UE group is not paged in the subsequent PO. Otherwise, it transmits $ePSS_1$.
- When the UE attempts to resynchronize with the eNB, it hypothesizes over the two assigned patterns and detects one of them. If it detects $ePSS_0$, the UE interprets that there is no upcoming page in the PO and goes back to sleep immediately. If it detects $ePSS_1$, then it remains awake to decode the paging message.

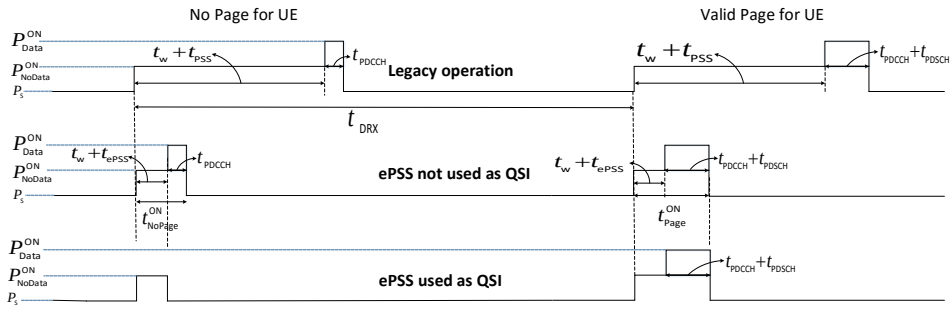


Figure 3.5: Illustration of ON time and sleep time for UEs using the legacy and the ePSS based resynchronization mechanisms.

Hence, the ePSS pattern can also serve as the QSI enabling the UE to resynchronize and go back to sleep quickly when there is no valid page.

Figure 3.5 depicts the UE sleep and wake-up durations for the legacy mode of operation, when it uses the ePSS only for resynchronization (not as QSI) and when it uses the ePSS also as the QSI. The notations $t_{\mathrm{DRX}}$, $t_{\mathrm{PDCCH}}$ and $t^{\mathrm{ON}}_{\mathrm{NoPage}}$ denote the length of UE DRX cycle, the ON time of the UE to decode the PDCCH and the total ON time of the UE when there is no page respectively. Since our ePSS mechanism is designed to provide faster timing reacquisition, the ON time of the UE decreases when it uses the ePSS for resynchronization instead of the legacy synchronization signal. Also, the UE ON time further reduces by a factor of $\frac{t_{\mathrm{PDCCH}}}{t^{\mathrm{ON}}_{\mathrm{NoPage}}}$ when the ePSS is also used as the QSI. A detailed discussion on the performance analysis of the ePSS is presented in the next section.

## 3.4 Performance Analysis

In this section, we analyze the detection performance of our ePSS mechanism and demonstrate that it is better than the legacy synchronization signal detection mechanism. We also provide a simple model based on the ON time to compute the energy

consumption of the UE and show that the UEs adopting the DRX mechanism along with our ePSS for timing resynchronization consume much lesser energy than the UEs using the current DRX mechanism with legacy synchronization signal detection for resynchronization.

### 3.4.1 Reacquisition Performance Analysis

The ePSS solutions discussed in Section 3.3 were simulated with the settings listed in Table 3.1 and a CFO of 1kHz. The SNR considered for this simulation is -14.2 dB, which corresponds to the operating SNR for the MTC UEs that require 15 dB coverage enhancement [43]. The detection threshold is set such that the false alarm rate is limited to 1%. Figure 3.6 shows the performance of the legacy synchronization signal detection scheme and our two ePSS design schemes (refer to Sections 3.3.1.1 and 3.3.1.2) along with the case where the ePSS is also used as the QSI (refer to Section 3.3.3). It is observed that the ePSS designed using longer length ZC sequences performs slightly better than the ePSS designed by re-using the PSS ZC sequences. As discussed in Section 3.3.1.2, the longer length ZC sequence has better cross-correlation properties that results in better performance.

In order to analyze the performance, we consider the accumulation time required for 90% detection denoted by $t_{\text{acc}}$. We note that the legacy synchronization signal detection requires $t_{\text{acc}} = 420$ ms that corresponds to 84 legacy synchronization signal repetitions, since it is transmitted every 5 ms. In this simulation, the ePSS is transmitted on subframe 1 and subframe 2 of the radio frame. This set of two subframes is denoted as "ePSS Block". For the ePSS constructed using multiple PSS (refer to Section 3.3.1.1), $t_{\text{acc}} = 30$ ms that corresponds to 3 ePSS Blocks and for the ePSS constructed using longer length ZC sequences (refer to Section 3.3.1.2), $t_{\text{acc}} = 20$ ms

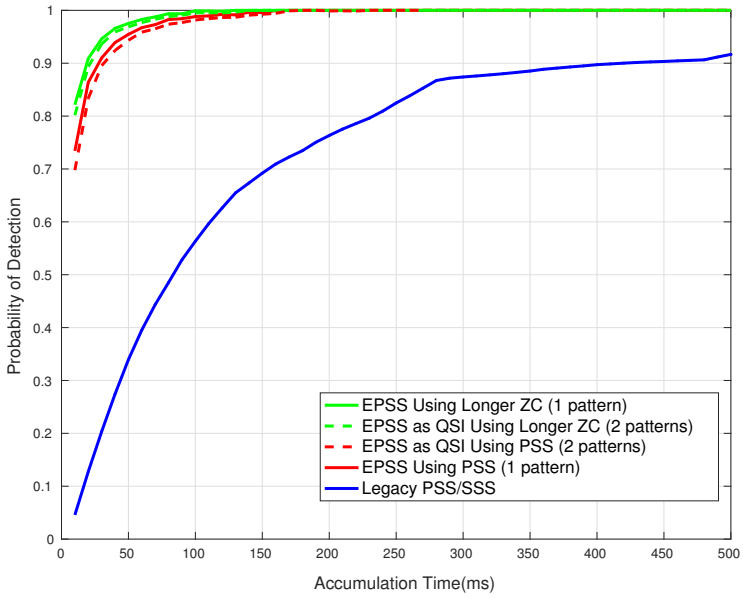


Figure 3.6: Performance of legacy synchronization signal detection and ePSS detection.

corresponding to 2 ePSS blocks. Also, it is evident that there is negligible degradation in performance when the ePSS is also used as the QSI for both the mechanisms. The ePSS detection consumes less than 10% of the time taken by legacy synchronization signal detection for the LC devices, which decreases the ON time of the UE significantly and reduces the energy consumption.

### 3.4.2 Energy Efficiency Analysis

Now we analyze the energy consumption of the UE following the DRX mechanism when it uses the legacy synchronization signal detection for resynchronization and compare it to the energy consumption of the UE when it uses our ePSS solutions. In this work, we look at energy consumption from the physical layer perspective and consider a simple model for our energy consumption calculation based on two quantities - a) ON time of the UE and b) sleep time of the UE similar to [89].

Let $t_{\mathrm{w}}$ and $t_{\mathrm{r}}$ denote the time taken for the UE RF warm-up and the time taken for the UE resynchronization respectively. The UE ON time for the PDCCH decode and the ON time of the PDSCH decode are denoted by $t_{\mathrm{PDCCH}}$ and $t_{\mathrm{PDSCH}}$ respectively. $P_{\mathrm{ON}}$ and $P_{\mathrm{S}}$ represent the power consumed by the UE during the ON time and the sleep time respectively. In order to decode a page, the UE warms up, resynchronizes with eNB and decodes the PDCCH to check for a page. If the PDCCH contains P-RNTI, the UE attempts to decode the paging data on the PDSCH. Otherwise, it goes back to sleep. Hence, the total ON time of the UE depends on whether it received a page or not. When the UE has a valid page, the ON time (see Figure 3.5) is given by $t^{\mathrm{ON}}_{\mathrm{Page}} = t_{\mathrm{w}} + t_{\mathrm{r}} + t_{\mathrm{PDCCH}} + t_{\mathrm{PDSCH}}$ and the corresponding energy consumed is given by

$$E^{\mathrm{ON}}_{\mathrm{Page}} = (t_{\mathrm{w}} + t_{\mathrm{r}})P^{\mathrm{ON}}_{\mathrm{NoData}} + (t_{\mathrm{PDCCH}} + t_{\mathrm{PDSCH}})P^{\mathrm{ON}}_{\mathrm{Data}}, \tag{3.1}$$

where $P^{\mathrm{ON}}_{\mathrm{NoData}}$ and $P^{\mathrm{ON}}_{\mathrm{Data}}$ denote the ON time power consumption of the UE without active data and with active data respectively. The warm-up and resynchronization phases are considered to be non-active data phases since the UE is not running intricate control/data decoding processes like layer demapping, de-precoding. Viterbi/turbo decoding, etc. Therefore, the power consumption in these phases is $P^{\mathrm{ON}}_{\mathrm{NoData}}$.

When there is no page for the UE, the ON time (see Figure 3.5) is determined by $t^{\mathrm{ON}}_{\mathrm{NoPage}} = t_{\mathrm{w}} + t_{\mathrm{r}} + t_{\mathrm{PDCCH}}$ and the corresponding energy consumed is given by

$$E^{\mathrm{ON}}_{\mathrm{NoPage}} = (t_{\mathrm{w}} + t_{\mathrm{r}})P^{\mathrm{ON}}_{\mathrm{NoData}} + t_{\mathrm{PDCCH}}P^{\mathrm{ON}}_{\mathrm{Data}}\ . \tag{3.2}$$

The sleep time can be obtained by subtracting the ON time from the total length of the UE DRX cycle (denoted by $t_{\mathrm{DRX}}$). For the UE using the legacy synchronization

signal detection, $t_{\mathrm{r}} = t_{\mathrm{PSS}}$, which is the time consumed for the legacy synchronization signal detection. For the UE using our ePSS for resynchronization, $t_{\mathrm{r}} = t_{\mathrm{ePSS}}$, which corresponds to the ePSS detection time. Also, when the ePSS is used as the QSI and when there is no page for the UE, the decoded ePSS pattern itself suggests that there is no valid page and the UE does not decode the PDCCH. In this case, the ON time will be $t^{\mathrm{ON}}_{\mathrm{NoPage}} = t_{\mathrm{w}} + t_{\mathrm{ePSS}}$. Using $p$ to denote the probability that the UE is paged, the total energy consumed by the UE can be calculated as

$$\begin{aligned} E_{\mathrm{tot}} = {} & p \cdot (E^{\mathrm{ON}}_{\mathrm{Page}} + (t_{\mathrm{DRX}} - t^{\mathrm{ON}}_{\mathrm{Page}})P_{\mathrm{S}}) \\ & + (1-p) \cdot (E^{\mathrm{ON}}_{\mathrm{NoPage}} + (t_{\mathrm{DRX}} - t^{\mathrm{ON}}_{\mathrm{NoPage}})P_{\mathrm{S}}), \end{aligned} \tag{3.3}$$

where $P_{\mathrm{S}}$ denotes the power consumed by the UE in deep sleep state.

For the Rx power consumption, we used $P^{\mathrm{ON}}_{\mathrm{Data}} = 500$ mW, $P^{\mathrm{ON}}_{\mathrm{NoData}} = 250$ mW and $P_{\mathrm{S}} = 0.0185$ mW [84, 118]. The UE warm-up time $t_{\mathrm{w}}$ was assumed to be 1 ms and the paging rate $p = 0.1$. We used $t_{\mathrm{PSS}} = 420$ ms for the legacy synchronization signal detection, $t_{\mathrm{ePSS}} = 30$ ms for the ePSS using multiple PSS and $t_{\mathrm{ePSS}} = 20$ ms for the ePSS using longer ZC sequences corresponding to the accumulation time required for 90% detection (see Figure 3.6). The energy efficiency gain indicates the ratio of the energy consumed by the UE receiver using the legacy synchronization signal detection for resynchronization to the energy consumed by the UE receiver using our ePSS for resynchronization. Table 3.2 summarizes the energy efficiency gain of the UE using our ePSS solutions for different values of the DRX cycle length $t_{\mathrm{DRX}}$. We examined two scenarios - a) Short paging decode time assuming $t_{\mathrm{PDCCH}} = t_{\mathrm{PDSCH}} = 10$ ms corresponding to the upper bound of the energy efficiency gains in Table 3.2 and b) Long paging decode time using $t_{\mathrm{PDCCH}} = t_{\mathrm{PDSCH}} = 40$ ms corresponding to the lower bound of the energy efficiency gains in Table 3.2. The cases we examined include the

Table 3.2: Rx energy efficiency gain for LC devices in DRX mode using ePSS.

| DRX Length $t_{\text{DRX}}$ | ePSS using multiple PSS | | ePSS using longer ZC | |
|---|---|---|---|---|
| | Not as QSI | As QSI | Not as QSI | As QSI |
| 2.56 s | 4.3 - 8.3 | 10.8 - 12.6 | 4.7 - 10.6 | 13.7 - 17.6 |
| 5.12 s | 4.3 - 8.3 | 10.8 - 12.5 | 4.7 - 10.2 | 13.6 - 17.5 |
| 10.24 s | 4.3 - 8.3 | 10.7 - 12.4 | 4.6 - 10.1 | 13.5 - 17.2 |
| 327.68 s | 3.7 - 6.0 | 7.5 - 7.9 | 4.0 - 6.9 | 8.7 - 9.5 |
| 2621.44 s | 2.2 - 2.6 | 2.8 - 2.9 | 2.3 - 2.7 | 2.9 - 3.0 |

maximum length of the DRX cycle supported in the current LTE/LTE-A standards (2.56 s) and the maximum extended DRX cycle length (2621.44 s).

In the following, we choose the DRX cycle length of 10.24 s to illustrate the interpretation of the energy efficiency gains in Table 3.2. In this case, the UE adopting DRX with our ePSS using multiple PSS mechanism for resynchronization is 4.3 times (denoted by 4.3x) more energy efficient than the UE using DRX with the legacy synchronization signal detection mechanism for resynchronization owing to faster timing reacquisition using the ePSS. Also, the gain obtained from the ePSS using longer ZC sequences is higher compared to the ePSS constructed using multiple PSS (4.7x as opposed to 4.3x), since the ePSS using longer ZC sequences requires a lesser time for reacquisition.

Moreover, the energy efficiency improves further when the ePSS is used as the QSI. For example, in the case of the 10.24 s DRX cycle, using our ePSS as QSI mechanisms are 10.7x (for the ePSS using multiple PSS) and 13.5x (for the ePSS using longer ZC sequences) more energy efficient than the legacy mechanism respectively. This demonstrates a significant increase compared to the corresponding gains obtained when the ePSS is not used as the QSI (4.3x and 4.6x respectively). This is because the LC device does not decode the PDCCH when the ePSS pattern indicates that

there is no page (which happens 90% of the time since $p = 0.1$) unlike the non-QSI cases where the UE has to decode the PDCCH regardless of whether it is paged or not, thereby simplifying the operation of checking for a page when our ePSS as QSI mechanism is used.

A common trend observed with the different ePSS solutions is that the energy efficiency gain decreases with the increase in length of the DRX cycle. This is because the reduction in energy consumption is directly proportional to the fraction of the time the UE is ON during the DRX cycle. Since the ON time of the UE depends on the SNR and not on $t_{\mathrm{DRX}}$, this ratio decreases with increase in $t_{\mathrm{DRX}}$ for a fixed SNR. However, even for the maximum DRX cycle length of 2621.44 s, the energy efficiency gain obtained is between 2.2x and 2.7x when ePSS is not used as QSI, which is considerable and improves further (between 2.8x and 3.0x) when ePSS is used as QSI. Also, for longer DRX cycle lengths, the legacy UE may have to reacquire the SFN before attempting to decode the paging control information (as discussed later in Section 3.4.5), while the UE using our ePSS solutions (as QSI) is informed about an upcoming page during the timing resynchronization phase itself and need not decode the SFN when there is no page. The energy efficiency gain computation does not account for the ON time of the UE for SFN decoding. Therefore, the energy efficiency gains obtained using our ePSS as QSI solutions (columns 2 and 4 of Table 3.2) for longer DRX cycles serve as a loose lower bound for the actual gains.

### 3.4.3 Battery Lifetime Improvement

Having established that the ePSS mechanisms result in higher energy efficiency, we now estimate the improvement in the battery lifetime of the device when our different ePSS solutions are used. The UE consumes its battery for both transmission and

Table 3.3: Battery lifetime gain for LC devices using ePSS with $t_{\mathrm{DRX}} = 10.24$ s and $t_{\mathrm{DRX}} = 2621.44$ s.

| Tx:Rx energy consumption share | ePSS using multiple PSS | | ePSS using longer ZC | |
|---|---|---|---|---|
| | Not as QSI | As QSI | Not as QSI | As QSI |
| | $t_{\mathrm{DRX}} = 10.24$ s | | | |
| 70:30 | 1.30 - 1.36 | 1.37 - 1.38 | 1.31 - 1.37 | 1.38 - 1.39 |
| 50:50 | 1.62 - 1.78 | 1.83 - 1.85 | 1.64 -1.82 | 1.86 - 1.89 |
| 30:70 | 2.16 - 2.60 | 2.74 - 2.81 | 2.21 - 2.71 | 2.84 - 2.94 |
| | $t_{\mathrm{DRX}} = 2621.44$ s | | | |
| 70:30 | 1.20 - 1.23 | 1.23 - 1.24 | 1.20 - 1.23 | 1.24 - 1.25 |
| 50:50 | 1.38 - 1.44 | 1.47 - 1.49 | 1.39 - 1.46 | 1.49 - 1.50 |
| 30:70 | 1.62 - 1.76 | 1.82 - 1.85 | 1.65 - 1.79 | 1.85 - 1.88 |

reception. The battery consumption share between UE's transmission and reception varies depending on the UE's application. For example, a device used for location tracking has to transmit the data more frequently than that used for smart meter data reporting. In both these applications require the device to periodically listen to the network to remain connected. The battery consumption share for transmission is higher for the UE used for location tracking, since it transmits data more frequently. However, for the UE used for smart meter data reporting, the battery consumption share is dominated by periodic reception. Hence, the battery consumption share between UE's transmission and reception is dictated by the duration of transmission and reception. Alternatively, if these durations are equal, one module can consume more energy than the other. For instance, a model where the device transmission may consume 2 times more energy than device reception is commonly used. In the following, we analyze the improvement in battery life for three different scenarios based on ratio of the UE battery consumption for transmission to that of the reception - a) 70:30 (Tx > Rx), b) 50:50 (Tx = Rx) and c) 30:70 (Tx < Rx).

Since our ePSS mechanisms are adopted by the UEs in the downlink, the energy

efficiency gains obtained using our solutions is applicable to the UE reception. The battery lifetime gain is calculated as

$$\beta = \frac{1}{s_{\mathrm{Tx}} + \frac{s_{\mathrm{Rx}}}{\eta}} \tag{3.4}$$

where $s_{\mathrm{Tx}}$ and $s_{\mathrm{Rx}}$ indicate the UE battery consumption share for transmission and reception respectively, and $\eta$ is the gain obtained by the use of our different ePSS solutions (given in Table 3.2). For example, in the first scenario $s_{\mathrm{Tx}} = 0.7$, $s_{\mathrm{Rx}} = 0.3$ and $\eta = 12.4$ for $t_{\mathrm{DRX}} = 10.24$ s and ePSS using longer ZC sequences (as QSI).

Table 3.3 gives the battery lifetime gain ($\beta$) for our different ePSS solutions with $t_{\mathrm{DRX}} = 10.24$ s and $t_{\mathrm{DRX}} = 2261.44$ s in the aforementioned scenarios. In the first scenario, a conventional battery lasting for 10 years can potentially last $10\beta = 10 \times 1.38 = 13.8$ years for $t_{\mathrm{DRX}} = 10.24$ s and $10 \times 1.24 = 12.4$ years for $t_{\mathrm{DRX}} = 2621.44$ s, when our ePSS using longer ZC sequences (as QSI) solution is adopted. This is a substantial improvement considering that only 30% of the battery was being used for UE reception. The battery lifetime gain increases as the battery consumption share for UE reception increases. For instance, with our ePSS using longer ZC sequences (as QSI) solution in the second and third scenarios, the battery lifetime increases to 18.6 years and 28.4 years respectively for $t_{\mathrm{DRX}} = 10.24$ s and to 14.9 years and 18.5 years respectively for $t_{\mathrm{DRX}} = 2261.44$ s, which is highly significant. The lowest energy efficiency gain is obtained when our ePSS using multiple PSS (not as QSI) solution is used. Even in this case the lifetime of a conventional battery lasting 10 years is extended to 13.0 years, 16.2 years and 21.6 years for the three scenarios for $t_{\mathrm{DRX}} = 10.24$ s and to 12.0 years, 13.8 years and 16.2 years respectively for $t_{\mathrm{DRX}} = 2261.44$ s, which is considerable. Similar to Section 3.4.2, the battery lifetime extension for ePSS as QSI solutions for longer DRX cycles serve as a loose lower

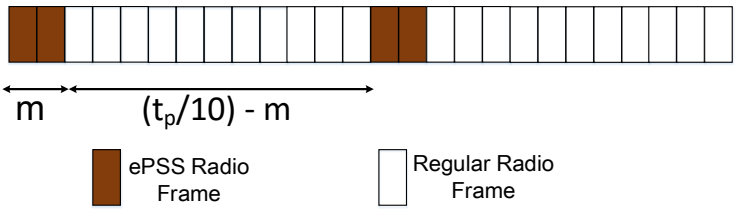


(a) Frame structure with ePSS transmission

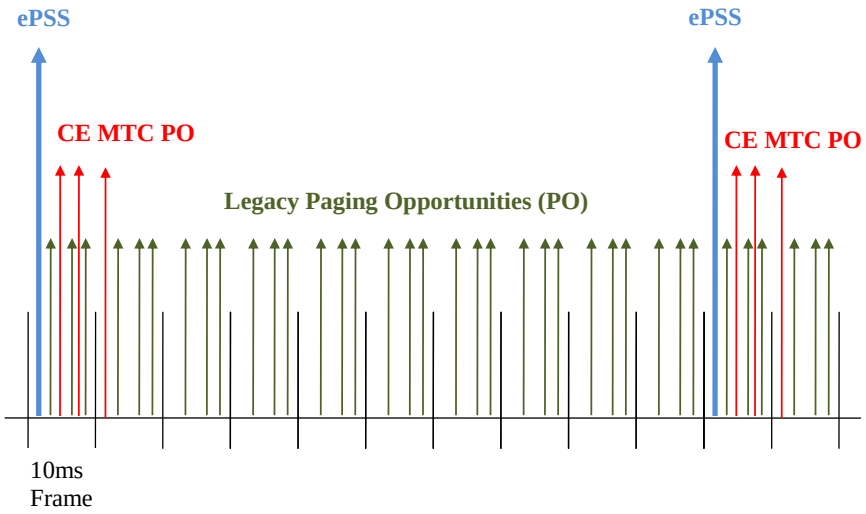


(b) ePSS and PO Allocation

Figure 3.7: Frame Structure and PO Allocation for LC devices using ePSS.

bound since the SFN decoding gain is not included in the computation.

### 3.4.4 Analysis of ePSS Transmission Overhead

The periodicity of the ePSS transmission determines the overhead on the network. If the ePSS is scheduled on every radio frame like the PSS, it will consume a lot of network resources. From our simulation results (see Figure 3.6), we note that $m$ ePSS frames are required for the desired accuracy of timing detection, where $m = 3$ for ePSS using PSS and $m = 2$ for ePSS using longer ZC sequences. If the periodicity

Table 3.4: Network resource overhead due to the ePSS transmission.

| eNB Bandwidth | $t_{\mathrm{p}} = 100$ ms | $t_{\mathrm{p}} = 360$ ms |
|---|---|---|
| 1.4 MHz (6 PRB pairs) | [4% 6%] | [1.11% 1.67%] |
| 5 MHz (25 PRB pairs) | [0.96% 1.44%] | [0.26% 0.4%] |
| 10 MHz (50 PRB pairs) | [0.48% 0.72%] | [0.13% 0.2%] |
| 20 MHz (100 PRB pairs) | [0.24% 0.36%] | [0.06% 0.1%] |

of ePSS is $t_{\mathrm{p}}$ ms, the transmission consists $m$ ePSS radio frames followed by $(\frac{t_{\mathrm{p}}}{10} - m)$ legacy radio frames as shown in Figure 3.7a.

The ePSS is mostly used by the LC devices. Therefore, to minimize the resource consumption, we propose to group the POs of such UEs close to the ePSS. This solution is illustrated in Figure 3.7b. For a given interval of time, the number of LC devices might a small subset of the total number of UEs. Assuming that 10% of the UEs are LC devices, the ePSS only needs to be sent every $t_{\mathrm{p}} = 100$ ms. Also, the P-RNTI for the LC devices can be sent on the enhanced PDCCH (ePDCCH) [117], which uses the subcarriers in the PDSCH space. The POs for the legacy UEs will be distributed and they will be paged via the regular PDCCH (PDCCH). This way the PDCCH capacity is not altered.

Moreover, when the ePSS is not transmitted every radio frame, a single ePSS will be used to resynchronize UEs that have their PO subframes greater than 10 ms from the ePSS subframe. Therefore, the UE can save power by going back to sleep after successfully detecting the ePSS and wake up again just before its PO. However, we have to ensure that the UE does not lose the symbol timing (UE clock does not drift by more than 5% of the symbol time, which is 3.6 $\mu$s) during its sleep time. For example, for a UE using a crystal with 10 ppm accuracy, the clock drift is within 5% of a symbol if the sleep time is less than 360 ms. Therefore, the maximum value of $t_{\mathrm{p}}$ is 360 ms for a 10 ppm accurate UE clock.

The ePSS consumes 6 PRB pairs $\times$ 2 subframes = 12 PRB pairs every 10 ms (refer

Figure 3.4a). As seen from Figure 3.6, the time taken to decode ePSS can be 20 ms (= 24 PRB pairs for ePSS using longer ZC sequences) or 30 ms (= 36 PRB pairs for ePSS using multiple PSS). The overhead on the eNB due to the resource allocation for the ePSS with periodicity $t_{\mathrm{p}} = 100$ ms and $t_{\mathrm{p}} = 360$ ms is summarized in Table 3.4. The numbers in each row of the second and third columns of Table 3.4 correspond to the network load considering ePSS decode time of 20 ms and 30 ms respectively. The eNB deployments usually have a bandwidth of 5 MHz or more and the network overhead due to the ePSS for such eNBs is less than 1.5% for both $t_{\mathrm{p}} = 100$ ms and $t_{\mathrm{p}} = 360$ ms. Moreover, the overhead of ePSS transmission is restricted to the idle mode. The regular data transmission occurs after the UE transitions from the idle mode to the connected mode, where the resource allocation uses the default LTE/LTE-A frame structure, without the ePSS. Therefore, the ePSS does not affect the regular data transmission.

### 3.4.5 Discussion

In summary, our ePSS solutions reduced the energy consumption when compared to the legacy solutions due to the following reasons.

- The ePSS consists of an increased density of synchronization signals, i.e., ePSS packs more synchronization signals in less amount of transmission time, thereby reducing the time taken by the UE to reacquire the symbol timing.

- The ePSS has an additional attribute of being able to indicate whether there is an impending page for the UE or not, thereby helping UEs to return to sleep mode quickly when there is no page and save energy. But the legacy UE follows the procedure of decoding the P-RNTI on the PDCCH regardless of whether it is paged or not, which is complex and energy consuming.

- The ePSS with best performance uses longer length ZC sequences, which possess better signal detection properties, thereby improving the reacquisition time and reducing power consumption.

Moreover, the legacy UE may have to reacquire the SFN so that it attempts to decode the paging information on the correct frame/subframe, depending on the accuracy of its clock and the length of the DRX cycle. This is because the UE will lose its frame timing when its clock drifts by more than half a frame ($= \frac{10\text{ms}}{2} = 5$ ms). For example, an LC UE with 10 ppm accurate clock [116] will lose its frame timing if it sleeps for more than $\frac{5\text{ms}}{(10 \cdot 10^{-6})} = 500$ s. When the DRX cycle length is than 500 s, the clock drift results in a symbol timing offset, but the UE remains in the same radio frame. However when the DRX cycle is longer than 500 s, both the frame timing and the symbol timing are lost and the UE has to reacquire the SFN.

The SFN field in LTE/LTE-A consists of 10 bits and is incremented by one every 10 ms (= frame length) [58, 59]. Hence the maximum time length that can be indicated by the SFN field is $2^{10} \times 10^{-3} = 10.24$ s. In order to support extended DRX cycles, the on-going standardization activities in LTE/LTE-A have included a new field called the Hyper - System Frame Number (H-SFN) which incremented by one every 10.24 s [56]. Currently, the number of H-SFN bits is set to 8. Consequently, the maximum time length that can be indicated with the combination of H-SFN and the legacy SFN is $(2^8 - 1) \times 10.24 + 10.24 = 2621.44$ s, which corresponds to the maximum extended DRX cycle length.

The UE has to decode the H-SFN and the SFN if it sleeps so long that the frame timing is lost, and then attempt the paging decode on the correct paging frame/subframe. Owing to the low operating SNR, H-SFN/SFN decoding can take multiple repetitions, increase the ON time and the energy consumption of the UE.

Also, the legacy UE needs to perform this decoding even when there is no page because it can know about the validity of the page only when it decodes the paging control information (which is post H-SFN/SFN decoding). But, when our ePSS as QSI solutions are used, the UE is informed about the validity of the page during the timing resynchronization phase itself and H-SFN/SFN decoding would not be necessary when there is no page. The savings obtained from not decoding the H-SFN/SFN when there is no page has not been included in our calculations for the energy efficiency gain and battery lifetime extension. Therefore, our results for this case serve as a loose lower bound and the actual gains that can be obtained using our solutions can be higher when the DRX cycle length is longer (>500 s for an LC UE with 10 ppm accurate clock).

Furthermore, our ideas can be extended to other OFDM based systems where the conventional methods of CP correlation and reference signal detection take a long time to converge at very low SNR. For example, in WLAN, two new, closely spaced, robust preamble sequences can be assigned to each UE, one indicating a "Page" and the other indicating "No Page". This mapping of paging indication to resynchronization sequences, combined with shrewd resource allocation would result in an energy efficient operation of the MTC UEs.

## 3.5 Conclusion

In this chapter, we considered the DRX mechanism in LTE/LTE-A for the low-cost, low-complexity MTC UEs requiring coverage enhancement (denoted by LC devices). We explored the sensitivity of the paging decode operation to the timing offset in greater detail by improving the timing resolution from being symbol accurate (see Chapter 2) to being sample accurate. Firstly, we showed that the paging decode

operation, which is a critical part of the DRX mechanism, is very sensitive to timing offset. Secondly, we explored the conventional timing acquisition algorithms - CP autocorrelation and the legacy synchronization signal detection and demonstrated they take around 600 ms and 380 ms respectively for reacquiring the symbol timing within tolerable limits. This leads to increased ON time of the UE and hence results in increased energy consumption. To mitigate this problem, we introduced the ePSS within the LTE/LTE-A standardization framework and proposed a novel DRX mechanism which uses our ePSS for faster timing resynchronization and reduced energy consumption. We described two simple methods to design the ePSS signal - by using multiple PSS sequences and by using ZC sequences and indicated that our ePSS design requires less than 1.5% network resource overhead for eNB bandwidths of 5 MHz or more.

Further, adopting the DRX with QSI mechanism described in Chapter 2, we proposed the use of the ePSS as QSI to further improve the energy efficiency of the LC devices. We illustrated that the modified DRX mechanism for the LC devices using our ePSS solutions results in 1.2 to 1.8 times improvement in their battery lifetime. Similar to the QSI mechanisms from Chapter 2, the specific ePSS solutions are suitable for UE categories of CAT-M1, CAT-0 and above. But the core idea behind the ePSS, i.e., faster resynchronization and quick return to sleep, is applicable to all the UE categories. For example, a synchronization signal block occupying 12 subcarriers $\times$ 11 symbols is being considered as the PSS in NB-IoT standardization, in order to reduce the time consumed for initial acquisition. Also, studies in 5G NR are accounting for the energy consumption due to timing acquisition and considering novel designs for the synchronization and paging channels.

# Chapter 4

# Low SNR Uplink CFO Estimation

## 4.1 Introduction

In Chapter 2 and Chapter 3, we described energy efficient mechanisms for the LTE/LTE-A MTC UEs in the downlink. In this chapter, we explore the MTC mechanisms for energy efficient uplink transmission using LTE/LTE-A, under low network coverage. Although the UEs belonging to CAT-M1 or higher categories could operate on a bandwidth of at least 1.4 MHz, the LTE/LTE-A MTC standardization activities in the uplink focused on single PRB transmission (occupying 180 kHz bandwidth), in order to address massive access by supporting higher number of MTC UEs per time interval. The introduction of the NB-IoT framework (described in Section 1.2.2) to the LTE/LTE-A standards provided the further motivation to device efficient UE data transmission mechanisms over a narrow bandwidth. Therefore, single PRB transmission became a common theme across different UE categories, promoting the exchange of ideas between standardization activities for CAT-0, CAT-M1 and NB-IoT UEs. Moreover, developing mechanisms to reduce the number of retransmissions and hence improve the uplink energy efficiency became a common challenge to be addressed in all UE categories.

It is well known that improved channel estimation, including accurate timing and frequency offset estimation is beneficial for data decoding. As mentioned in Section 1.2.2, the eNB adopts the timing advance indication mechanism to ensure

that all UE transmissions are time synchronized. Minor deviations in timing offset are estimated accurately using the CP autocorrelation [63, 64]. These procedures ensure that the residual timing offset is within the CP length [58] and do not impact the system performance. However, the tracking the Carrier Frequency Offset (CFO) of each UE using CP autocorrelation is complex (as described in detail in Section 4.3.1), necessitating novel mechanism for CFO estimation at the eNB.

Prior works for uplink CFO estimation consider normalized CFO (actual CFO value divided by the subcarrier spacing) and describe algorithms to estimate and compensate for the normalized CFO [63, 64, 107, 119]. However, there is a small portion of the CFO remaining in the system after compensation depending on the accuracy of estimation, called the residual CFO. Although it is desirable to minimize this residual CFO, the benefits from this reduction are minimal at high operating SNR, since the channel estimation algorithms at the base-station can effectively handle a small residual CFO. In LTE/LTE-A, the subcarrier spacing is 15 kHz [58]. For instance, when the actual residual CFO in the system is 100 Hz, the normalized residual CFO value is 0.067, which is negligible at high SNR. However, a significant number of MTC UEs are expected to operate in low coverage areas, where the operating SNR is as low as -15 dB [43, 44] and as we demonstrate, the residual CFO adversely impacts the performance of such UEs.

In this chapter, we first demonstrate that further reduction in residual CFO is highly beneficial for MTC UEs in low coverage, since it reduces the number of data retransmissions, which in turn reduces the ON time of the UEs and hence increases the energy efficiency. We propose ML based algorithms for robust CFO estimation in low coverage, using - a) repeated data transmission, b) pilot transmission and c) both repeated data and pilot transmission. We also derive the Cramér-Rao lower bound

for these estimators. Next, we provide an insight into the NB-IoT large transport block transmission scheme, which is a novel, simple and effective mechanism being considered by the 3GPP for energy efficient MTC and illustrate how the energy efficiency obtained from this scheme can be further enhanced by the use of our robust CFO estimation techniques. Lastly, we propose a variation of the LTE/LTE-A frame structure incorporating additional pilot signals during the initial MTC transmissions, which assists in faster CFO estimation at the eNB with minimal overhead.

The rest of the chapter is organized as follows. In Section 4.2, we analyze the effect of CFO on the energy efficiency of the NB-IoT MTC UEs. In Section 4.3, we describe the conventional techniques used for CFO estimation and in Section 4.4, we introduce our ML based CFO estimation technique for LTE/LTE-A MTC. Using simulations, we compare the performance of our CFO estimation technique with the conventional techniques in Section 4.5, followed by a detailed analysis of the energy efficiency of MTC UEs using CFO estimation and compensation for the current transmission scheme and the newly proposed large transport block transmission mechanism. In Section 4.6, we propose a new MTC transmission technique with increased pilot density, which uses our ML based CFO estimation technique for faster CFO estimation in low coverage. The conclusions are presented in Section 4.7.

## 4.2 Effect of CFO Estimation for NB-IoT Uplink

As described in Section 1.2.2, the NB-IoT mechanism in LTE/LTE-A refers to the transmission and reception of signals on a bandwidth corresponding to one PRB (180 kHz). This is helpful to low data rate MTC UEs, where the transmission happens in small bursts of data followed by long idle periods. It would be ideal for the UE to complete its data transmission with minimal number of retransmissions, switch

to idle mode and save power. The number of retransmissions depends on the SNR, the channel conditions and the timing/frequency estimation accuracy at the eNB decoding the UE data. While the CP autocorrelation and timing advance mechanisms enable the eNB to accurately track the timing offset [63, 64], tracking the CFO using CP autocorrelation would be quite complex (explained later in Section 4.3.1).

In this section, we demonstrate our model for energy consumption analysis and determine the effect of residual CFO on the energy consumption using numerical calculations.

### 4.2.1 Energy Consumption Model

In order to calculate the energy consumption, we adopt a simple model,

$$E = P_{\mathrm{ON}} t_{\mathrm{ON}} + P_{\mathrm{OFF}} t_{\mathrm{OFF}} \tag{4.1}$$

where $P_{\mathrm{ON}}$ and $P_{\mathrm{OFF}}$ denote the power consumed by the UE during its active (ON) period and sleep (OFF) period respectively. The durations ON and OFF periods are represented by $t_{\mathrm{ON}}$ and $t_{\mathrm{OFF}}$ respectively. The total time length is $t_{\mathrm{Total}} = (t_{\mathrm{ON}} + t_{\mathrm{OFF}})$ and we define $v = \frac{P_{\mathrm{OFF}}}{P_{\mathrm{ON}}}$, where $v \ll 1$ since the sleep time power consumption is much lower than the active time power consumption. Then, the energy consumption is calculated as

$$E = P_{\mathrm{ON}}(t_{\mathrm{ON}} + v(t_{\mathrm{Total}} - t_{\mathrm{ON}})). \tag{4.2}$$

### 4.2.2 Numerical Results

To illustrate the impact of CFO on the UE energy consumption, we consider a scenario with no residual timing offset, since it can be estimated with a sufficient degree of

accuracy using the CP and determine the number of repetitions required for an MTC UE for different values of the residual CFO. The presence of CFO leads to Inter Carrier Interference (ICI), which affects the performance. However, the amount of ICI is small, since we analyze the effects of residual CFO. Multi-user Interference (MUI) is not considered because the LTE/LTE-A standards ensure that subcarriers are not shared between different users for a given subframe [58]. We first analyze the performance for CFO = 100 Hz, which is the value used for MTC performance evaluation by the 3GPP [43] and then for lower values of CFO, corresponding to 50 Hz, 25 Hz and 10 Hz. Among the different CFO values, we use CFO = 10 Hz to model the scenario where the frequency offset is negligible, based on simulations which indicated that the number of repetitions required by the UE did not change significantly for $0 \leq \text{CFO} \leq 10$ Hz.

The simulations are performed using the LTE toolbox in MATLAB. In order to analyze the low coverage scenario, the 3GPP recommends the evaluation of performance for 18 dB additional coverage [43], which corresponds to our operating SNR of -15.5 dB. For the channel model, we use the EPA model with a Doppler spread of 1 Hz, which is advocated by the 3GPP for MTC UEs with limited mobility [43]. We use a single PRB pair transmission scheme (12 subcarriers $\times$ 1 subframe) with the MCS index chosen to be 5 (corresponding to QPSK modulation and a code rate of 0.4385 [57]), consistent with the 3GPP recommendation for NB-IoT. We use TBS = 72 bits, which is the maximum transport block size for MCS = 5 [57]. Other simulation parameters are summarized in Table 4.1.

Table 4.2 gives the number of subframes required by the eNB to decode the transport block and the effective data rate for different values of the residual CFO. It is evident that a transport block with lower CFO requires fewer repetitions than the

Table 4.1: Simulation parameters

| Parameter | Value |
|---|---|
| No. data symbols per subframe | 12 subcarriers × 12 symbols |
| No. of DMRS symbols per subframe | 12 subcarriers × 2 symbols |
| No. UE antennas | 1 |
| No. eNB antennas | 2 |
| eNB bandwidth | 10 MHz |
| eNB sampling rate | 15.36 MHz |
| Channel Model | EPA 1 Hz |
| SNR | -15.5 dB |
| BLER | 0.1 |

Table 4.2: Energy efficiency vs. CFO for TBS = 72 bits

| CFO | $N_{\text{SF}}$ | $R_{\text{eff}}$ (kbps) | Energy Efficiency Gain | | |
|---|---|---|---|---|---|
| | | | D = 10% | D = 1% | D = 0.1% |
| 100 | 110 | 0.44 | - | - | - |
| 50 | 100 | 0.48 | 8.6% | 8.5% | 7.5% |
| 25 | 92 | 0.52 | 15.5% | 15.3% | 13.5% |
| 10 | 80 | 0.60 | 25.9% | 25.5% | 22.5% |

one with higher CFO, thereby increasing the effective data rate. This suggests that a lower residual CFO at the eNB helps the MTC UE to complete its transmission quickly, turn off its radio and save power.

We obtain the energy consumed by the UE for the different CFO values using Eq. (4.2) with $t_{\text{ON}} = \frac{1}{R_{\text{eff}}}$ s per bit, where $R_{\text{eff}}$ is the effective data rate given by 1.1. We consider the energy consumed by the UE for CFO = 100 Hz, denoted by $E_{\text{orig}}$, as our reference and compute to the energy efficiency gain as $\left(1 - \frac{E_{\text{new}}}{E_{\text{orig}}}\right)$, where $E_{\text{new}}$ is the energy consumption of the UE corresponding to the lower CFO values.

Table 4.2 summarizes the energy efficiency results when $t_{\text{Total}}$ is an integer multiple of $t_{\text{orig}}$, which is the time taken for successful decoding with CFO = 100 Hz. That is, $t_{\text{Total}} = qt_{\text{orig}}$ and $q = 10, 100, 1000$, which correspond to duty-cycles (D) of 10%, 1% and 0.1% respectively, $P_{\text{ON}} = 100$ mW (corresponding to the 20 dBm transmission

power of MTC UEs [43, 48]) and $P_{\text{OFF}} = 0.015$ mW (based on the sleep time power consumption indicated in [84,118]). The reason to choose these duty-cycles is that for each case, the inactive duration of the UE is much greater than the active duration, which suitably models the infrequent data transmission and low-data rate mode of operation of MTC UEs.

A common trend that we note in these results is that the energy efficiency gain decreases with decrease in D. This is intuitive because the reduction in energy consumption is obtained by reducing the ON time of the UE and smaller values of D results in lower ON time. We observe that the energy efficiency gain increases with a decrease in residual CFO. The reduction of residual CFO from 100 Hz to 10 Hz results in 22.5% reduction in energy consumption even for a low duty cycle of 0.1%, which is significant. Therefore, a robust CFO estimation mechanism at the eNB, which works accurately at low operating SNRs and helps in reducing the energy consumption of the MTC UE is desirable.

## 4.3 Conventional CFO Estimation Techniques

Having established the need for accurate CFO estimation to enable high energy efficiency of IoT communication, we now discuss the CFO estimation techniques that are currently used in the uplink. In particular, we consider two techniques - a) CP autocorrelation [63, 64] and b) symbol repetition demonstrated in [107, 119] and the references within, which are widely used for fractional frequency offset estimation in the uplink. We illustrate why these techniques cannot be used by MTC UEs using LTE/LTE-A in low coverage.

In literature, fractional frequency offset is often represented and estimated in terms of the normalized CFO, i.e., the actual CFO value divided by the subcarrier

spacing ($\Delta F$). The subcarrier spacing is related to the sampling rate ($N_{\mathrm{s}}$) and the FFT size ($N_{\mathrm{FFT}}$) such that $N_{\mathrm{s}} = N_{\mathrm{FFT}}\Delta F$. However, we choose to represent the frequency offset using actual CFO instead of normalized CFO because our work considers the estimation of residual CFO, which is typically represented in terms of the actual value.

### 4.3.1 CP Autocorrelation

In OFDM based systems, the CFO is estimated from the phase of the autocorrelation of the CP as

$$\hat{\epsilon} = \frac{N_{\mathrm{s}}}{2\pi N_{\mathrm{FFT}}} \left( \mathrm{angle} \left( \sum_{n=0}^{N_{\mathrm{CP}}-1} y(n + N_{\mathrm{FFT}}) y^*(n) \right) \right) \tag{4.3}$$

where $y(n)$ is the $n^{\mathrm{th}}$ sample of the received time-domain signal at the eNB, $N_{\mathrm{s}}$ is the sampling rate, $N_{\mathrm{FFT}}$ is the FFT size used at the eNB and $N_{\mathrm{CP}}$ is the CP length [63, 64]. From Eq. (4.3), we see that $\hat{\epsilon}$ is the product of the normalized CFO with the subcarrier spacing (indicated by the $\frac{N_{\mathrm{s}}}{N_{\mathrm{FFT}}}$ scaling factor), which denotes the actual CFO in the system.

In multiple access systems like Orthogonal Frequency Division Multiple Access (OFDMA) and Single Carrier - Frequency Division Multiple Access (SC-FDMA), when multiple UEs occupy the spectrum, the time-domain symbol and the CP contains components from all the UEs . Assuming that UEs have perfect timing synchronization, the CP portion of the received signal at the eNB will consist of the sum of the CPs of all the UEs. Each UE might have a different CFO. Therefore, detection of each UE's CFO requires the separation of its time-domain symbol and its CP from the multiplexed received signal.

In order to get the per-UE time-domain symbol, the eNB first takes an FFT of the

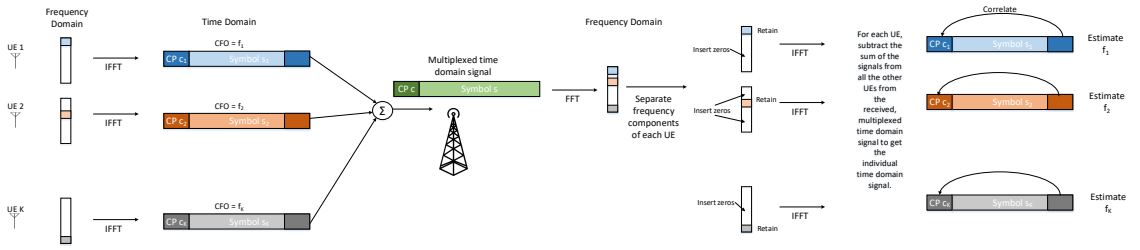


Figure 4.1: Illustration of CFO estimation using CP autocorrelation.

multiplexed time-domain signal, retains the subcarriers of the UE of interest, sets the remaining subcarriers to zero and takes an Inverse Fast Fourier Transform (IFFT). This procedure is illustrated in Figure 4.1. Moreover, in the case of MTC UEs in low coverage, multiple repetitions of the time domain symbol and CP are required for successful detection, which further increases the complexity. For example, an eNB with a bandwidth of 10 MHz has 50 PRBs available for user data and uses a 1024-point FFT. For MTC UEs using single PRB transmission and a large number of MTC devices present in the network, we can potentially have 50 UEs served at each instant. To separate the time-domain symbol and CP of each UE, the eNB requires 1 FFT and 50 IFFTs. Since the FFT/IFFT is $O(N \log_2(N))$ complex operations, this requires $51 \times 1024 \times 10 \approx 5.2 \times 10^5$ complex operations, which is computationally intensive. Furthermore, if the UEs are in low coverage and assuming that 14 symbols (1 subframe) are required for successful frequency offset detection, the number of complex operations increases to $7.3 \times 10^6$. Therefore, CP autocorrelation is not an ideal candidate for CFO estimation in the case of MTC UEs.

### 4.3.2 Symbol Repetition

Besides the CP autocorrelation method, CFO estimation can be done by correlating repetitions of data or pilot signals and measuring the correlation phase angle (see

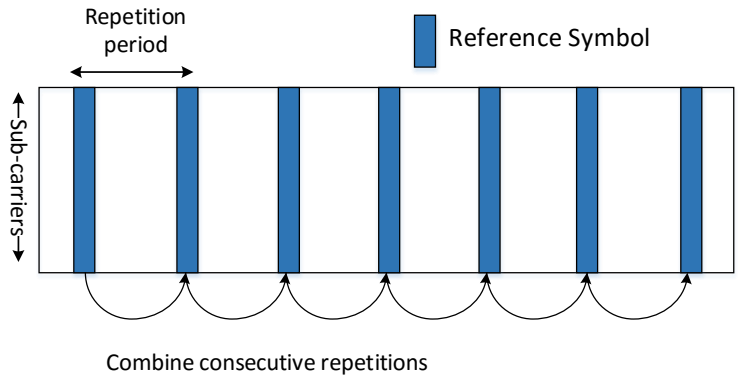


Figure 4.2: Illustration of CFO estimation using symbol repetition.

Figure 4.2) [107, 119]. However, the repetitions should be close enough in time, so that the phase angle does not roll-over. If a UE has to measure a CFO ranging from -$f_0$ Hz to $f_0$ Hz, the maximum amount of time between two repetitions is given by $T_{\text{rep}} = \frac{1}{2f_0}$. For example, we require $T_{\text{rep}} = 1$ ms, if the UE has to measure a CFO ranging from -500 Hz to 500 Hz. In other words, the detectable CFO range decreases as $T_{\text{rep}}$ increases. The estimation method is formulated as

$$\hat{\epsilon} = \frac{N_{\text{s}}}{2\pi N_{\text{g}}} \left( \text{angle} \left( \sum_{n=1}^{N-1} Y_n \cdot Y_{n-1}^{*} \right) \right) \tag{4.4}$$

where $Y$ is the frequency-domain received symbol spanning over $N_{\text{sc}}$ subcarriers, "$\cdot$" denotes element-wise multiplication, $n$ indicates the repetition index, $N$ is the number of repetitions required to successfully detect the CFO, $N_{\text{s}}$ is the sampling rate and $N_{\text{g}}$ is the number of samples between the consecutive symbol repetitions in terms of the FFT size, $N_{\text{FFT}}$. For example, when the repetitions occur every 2 symbols, $N_{\text{g}} = 2N_{\text{FFT}}$. Again, $\hat{\epsilon}$ in Eq. (4.4) also denotes the actual CFO in the system.

Unlike the method of CP autocorrelation, this technique can be scaled to accommodate multiple UEs. This is because the method uses frequency-domain symbols

and the signals of different UEs can be easily separated and the CFO of each UE can be separately calculated in the frequency domain. However, in LTE/LTE-A, the DMRS symbols repeat every 10 ms and the range of the CFO that could be detected with this is only from -50 Hz to 50 Hz, which is smaller than the residual CFO range (-100 Hz to 100 Hz) in the system. Therefore, the DMRS symbols cannot be directly used for correlation phase angle based CFO estimation. In the following, we propose our mechanisms for CFO estimation for MTC UEs using LTE/LTE-A in low coverage.

## 4.4 ML Based CFO estimation

In this section, we describe the design of our ML based CFO estimation algorithm for two cases - 1) using repeated RV transmission and 2) using the DMRS. Our ML based CFO estimation method is an extension of the method discussed in [119], which was designed for consecutive symbol repetition. We modify the algorithm in [119] so as to fit the LTE/LTE-A frame structure and operate on subframe repetitions (in case 1) and reference signal repetition (in case 2).

Let $d$ denote the transmitted signal of length $K$ samples. The CFO of the UE is denoted by $\epsilon$. Since the CFO is a phase-ramp in time-domain, the signal with CFO is given by

$$s(k) = d(k)\mathrm{e}^{\left(\frac{j2\pi\epsilon k}{N_\mathrm{s}}\right)} = d(k)\mathrm{e}^{jk\theta} \tag{4.5}$$

where $N_\mathrm{s}$ is the sampling rate, $k = 0, 1, 2, \cdots, K-1$ and

$$\theta = \frac{2\pi\epsilon}{N_\mathrm{s}}. \tag{4.6}$$

Using Eq. (4.5), the LTE/LTE-A transport block transmission in time-domain can

be expressed as

$$s_n(k) = d_n(k)\mathrm{e}^{j(k+nK)\theta} \tag{4.7}$$

where $k = 0, 1, 2, \cdots, K-1$, $n = 0, 1, 2, \cdots N_{\mathrm{SF}} - 1$ and $N_{\mathrm{SF}}$ is the number of subframes required for the successful decoding of the transport block.

The current LTE/LTE-A standards support 4 RVs of the UE data block to be transmitted. The UE transmits one RV per subframe and the RV index is cycled in the order $[0, 2, 3, 1]$, i.e., $d_0 = d_4 = d_8 = \cdots = r_0, d_1 = d_5 = d_9 = \cdots = r_2$ and so on, where $r_q$ denotes the RV being transmitted with the RV index $q = 0, 2, 3, 1$. This means that the RV is repeated every 4 subframes and considering that each subframe is 1 ms, the range of CFO detection is -125 Hz to 125 Hz.

In the ongoing LTE MTC standardization, RV repetition is being proposed for MTC UEs. When the UE uses RV repetition, it respects the standard RV cycling order, but can transmit $N$ repetitions of the same RV index before switching to the next index, i.e, $d_0 = d_1 = d_2 = \cdots = d_{N-1} = r_0, d_N = d_{N+1} = d_{N+2} = \cdots = d_{2N-1} = r_2$ and so on. For example, if $N = 3$, the UE transmits [0,0,0,2,2,2,3,3,3,1,1,1,0,0,0,...]. Therefore, for the MTC UEs, the CFO detection range is -500 Hz to 500 Hz.

### 4.4.1 ML Based CFO Estimation Using Repeated Data

In the following, we derive an ML based technique, which uses the RV repetitions to estimate the CFO. We define a new signal $x$, which consists of $N$ repetitions of the same RV (denoted by $r$). Then, we have

$$x_n(k) = r(k)\mathrm{e}^{j(k+nLK)\theta} \tag{4.8}$$

where $k = 0, 1, 2, \cdots, K-1$, $n = 0, 1, \cdots N-1$, $L = 4$ for legacy UEs (since the same RV is repeated every 4 subframes) and $L = 1$ for MTC UEs (since the repetitions are consecutive).

Let $R$ denote the DFT of $r(k)\mathrm{e}^{jk\theta}$. Then, in frequency domain, each RV reception at the eNB can be expressed as

$$Y_n = H_n \cdot R\mathrm{e}^{jnLK\theta} + W_n \tag{4.9}$$

where $H_n$ is the channel vector ($n = 0, 1, \cdots, N-1$), $W_n$ is the noise vector and $H_n \cdot R$ denotes the element-wise multiplication between $H_n$ and $R$.

We assume that the channel remains the same for $N$ subframes, which holds in the case of pedestrian channels. Therefore, $H_n = H, \forall n$. In order to estimate the CFO, we have to estimate $\theta$ from Eq. (4.9). Since we have no information about the data and the channel, the unbiased estimate for the vector $H \cdot R$ is given by

$$\hat{C} = \frac{1}{N} \sum_{n=0}^{N-1} Y_n \mathrm{e}^{-jnLK\theta}. \tag{4.10}$$

Substituting Eq. (4.10) to Eq. (4.9), the ML estimator for the phase angle $\theta$, denoted by $\hat{\theta}$ and the corresponding CFO estimate ($\hat{\epsilon}$) are given by

$$\hat{\theta} = \min_{\theta} \sum_{k=0}^{N-1} \|Y_k - \hat{C} \cdot \mathrm{e}^{jkLK\theta}\|^2, \tag{4.11}$$

$$\hat{\epsilon} = \frac{\hat{\theta} N_\mathrm{s}}{2\pi LK}. \tag{4.12}$$

The value of $\hat{\theta}$ is obtained by searching over the different values of $\theta$ between 0 and $2\pi$ in discrete steps. The step size is set according to the required resolution of

the CFO estimate. If the CFO resolution is $f_{\mathrm{r}}$ Hz, then the step size for the search is $\frac{2\pi LKf_{\mathrm{r}}}{N_{\mathrm{s}}}$. The complexity of the search increases when a finer resolution is required for the CFO estimate.

#### 4.4.1.1 Cramér-Rao Lower Bound

The performance of an estimator is typically analyzed using the Mean Squared Error (MSE), which is lower bounded by the Cramér-Rao bound. For our ML based CFO estimator using repeated data, Cramér-Rao bound is given by

$$CRB_{\epsilon} = \frac{3N_s^2\Psi^{-1}}{4\pi^2L^2K^2MN(N-1)(4N-3)} \tag{4.13}$$

where $\Psi$ is the SNR and $M$ is the number of DFT samples used for estimating the CFO. The procedure to derive $CRB(\epsilon)$ is illustrated in the Appendix A.

### 4.4.2 ML Based CFO Estimation Using the DMRS

The generic structure of our ML based CFO estimation technique enables us to extend its applicability to the periodic repetitions of DMRS signals in LTE/LTE-A. A DMRS symbol is transmitted every half subframe. For DMRS transmission, Eq. (4.9) changes to

$$\tilde{Y}_{nm} = G_{nm} \cdot P_{nm}\mathrm{e}^{\frac{j(2n+m)K\theta}{2}} + \tilde{W}_{nm} \tag{4.14}$$

where $P_{nm}$ are the known DMRS sequences, $G_{nm}$ and $\tilde{W}_{nm}$ are the channel and the noise vectors with $n = 0, 1, \cdots, N-1$, denoting the subframe index and $m = 0, 1$ indicates whether the DMRS is transmitted on the first half ($m = 0$) or the second half of the subframe ($m = 1$). Therefore, $L$ is set to $\frac{1}{2}$ for DMRS transmission and

there is no difference between the legacy and MTC UEs. This is because the DMRS is transmitted in the same manner for legacy as well as MTC UEs with a periodicity of half subframe (0.5 ms).

Now, we derive the ML based CFO estimator using the DMRS. Similar to the ML estimator for repeated data, we assume that the channel does not vary over the $N$ subframes of interest. Hence, $G_{nm} = G, \forall n, m$. Then, the channel estimate is given by

$$\hat{G} = \frac{1}{2N} \sum_{n=0}^{N-1} \sum_{m=0}^{1} \tilde{Y}_{nm} \cdot P_{nm}^{*} \mathrm{e}^{\frac{-j(2n+m)K\theta}{2}}, \tag{4.15}$$

and the ML estimator for $\theta$ is given by

$$\hat{\theta} = \min_{\theta} \sum_{k=0}^{N-1} \sum_{l=0}^{1} \|\tilde{Y}_{kl} - \hat{G} \cdot P_{kl} \mathrm{e}^{\frac{j(2k+l)K\theta}{2}}\|^2, \tag{4.16}$$

and the corresponding CFO estimate can be calculated using Eq. (4.12). The range of CFO values that can be detected using this mechanism is between -1 kHz to 1 kHz, since the DMRS periodicity is 0.5 ms. The Cramér-Rao bound for this case can also be obtained from Eq. (4.13), using $L = \frac{1}{2}$, $M$ equal to the length of the DMRS sequence and $2N$ repetitions instead of $N$.

### 4.4.3 Modified Conventional CFO Estimation Scheme for DMRS

Although DMRS symbols are transmitted every 0.5 ms in LTE/LTE-A, the duration of repetition between identical DMRS symbols is 10 ms. If the conventional correlation phase angle method is used on these DMRS repetitions, it results in a reduced CFO detection range of -50 Hz to 50 Hz (refer to Section 4.3.2). Here, we suggest a modification to the conventional method so that it can make use of all the DMRS

transmissions to estimate the CFO within the desired range.

We multiply each received DMRS symbol ($\tilde{Y}_{nm}$ in Eq. (4.14) by the conjugate of the reference DMRS symbol ($P_{nm}$) and obtain the CFO estimate by using the phase angle of the correlation of consecutive DMRS symbols. To illustrate this mechanism, we denote $Z_{2n+m} = \tilde{Y}_{nm} \cdot P^*_{nm}, \forall n, m$, where $n = 0, 1, \cdots N-1$ and $m = 0, 1$. Then, the CFO estimate is given by

$$\hat{\epsilon}_{\text{conv}} = \frac{N_{\text{s}}}{\pi K} \left( \text{angle} \left( \sum_{l=1}^{2N-1} Z_l \cdot Z^*_{l-1} \right) \right). \tag{4.17}$$

The range of CFO detection using such a modified mechanism is between -1 kHz and 1 kHz, similar to the ML based CFO estimation technique using DMRS.

### 4.4.4 ML Based CFO Estimation Using Repeated Data with DMRS Compensation

Our ML based CFO estimation using repeated data proposed in Section 4.4.1 uses only the data symbols for estimating the CFO. The DMRS symbols are not used because they are not the same between consecutive subframes. Here, we extend this method such that it also incorporates the DMRS symbols. This is done by multiplying each received DMRS symbol by the conjugate of the reference DMRS symbol (similar to the method in Section 4.4.3). Then, all the DMRS symbols will be a vector of ones, multiplied by the channel co-efficient and the CFO in that symbol plus the noise at the receiver. This will give us two additional symbols per subframe for ML estimation of CFO.

## 4.5 Simulation Results

In this section, we first present the simulation results for our ML based CFO estimation algorithms and compare their performance with the conventional CFO estimation techniques. Then, we introduce the large transport block transmission mechanism for MTC, where the UE transmits transport blocks whose size is larger than that supported in the current LTE/LTE-A standards. We illustrate that this mechanism improves the effective data rate of the UE and reduces the energy consumption. We also show that the energy efficiency of the MTC UE is further enhanced when this mechanism is used in conjunction with our ML based CFO estimation technique.

### 4.5.1 Performance of CFO Estimation Techniques

In order to analyze the performance of our ML based CFO estimation and the conventional CFO estimation techniques, we consider three cases - a) using data symbols only, b) using the entire subframe with DMRS compensation and c) using DMRS symbols only. In the first case, we have 12 symbols available per subframe for CFO estimation and in the second case, the DMRS symbols of the received subframe are multiplied with their conjugates, so that the entire subframe can be used for CFO estimation. In the third case, we use only the 2 DMRS symbols in each subframe to estimate the CFO. The residual CFO in the system is 100 Hz and the CFO estimation error is measured as the absolute value of the difference between the actual CFO and the estimated CFO values. We evaluate the performance based on the number of subframes required to estimate the CFO within 10 Hz accuracy, denoted by $N_{\text{CFO}}$.

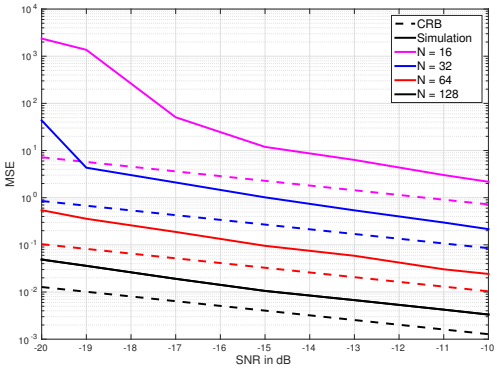


(a) Using data symbols only

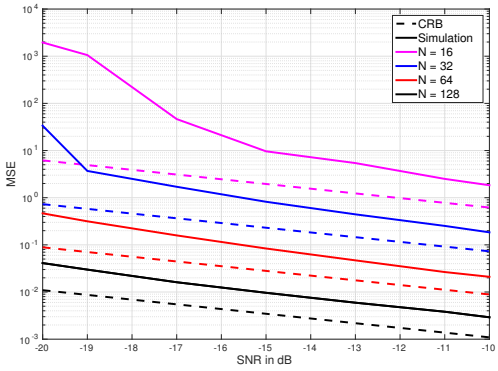


(b) Using the entire subframe

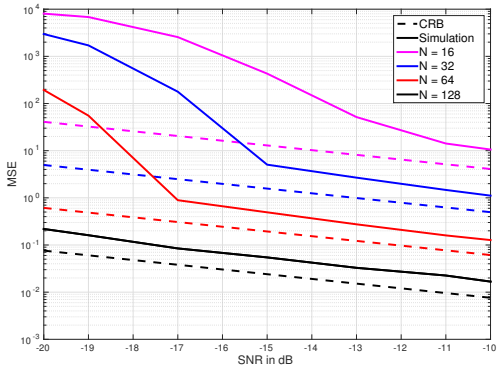


(c) Using DMRS symbols only

Figure 4.3: MSE vs. SNR and Cramér-Rao bound for ML based CFO estimation in AWGN.

### 4.5.2 MSE and Cramér-Rao Bound for the Gaussian Channel

First, we determine the MSE of our ML based CFO estimator for the three cases in an AWGN channel and compare the MSE with the Cramér-Rao bound given in Eq. (4.13). The eNB bandwidth is chosen to be 10 MHz and the corresponding sampling rate $N_s = 15.36$ MHz. Therefore, each subframe (1 ms) contains $K = 1$ ms $\times$ 15.36 MHz = 15360 samples. In the first two cases, the data is repeated in every subframe (MTC RV transmission case), which corresponds to $L = 1$. For the first

case, the number of DFT samples used for CFO estimation, we have $M = 12$ symbols $\times$ 12 subcarriers = 144 and for the second case, $M = 14$ symbols $\times$ 12 subcarriers = 168. The MSE and Cramér-Rao bound for these two cases are shown in Figure 4.3a and Figure 4.3b respectively. In the third case, we have DMRS symbols spanning 12 subcarriers transmitted every half-subframe, corresponding to $L = \frac{1}{2}$, $M = 12$ and a total of $2N$ DMRS transmissions. The results for this case are shown in Figure 4.3c.

The SNR considered for this analysis is between -20 dB and -10 dB, corresponding to the operating scenarios for MTC UEs in low network coverage. It can be observed that with increasing SNR, the MSE of our ML based CFO estimator gets closer to the Cramér-Rao bound for all the three cases. Also, the performance of the first two cases is better than that of the third case due to larger value of $M$ in these cases. Moreover, the MSE is measured for actual CFO values, which means that an estimation error of 10 Hz corresponds to MSE = 100. Therefore, for an AWGN channel with SNR of -15.5 dB (corresponding to 18 dB coverage enhancement) and the desired CFO estimation accuracy of 10 Hz, $N_{\text{CFO}} = 16$ for the first two cases and $N_{\text{CFO}} = 32$ for the third case.

### 4.5.3 Results for the EPA Channel

Now, we analyze the performance of our ML based CFO estimation techniques for the EPA channel. Owing to the very low operating SNR, achieving the desired accuracy of estimation with 100% probability may take a very large number of repetitions for fading channels. In such cases, it is necessary to evaluate the performance based on a probabilistic measure, i.e., achieving the desired accuracy of estimation with high probability. Therefore, we define the performance metric as the number of subframes ($N$) required to achieve CFO estimation error $\leq$ 10 Hz with 95% probability

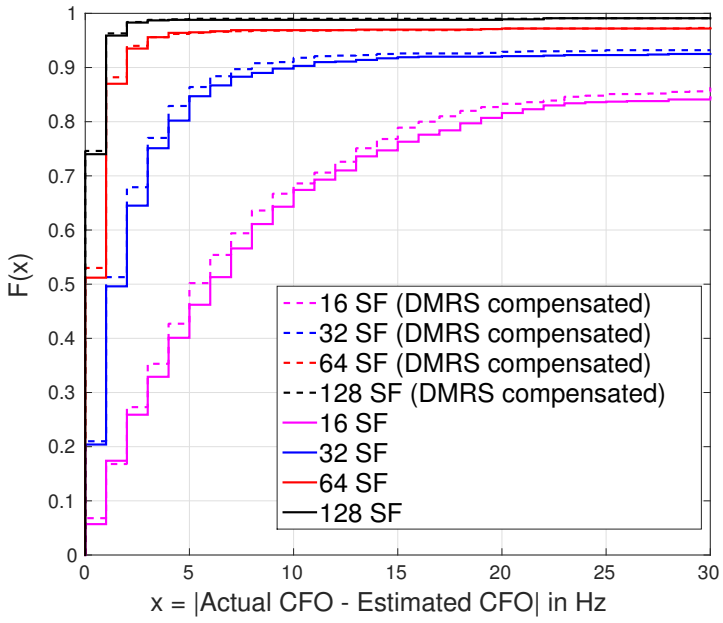


(a) Using ML estimation

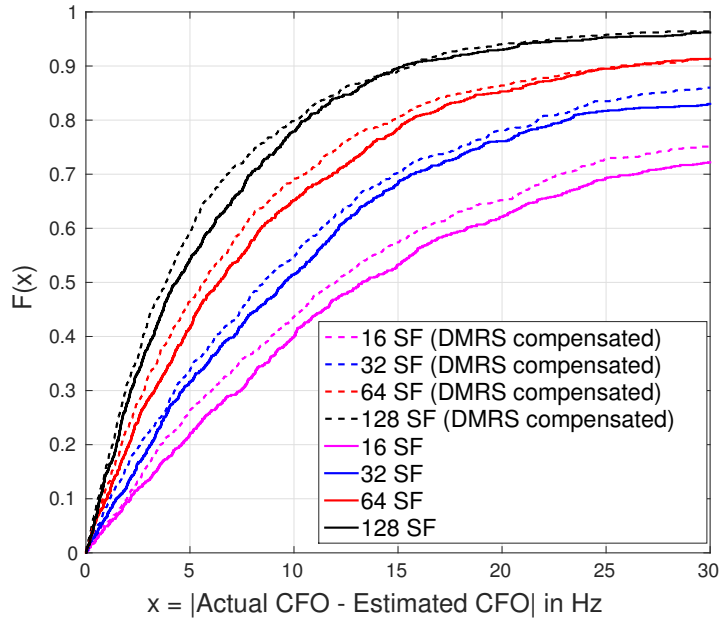


(b) Using angle-based estimation

Figure 4.4: CDF of the estimated CFO error using RV repetitions for legacy LTE/LTE-A uplink.

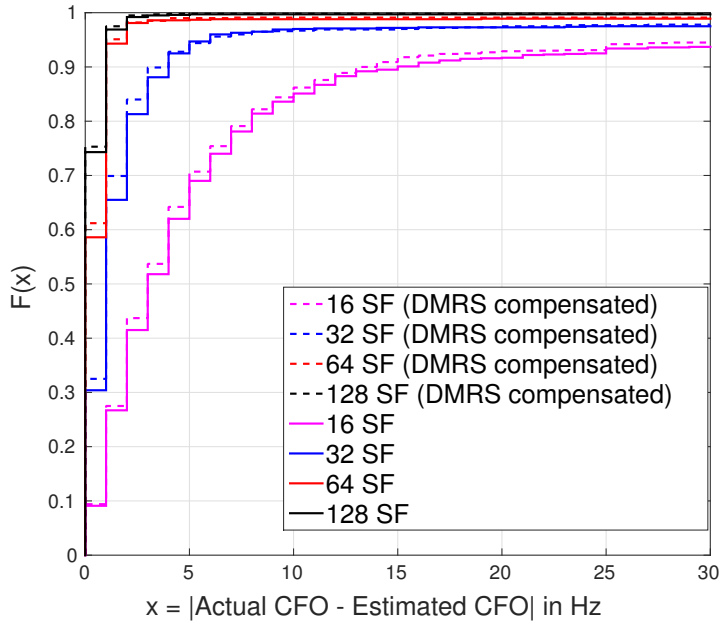


(a) Using ML estimation

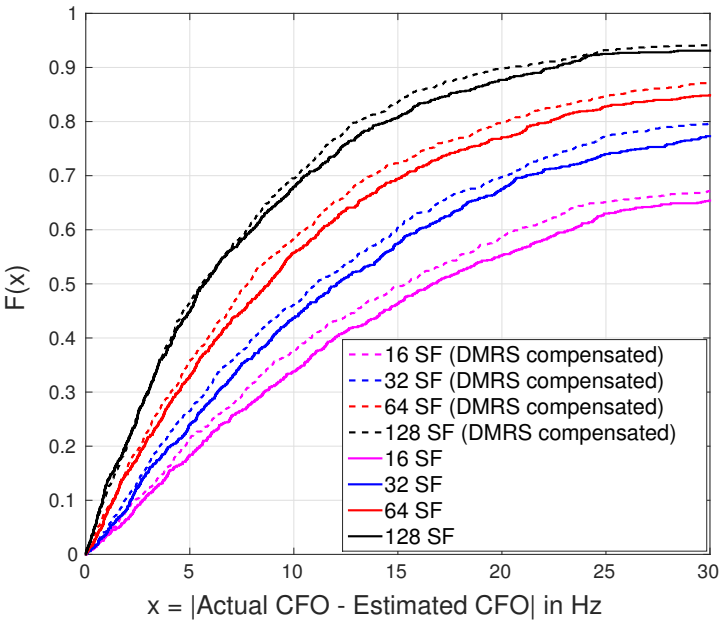


(b) Using angle-based estimation

Figure 4.5: CDF of the estimated CFO error using RV repetitions for MTC LTE/LTE-A uplink.

and present the results in terms of the Cumulative Distribution Function (CDF) of the CFO estimation error for different values of $N$. A similar approach is adopted by different companies in the 3GPP when they provide the performance results for downlink synchronization, where the number of repetitions of the synchronization signal required to achieve 90% detection probability is used as the performance metric [43, 44].

For the first two cases, we compare the results obtained by our method with the CFO estimation scheme using the conventional angle-based scheme (see Eq. (4.4)). For the DMRS only case, we compare the results from the ML based estimation scheme with that obtained from the modified angle-based scheme (see Eq. (4.17)). The simulation settings are summarized in Table 4.1.

Figure 4.4a and Figure 4.4b indicate the performance of our ML based CFO estimation algorithm and the conventional angle-based CFO estimation algorithm respectively, for the legacy RV transmission scheme (RV pattern: $0, 2, 3, 1, 0, 2, 3, 1, \cdots$) in LTE/LTE-A uplink. We observe that our ML estimation based method requires at least $N_{\text{CFO}} = 64$ for $\geq 95\%$ probability of successful CFO estimation, while for $N_{\text{CFO}} = 16$, this probability reduces to 68%. Therefore, for the desired CFO performance (95% success rate with 10 Hz accuracy), the eNB has to buffer 64 subframes. The conventional angle-based method has only 80% success rate in CFO estimation even when $N_{\text{CFO}} = 128$. In both the cases, using the entire subframe with DMRS compensation performs marginally better than using only the data symbols because we have 14 symbols instead of 12 available for CFO estimation.

Figure 4.5a and Figure 4.5b depict the performance the two CFO estimation algorithms for the MTC RV transmission scheme (RV pattern with $N$ RV-0s, followed by $N$ RV-2s and so on) in LTE/LTE-A uplink. Since the CFO is estimated using $N$

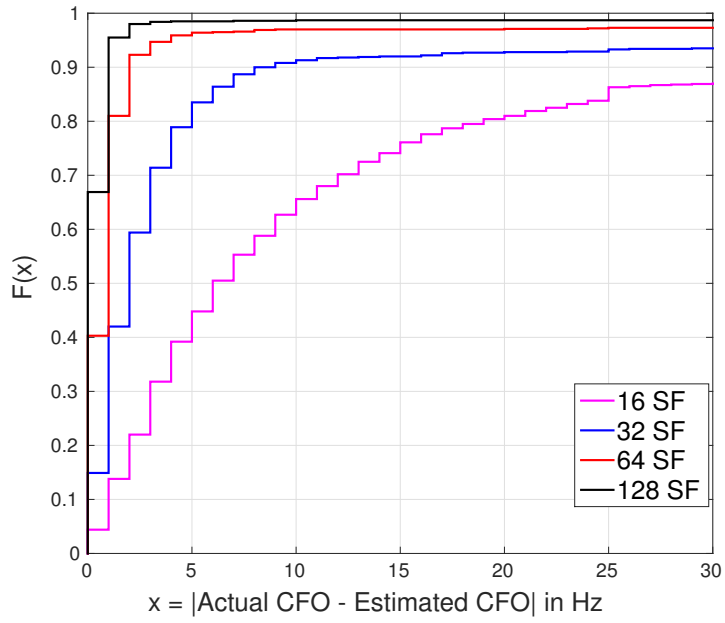


(a) Using ML estimation

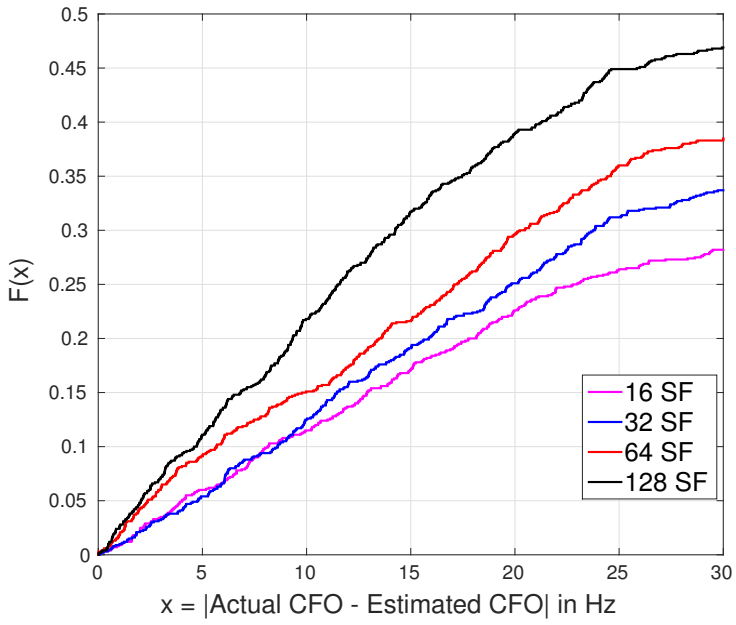


(b) Using modified angle-based estimation

Figure 4.6: CDF of the estimated CFO error using DMRS only for both legacy and MTC LTE/LTE-A uplink.

subframes, $N_{\text{CFO}} = N$. In this case, we observe that our ML estimation based method with $N_{\text{CFO}} = 16$ has around 82% probability of successful CFO estimation, which is a significant improvement when compared to the legacy case, while for $N_{\text{CFO}} = 32$, we see that the probability of successful estimation increases to 95%. This means that the eNB has to buffer 32 subframes for CFO estimation and correction, which is half the size required for the legacy RV transmission scheme. The conventional angle-based method has similar performance to that of the legacy case. Therefore, for both the legacy and MTC RV repetition schemes, the correlation phase angle method fails to achieve the same estimation accuracy as that of the ML based CFO estimator.

Figure 4.6a and Figure 4.6b show the CDF of the CFO estimation error using our ML estimation based method and the conventional angle-based method using only the DMRS signals. Also, there is no need to differentiate the legacy and MTC scenarios since the DMRS transmission mechanism remains the same for both the scenarios. We observe that the conventional method fails to provide an accurate CFO estimation even with averaging over 128 subframes because there are only 2 symbols available per subframe for CFO estimation. Also, our ML based CFO estimation technique using 2 DMRS symbols performs as well as the same technique for legacy RV scheme, requiring $N = 64$ subframes for estimating the CFO within 10 Hz with 95% probability. Using 2 DMRS symbols per subframe is as good as using 12 data symbols because the noise on the DMRS symbols is averaged $2N$ times, while that on data symbols is averaged $N$ times, resulting in better performance. Although this means that we use only one-seventh of the symbols for CFO estimation (2 DMRS symbols instead of 14 symbols in the legacy RV scheme), the eNB still needs to buffer the entire 64 subframes, since the CFO correction has to be applied on all the data

symbols.

To this end, we have shown that the reduction in residual CFO results in an increase in the energy efficiency of the MTC UE (see Table 4.2) and that our proposed ML based CFO estimation techniques provide a robust and an accurate mechanism to reduce the residual CFO in low coverage. Also, the number of subframes required by our technique for CFO detection is smaller than the total number of subframes required for successful data decoding (see Table 4.2), i.e., $N_{\mathrm{CFO}} < N_{\mathrm{SF}}$, ensuring the feasibility of implementation of our technique at the eNB. In the following, we go one step further and apply our improved methods to the so-called large transport block transmission mechanism for MTC UEs in LTE/LTE-A, to further enhance their energy efficiency.

### 4.5.4 NB-IoT Large Transport Block Transmission

In the current LTE/LTE-A standards, the maximum TBS is fixed based on the MCS and the number of PRBs allocated to the UE. With QPSK chosen to be the highest order of modulation for NB-IoT, the maximum TBS that can be transmitted corresponds to MCS = 9, which is 136 bits [57, 58]. The 3GPP standardization activities are considering a large transport block transmission mechanism, where the UE transits transport blocks whose size is larger than the current maximum size of 136 bits. Now, we briefly review the large transport block transmission mechanism and demonstrate the energy efficiency gains when our CFO estimation technique is applied to such a mechanism.

The large transport block transmission mechanism relies on the precedent that the effective data rate of the UE increases when larger sized blocks are transmitted, which means that the UE can complete its transmission quickly, go back to idle state

and save power. The effective data rate of the UE is given by Eq. (1.1). If we increase the TBS by a factor $\alpha$ in Eq. (1.1), then $N_{\mathrm{SF}}$ need not increase by the same amount. This is because the performance of the turbo decoder used for decoding the transport block does not vary linearly with respect to the code rate. In most of the cases, $N_{\mathrm{SF}}$ will scale by a factor less than $\alpha$, thereby increasing the effective data rate. However, the TBS cannot be increased arbitrarily and is limited by the code rate.

The transport block is appended with a 24-bit CRC [58, 59]. The code rate per subframe is calculated as

$$c_{\mathrm{orig}} = \frac{(\mathrm{TBS} + 24)}{(T_{\mathrm{sc}} \times n_{\mathrm{b}})} \tag{4.18}$$

where $T_{\mathrm{sc}}$ denotes the total number subcarriers available for transmitting the transport block and $n_{\mathrm{b}}$ is the number of bits per subcarrier. Since, MTC transmission is restricted to QPSK, $n_{\mathrm{b}} = 2$. Considering that the uplink transmission for a single antenna UE requires 2 symbols for DMRS transmission (see Figure 1.4), there are 12 symbols available for control and data transmission. Assuming that the UE uses a single PRB pair transmission (12 subcarriers per symbol) and does not transmit any control information when it is sending data, $T_{\mathrm{sc}} = 12 \times 12 = 144$.

Legacy LTE/LTE-A standards indicate that the transport block transmission should obey the condition of each RV being independently decodable [58]. Hence, the code rate must be chosen per RV. However, this condition is relaxed for low-complexity MTC UEs, since they are low data-rate devices and require multiple retransmissions of data in most of the cases. Therefore, we have a new metric called the effective code rate, which is a measure of the code rate over 4 RVs, given by $c_{\mathrm{eff}} = \frac{c_{\mathrm{orig}}}{4}$ and the data block can be decoded when all 4 RVs are received.

To illustrate this aspect, let us choose TBS = 324 bits. Noting that $T_{\mathrm{sc}} = 144$ and $n_{\mathrm{b}} = 2$, we get $c_{\mathrm{orig}} = 1.21 (> 1)$, which suggests that each RV transmission will not

Table 4.3: Number of repetitions vs. CFO

| TBS | $N_{100\text{Hz}}$ | $N_{10\text{Hz}}$ | $R_{100\text{Hz}}$ (kbps) | $R_{10\text{Hz}}$ in (kbps) |
|---|---|---|---|---|
| 72 | 110 | 80 | 0.44 | 0.60 |
| 144 | 200 | 144 | 0.60 | 0.83 |
| 224 | 304 | 216 | 0.66 | 0.93 |
| 328 | 376 | 256 | 0.81 | 1.19 |
| 424 | 448 | 304 | 0.89 | 1.32 |

be independently decodable for this TBS and it cannot be used in the legacy scheme. However, for the MTC scheme, the effective code rate $c_{\text{eff}} = 0.3(< 1)$, which suggests that the TBS is can be readily used.

### 4.5.5 Energy Efficiency Analysis

Now, we illustrate the reduction in energy consumption of MTC UEs obtained by the use of large transport block transmission and our ML based CFO estimation. We use the energy consumption model described in Section 4.2.1 to calculate the energy efficiency of the MTC UEs. The simulation parameters are listed in Table 4.1 and the power consumption values used are the same as in Section 4.2.2.

Table 4.3 gives the number of subframes required by the eNB to decode the transport block ($N_{100\text{Hz}}$ and $N_{10\text{Hz}}$) and the effective data rate for large transport block transmission ($R_{100\text{Hz}}$ and $R_{10\text{Hz}}$) with CFO = 100 Hz and CFO = 10 Hz, respectively. The former CFO value is the one currently used by the 3GPP for MTC performance evaluation and the latter models the negligible frequency offset scenario (refer Section 4.2.2). Similar to the performance of the regular sized transport block (TBS = 72 bits) in Section 4.2.2, we observe that the effective data of the UE increases with a decrease in the residual CFO value even for large transport blocks.

Table 4.4: Energy efficiency gain vs. TBS

| TBS | $\eta_1$ | | | $\eta_2$ with $p = 0.95$ | | |
|---|---|---|---|---|---|---|
| | D = 10% | D = 1% | D = 0.1% | D = 10% | D = 1% | D = 0.1% |
| 72 | - | - | - | 25.8% | 25.6% | 22.5% |
| 144 | 27.2% | 26.9% | 23.7% | 45.2% | 44.6% | 39.3% |
| 224 | 33.6% | 33.2% | 29.3% | 50.2% | 49.5% | 43.7% |
| 328 | 46.0% | 45.3% | 40.0% | 60.0% | 59.2% | 52.3% |
| 424 | 51.1% | 50.4% | 44.5% | 63.4% | 62.5% | 55.2% |

Table 4.5: Battery lifetime gain vs. TBS for transmitting 10 kilobytes

| TBS | $\beta_1$ | | | $\beta_2$ | | |
|---|---|---|---|---|---|---|
| | Tx:Rx Power consumption share | | | | | |
| | 70:30 | 50:50 | 30:70 | 70:30 | 50:50 | 30:70 |
| 72 | - | - | - | 1.19 - 1.22 | 1.13 - 1.15 | 1.07 - 1.08 |
| 144 | 1.2 - 1.24 | 1.13 - 1.16 | 1.08 - 1.09 | 1.38 - 1.46 | 1.24 - 1.29 | 1.13 - 1.16 |
| 224 | 1.26 - 1.31 | 1.17 - 1.2 | 1.1 - 1.11 | 1.44 - 1.54 | 1.28 - 1.33 | 1.15 - 1.18 |
| 328 | 1.39 - 1.47 | 1.25 - 1.30 | 1.14 - 1.16 | 1.58 - 1.72 | 1.35 - 1.43 | 1.19 - 1.22 |
| 424 | 1.45 - 1.56 | 1.29 - 1.34 | 1.15 - 1.18 | 1.63 - 1.8 | 1.38 - 1.46 | 1.2 - 1.23 |

#### 4.5.5.1 Large Transport Block Transmission Only

First, we calculate the energy efficiency obtained solely by the use of large transport block transmission, where the residual CFO is not compensated and remains at 100 Hz. Let $E_{\text{ltb}}$ denote the energy consumed in this scenario. $E_{\text{ltb}}$ is obtained by using $t_{\text{ON}} = t_{\text{ltb}} = \frac{1}{R_{100\text{Hz}}}$ s per bit in Eq. (4.2). The energy efficiency gain is calculated as

$$\eta_1 = \frac{E_{\text{orig}} - E_{\text{ltb}}}{E_{\text{orig}}} = 1 - \frac{t_{\text{ltb}} + v(t_{\text{Total}} - t_{\text{ltb}})}{t_{\text{orig}} + v(t_{\text{Total}} - t_{\text{orig}})} \tag{4.19}$$

#### 4.5.5.2 Large Transport Block Transmission with CFO Estimation

When our ML based CFO estimation techniques are used, the corresponding energy consumption, $E_{\text{cfo}}$ is obtained by using $t_{\text{ON}} = t_{\text{cfo}} = \frac{1}{R_{10\text{Hz}}}$ s per bit in Eq. (4.2). However, the CFO estimation is successful with probability $p$ owing to the low operating SNR and limited symbol buffer size available at the eNB. Therefore, the energy

consumption of the UE with CFO estimation is given by

$$E_{\text{final}} = pE_{\text{cfo}} + (1-p)E_{\text{orig}} \tag{4.20}$$

Then, the energy efficiency gain of the UE using CFO estimation is calculated as

$$\begin{aligned}\eta_2 &= \frac{E_{\text{orig}} - E_{\text{final}}}{E_{\text{orig}}} = p\left(1 - \frac{E_{\text{cfo}}}{E_{\text{orig}}}\right) \\ &= p\left(1 - \frac{t_{\text{cfo}} + v(t_{\text{Total}} - t_{\text{cfo}})}{t_{\text{orig}} + v(t_{\text{Total}} - t_{\text{orig}})}\right)\end{aligned} \tag{4.21}$$

We use the energy consumed by the UE for TBS = 72 bits and CFO = 100 Hz, $E_{\text{orig}}$, as our reference and evaluate the energy efficiency of different sized transport blocks transport blocks with CFO = 100 Hz and CFO = 10 Hz. Table 4.4 summarizes the energy efficiency results for three different duty-cycles (D), corresponding to 10%, 1% and 0.1% (refer Section 4.2.2).

We observe that solely the large transport block (without CFO estimation) results in 23.7% to 44.5% more energy efficiency than the current mode of operation with TBS = 72 bits even for a very low duty cycle of 0.1%. When our ML based CFO estimation techniques are used, the residual CFO is within 10 Hz with 95% probability ($p = 0.95$). With this, we obtain a further improved energy efficiency of 39.3% to 55.2% for larger TBS, indicating that robust CFO estimation at the eNB significantly reduces the energy consumption of the MTC UEs in low coverage.

Alternatively, the performance of our mechanisms can be analyzed using the battery lifetime gain metric (similar to that discussed in Chapter 3, Section 3.4.3). Since our solutions here are with respect to UE transmission, the battery lifetime gain is given by

$$\beta_i = \frac{1}{(1-\gamma_i)s_{\text{Tx}} + s_{\text{Rx}}} \tag{4.22}$$

where $i = 1$ for solely the large transport block transmission and $i = 2$ for the large transport block transmission with CFO estimation. The parameter $\gamma_i$ represents the energy efficiency gain calculated for the transmission of a data packet of size $d_\mathrm{s}$ bits. That is, $\gamma_1$ is obtained by calculating $\eta_1$ using $t_\mathrm{ltb} = \mathrm{ceil}\left(\frac{d_\mathrm{s}}{R_\mathrm{100Hz}}\right)$ and $\gamma_2$ is obtained by calculating $\eta_2$ using $t_\mathrm{cfo} = \mathrm{ceil}\left(\frac{d_\mathrm{s}}{R_\mathrm{10Hz}}\right)$. In both the cases, $t_\mathrm{orig} = \mathrm{ceil}\left(\frac{d_\mathrm{s}}{\hat{R}_\mathrm{100Hz}}\right)$, where $\hat{R}_\mathrm{100Hz}$ corresponds to $R_\mathrm{100Hz}$ value of the TBS used as reference.

Since $\gamma_i$ denotes the energy efficiency gain of the UE transmitter for the transmission of $d_\mathrm{s}$ bits, the transmission energy consumed is $(1 - \gamma_i)s_\mathrm{Tx}$. Table 4.5 provides the battery lifetime gains for different TBS values for $d_\mathrm{s} = 10$ kilobytes using TBS = 72 bits at CFO = 100 Hz as reference. For each entry, the lower value corresponds to D = 1% and the higher value corresponds to D = 10%.

The results are similar to those obtained for energy efficiency gain in Table 4.4. Smaller duty cycles have lower gains and CFO estimation improves the battery lifetime gain for the large transport block transmission. For example, with the largest TBS of 424 bits and Tx:Rx share of 50:50, we obtain a battery lifetime gain of 1.29 to 1.34, which means that a battery lasting for 10 years would now last for 12.9 to 13.4 years. With our robust CFO estimation and compensation, the battery would last for an improved lifetime of 13.8 to 14.6 years. Also, we obtain increased gains when the UE transmission has a higher power consumption share than reception, which is opposite to the results in Chapter 3 (see Table 3.3). However, this is expected because our mechanisms discussed here only reduce the transmitter energy consumption and do not modify the receiver energy consumption.

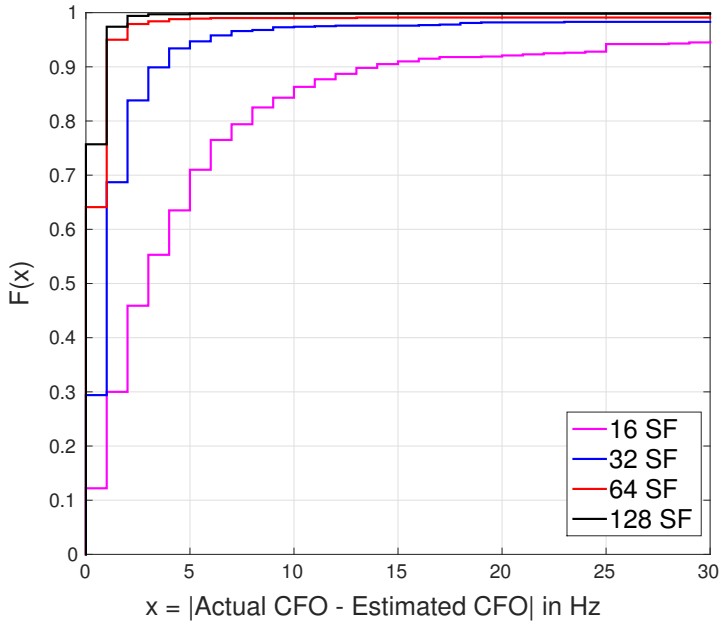


Figure 4.7: CDF of the estimated CFO error using ML estimation and 2x DMRS.

## 4.6 Discussion

The ML based CFO estimation scheme using RV repetition for MTC UEs (see Fig 4.5a), which demonstrated the best performance, suggests that the eNB requires 32 consecutive repetitions of the same RV for the desired CFO estimation performance. It would be beneficial to have an MTC transmission scheme, which not only assists in CFO estimation, but also removes the constraints on RV block transmission and repetition. In this section, we propose a new uplink transmission scheme with increased DMRS density, which achieves this objective. Also, we briefly discuss how our ML estimation based CFO estimation mechanisms can be used in non-LTE scenarios.

### 4.6.1 Increased DMRS Density Scheme in LTE/LTE-A Uplink

In the following, we propose a new transmission scheme for LTE/LTE-A uplink, where the DMRS density is doubled for $N$ initial subframes and evaluate the performance of our ML based CFO estimation technique using the DMRS technique. In the current LTE/LTE-A uplink, the DMRS sequences are transmitted on the fourth and the eleventh symbols of a subframe with normal CP (see Figure 1.4). For our proposed transmitted scheme, the MTC UEs double the DMRS density by transmitting new DMRS sequences on the third and the tenth symbols along with the legacy DMRS sequences for the initial $N$ subframes and then reverts back to the legacy scheme.

Figure 4.7 gives the performance our ML based CFO estimation scheme when the DMRS density is doubled. We observe that we can estimate the CFO within 10 Hz of the actual value with 95% probability when the accumulation time is 32 ms or more. The performance results are close to that of the ML based CFO estimation scheme using RV repetition for MTC UEs (see Fig 4.5a) and the doubled DMRS density scheme does not impose any restriction on the RV block being transmitted and the number of repetitions, as desired.

The only disadvantage of this scheme is that there is an overhead of 2 symbols for first $N$ subframes for each transmission. For example, with $N = 32$, we have an overhead of 64 symbols. With 14 symbols per subframe (1 subframe = 1 ms), the overhead time is less than 5 ms. Since, the transmission takes more than 100 subframes for any TBS, the overhead is less than 5% for all the cases. Moreover, the eNB can utilize the increased DMRS density for better channel estimation, which improves the overall performance of data decoding and further reduces the overhead. Alternatively, one could use the advantage of better channel estimation to transmit

data with a higher MCS, thereby increasing the throughput. Therefore, for the same number of buffered subframes, our increased DMRS density based estimation is more beneficial than estimation using repeated data.

### 4.6.2 Application of ML Based CFO Estimation to Non-LTE Scenarios

Hitherto, we designed and developed CFO estimation mechanisms specific to the LTE/LTE-A frame structure considering RV repetitions and DMRS transmissions. However, this technique can be readily extended to any communication mechanism incorporating periodic data and/or pilot repetitions. The ML based CFO estimation for such scenarios can be derived by choosing the appropriate values of $K$ and $L$ based on the length and the periodicity of the repeated data/pilot signals in Eq. (4.14) (similar to how we derived the DMRS based estimation as a special case).

## 4.7 Conclusion

In this chapter, we addressed the problem of improving the uplink energy efficiency of MTC devices adhering to the NB-IoT framework. We showed that the energy efficiency of the MTC UE increases if the eNB adopts CFO estimation mechanisms that reduce the residual CFO to negligible limits. We proposed an ML based CFO estimation mechanism that uses the data and pilot repetitions in LTE/LTE-A and illustrated that it significantly outperforms the legacy CFO estimation technique using the phase of the correlation between consecutive data repetitions. We demonstrated that incorporating our ML based CFO estimation technique at the eNB results 22.5%-55.2% reduction in energy consumption of the MTC UEs, when compared to

the case where the residual CFO is not compensated. We also proposed a variation of the LTE/LTE-A frame structure incorporating additional pilot signals during the initial MTC transmissions, which assists in faster CFO estimation at the eNB with minimal overhead.

Our ML based CFO estimation technique provides a robust mechanism to estimate the CFO in low coverage. Moreover, it is applicable to all categories of LTE MTC UEs and can also be easily adopted to other wireless communication standards. Recently, NB-IoT standardization decided not to adopt the increased DMRS density scheme, in order to maintain full compatibility with legacy UEs. However, the prospects of having such a scheme for 5G NR standardization is open for study.

# Chapter 5

# Conclusions and Directions for Future Work

The research work presented in this thesis focused on developing mechanisms to improve the current LTE/LTE-A standards to effectively support the IoT. Specifically, we suggested enhancements to the MTC framework in LTE/LTE-A addressing the energy efficiency of the UEs in normal coverage, as well as those requiring coverage enhancement. The solutions developed for normal coverage are applicable to the IoT scenarios of pet tracking or weather sensing in which the UEs have low-mobility and are located in regions where the network coverage is good. The mechanisms developed for extended coverage are suitable for the IoT applications of patient health monitoring or smart metering, where the IoT devices are located in interiors of buildings where the network coverage is low. Most importantly, our solutions are in line with the standardization activities for MTC in 3GPP LTE/LTE-A to facilitate IoT and have minimal influence on the legacy UEs.

In Chapter 2, we discussed the limitations of the DRX procedure, which is currently used by the LTE/LTE-A UEs in the downlink for saving power. We showed that the power savings obtained from the DRX mechanism depend on the duration for which the UE is awake, i.e., the ON time of the UE, which in turn depends on the procedure followed by the UE for decoding the paging information. We discussed that the paging operation was computationally intensive and was performed every

time the UE wakes up from the DRX cycle, regardless of whether it is paged or not. To simplify the paging decode procedure, we introduced the a modified DRX mechanism incorporating quick sleeping. Our Quick Sleeping Indication (QSI) would indicate whether the UE is receiving a valid page or not in the upcoming paging transmission. The UE would first decode the QSI and if it indicated an impending paging message, the UE would stay awake for decoding the page. However, if there is no valid page, the UE would immediately go back to sleep and save energy.

For the normal coverage case, we designed the quick sleeping mechanisms using the resources that were already being allocated by the base station, thereby avoiding resource allocation overhead. Specifically, we choose to transmit the QSI on those physical channels whose locations on the subframe grid are fixed - the broadcast or the synchronization channels. Then, we identified that the timing reacquisition process further increased the ON time, especially when the coverage is low, leading to increased energy consumption. To alleviate this problem, we introduced a robust QSI signal using the data channel. Although this signal required additional resources, it helped the UEs in low coverage to obtain both the paging and timing information in parallel, which reduced the ON time and paging decoding complexity, thereby saving energy. Our DRX with quick sleeping solutions demonstrated more than 45% improvement in energy efficiency.

In the aforementioned DRX with quick sleeping mechanism, the timing resolution considered was at the symbol level (the timing was designated to be correct if the UE finds the correct symbol number). In Chapter 3, we first showed that the paging decode operation is very sensitive to timing offset and any deviation in timing beyond the cyclic prefix length degrades the decoding process. In order to obtain accurate sample-level timing detection, we explored the conventional timing

acquisition algorithms - cyclic prefix autocorrelation and the synchronization signal detection. We demonstrated that the conventional mechanisms require substantial ON time for reacquiring the symbol timing within tolerable limits and hence lead to increased energy consumption.

To mitigate this problem, we introduced the enhanced Primary Synchronization Signal (ePSS) within the LTE/LTE-A standardization framework and proposed a novel DRX mechanism which uses our ePSS for faster timing resynchronization and reduced energy consumption. We described two simple methods to design the ePSS signal - by using multiple legacy PSS sequences and by using longer ZC sequences and indicated that our ePSS design requires less than 1.5% network resource overhead for base-station bandwidths of 5 MHz or more. We also illustrated that the modified DRX mechanism using ePSS as QSI would result in 1.2 to 1.8 times improvement in the battery life of the low-coverage, low-complexity MTC devices.

Having described energy efficient mechanisms for MTC UEs in the downlink in Chapter 2 and Chapter 3, the problem of improving the energy efficiency of the low-coverage MTC devices in the uplink was addressed in Chapter 4. We showed that the energy efficiency of the MTC UE increases if the base station adopts CFO estimation mechanisms that reduce the residual CFO to negligible limits. We proposed a ML based CFO estimation mechanism that uses the data and pilot repetitions in LTE/LTE-A and illustrated that it significantly outperforms the legacy CFO estimation technique using the phase of the correlation between consecutive data repetitions.

An important contribution from this work was the evaluation of our CFO estimation algorithm for the large transport block transmission in the NB-IoT. Various studies in NB-IoT indicated that the large transport block transmission increases the effective data rate and reduces the retransmission time, thereby saving energy.

We showed that incorporating our ML based CFO estimation mechanism results in further reduction in the number of retransmissions for NB-IoT. Finally, we proposed a variation of the LTE/LTE-A frame structure incorporating additional pilot signals during the initial MTC transmissions, which assists in faster CFO estimation at the eNB with minimal overhead.

From the standardization perspective, our DRX with QSI and ePSS solutions are applicable to UE categories of CAT-M1, CAT-0 and above, since they operate on a bandwidth of at least 1.4 MHz. These contributions were presented in the MTC Radio Access network - Layer 1 (RAN-1) meetings of the 3GPP and played a vital role in - a) extending the DRX cycle length beyond the initially proposed 2.56 s to 2621.44 s for CAT-M1 UEs, b) developing a simplified paging control channel for CAT-M1 devices with a single Downlink Control Information (DCI) format to reduce the number of blind hypotheses and c) identifying that UE resynchronization also plays a major role in increased energy consumption of low coverage MTC UEs. In fact, the topic of improving resynchronization (and initial synchronization) is still an open study item for LTE MTC Release 14. Recently, the focus of the LTE standardization has shifted towards defining NB-IoT and 5G NR specifications. Nevertheless, the learning and the basic principles adopted in our solutions provide the impetus to design more energy efficient mechanisms in the downlink for the forthcoming NB-IoT and 5G NR standards.

Our ML based CFO estimation technique in the uplink is not only applicable to all the LTE UE categories, but also easily adoptable for other wireless communication standards using data/pilot repetitions. But our proposal for increased DMRS density was not considered for standardization, in order to maintain full compatibility with legacy UEs. Considering that novel schemes for uplink pilot design are open study

items for 5G NR, we believe that it would be beneficial to develop these schemes such that they allow for faster and robust CFO estimation in low coverage.

## 5.1 Directions for Future Work

The IoT scenario and the MTC mechanisms present numerous challenging research problems. Some interesting avenues for future research are summarized below.

### 5.1.1 Coverage Enhancement for LTE MTC Using Massive MIMO

Massive Multi-Input-Multi-Output (MIMO) is a communication technology that has attracted the interest of researchers worldwide in recent years. It is a successor of the conventional MIMO technology which has been well studied and applied in various wireless communication standards like WLAN (802.11), WiMax (802.16) and LTE. It has been proved that the MIMO technology improves the reliability and the capacity of wireless communications significantly. The MIMO technology has evolved from addressing point-to-point links where two devices with multiple antennas communicate with each other, to providing efficient communication mechanisms for Multi-User MIMO (MU-MIMO) systems, where a base station with multiple antennas communicates with a set of single antenna devices. The MU-MIMO system model fits the case of MTC where the network comprises of multiple, low-complexity, single antenna users. The current MU-MIMO systems employ few number of antennas (for example, 8 in LTE) at the base station and hence extract relatively modest gains in spectral efficiency. The massive MIMO technology employs a large number of antennas at the base station (100 or more) in order to enhance the capacity and

spectral efficiency of the system. In [120], it has been shown that massive MIMO can provide a spectral efficiency as high as 26.5 bps/Hz.

A prime advantage of massive MIMO is its energy efficient mode of operation when compared to the conventional Single-Input-Single-Output (SISO) system. In [121], it is shown that the transmit power of each user in a massive MIMO system is reduced when compared to the SISO system for the same performance. This reduction in user transmission power is proportional to $M$, the number of antennas at the base station with perfect CSI or to $\sqrt{M}$ in the case of imperfect CSI. This leads to energy efficient operation in the uplink. Similarly, in the downlink, the reduction in base station transmit power is proportional to $K$ and $\sqrt{K}$ for perfect CSI and imperfect CSI respectively, where $K$ is the number of users. In other words, massive MIMO can provide extended coverage for the same amount of power. The MTC scenario is bound to have more than one user to be served at a given instant of time owing to the large number of devices present in the network. This renders massive MIMO to be a suitable candidate for coverage enhancement in MTC when some CSI (perfect or imperfect) information is available.

It would be interesting to examine the use of massive MIMO to improve the SNR during the initialization phase in LTE/LTE-A, where the CSI is completely unknown. Recently, beamforming based initial access techniques are being proposed for millimeter wave communications [122, 123]. While these works use the Line Of Sight (LOS) propagation model for the channel and multiple antennas at the UE, it would be important to evaluate the performance for single antenna UEs in Non Line Of Sight (NLOS) channels and also to standardize massive MIMO operation in 5G.

Secondly, recent standardization activities for the 5G NR in LTE/LTE-A [124] discuss grant-free access methods for UE transmission [125]. These grant-free meth-

ods will be a perfect foil for massive MIMO base-stations, since the UEs can follow a simple transmission mechanism and the base station can incorporate improved detection/decoding mechanisms of the UE signals using the large antenna array processing. For example, large antenna arrays can render better directivity for the base-station to employ digital beamforming and process the UE signals one direction at a time, thereby mitigating the interference from the other directions. Developing massive MIMO based grant-free mechanisms to address the massive uplink access in IoT would also be a potential avenue for future research.

### 5.1.2 Exploring LTE in Unlicensed Bands (LTE-U) for MTC

With the exponential increase in the number of devices requiring network access, it would be highly difficult for the current frequency spectrum to provide resources for all these devices. Moreover, the purchase of a licensed spectrum is expensive and its availability is limited. Therefore, recent research has moved towards exploring unlicensed spectral bands, which has a large amount of available spectrum. For example, in the 5 GHz band, the available spectrum spans approximately 500 MHz [126]. Since, LTE/LTE-A provides better system capacity, higher coverage and easy integration with existing systems, deployment of LTE-Unlicensed (LTE-U) is being considered by 3GPP. The LTE-A standard employs carrier aggregation to provide additional bandwidth. In LTE-U, this idea is being extended towards Licensed Assisted Access (LAA) where the licensed and unlicensed bands are aggregated. Therefore, LTE-U can potentially combine the advantages of LTE-A with the large bandwidth available in the unlicensed spectrum to handle the high data demand. This renders LTE-U to be a good candidate for MTC.

The main challenge for LTE-U is to co-exist with the other technologies like Wireless Fidelity (WiFi) and Bluetooth in the unlicensed band [127]. In this regard, regulatory mechanisms like Listen Before Talk (LBT), dynamic frequency selection and Clear Channel Assessment (CCA) for the low-complexity MTC UEs have to investigated. A major advantage of using unlicensed band is data offloading and co-operative communications. LTE-U for cooperative communications is an appealing research topic, where the MTC UEs could use WiFi to exchange information amongst themselves, while being connected to a primary LTE cellular network. One application of such a framework would be optimize the transmission of the Channel Quality Indication (CQI) in the uplink. The LTE-U framework can also be used along with the massive MIMO solution, where cooperative CQI feedback mechanisms can be employed to improve the system performance.

## 5.2 Concluding Remarks

The advent of IoT and the emergence of a plethora of new challenges has not only made the field of wireless communication exciting, but also rekindled the interest in developing novel physical layer solutions adhering to the diverse IoT requirements. We believe that this is a great time to contribute to this field with innovative and practical solutions. The contributions from this thesis provide a stepping stone for analyzing the performance of IoT devices adopting the LTE/LTE-A MTC mechanisms. The energy efficiency and extended coverage aspects evaluated in this work are identified to be key performance indicators for the design and development of next generation wireless communication technologies hosting the IoT. Lastly, although this research is closely tied to LTE/LTE-A, it is fairly straightforward to extend the ideas to other standards/technologies for facilitating the IoT.

# Bibliography


[1] A. Zanella, N. Bui, A. Castellani, L. Vangelista, and M. Zorzi, "Internet of things for smart cities," *IEEE Internet Things J.*, vol. 1, no. 1, pp. 22–32, 2014.

[2] L. Da Xu, W. He, and S. Li, "Internet of things in industries: A survey," *IEEE Trans. Ind. Informat.*, vol. 10, no. 4, pp. 2233–2243, 2014.

[3] N. Dlodlo and J. Kalezhi, "The Internet of things in agriculture for sustainable rural development," in *Proc. IEEE Int. Conf. on Emerging Trends in Networks and Computer Communications*, 2015, pp. 13–18.

[4] C. Kalalas, L. Thrybom, and J. Alonso-Zarate, "Cellular communications for smart grid neighborhood area networks: A survey," *IEEE Access*, vol. 4, pp. 1469–1493, 2016.

[5] L. Catarinucci, D. de Donno, L. Mainetti, L. Palano, L. Patrono, M. L. Stefanizzi, and L. Tarricone, "An IoT-aware architecture for smart healthcare systems," *IEEE Internet Things J.*, vol. 2, no. 6, pp. 515–526, 2015.

[6] G. Kortuem, F. Kawsar, V. Sundramoorthy, and D. Fitton, "Smart objects as building blocks for the Internet of things," *IEEE Internet Comput.*, vol. 14, no. 1, pp. 44–51, 2010.

[7] Ericsson, "Cellular networks for massive IoT (whitepaper)," Jan 2016.

[8] "IEEE standard for local and metropolitan area networks–part 15.4: Low-rate wireless personal area networks (LR-WPANs)," *IEEE Std 802.15.4-2011*, 2011.

[9] D. Raychaudhuri and N. B. Mandayam, "Frontiers of wireless and mobile communications," *Proc. of the IEEE*, vol. 100, no. 4, pp. 824–840, 2012.

[10] "IEEE standard for information technology–telecommunications and information exchange between systems–local and metropolitan area networks–specific requirements–part 11: Wireless lan medium access control (MAC) and physical layer (PHY) specifications," *IEEE Std 802.11-2012*, 2012.

[11] S. Aust, R. V. Prasad, and I. G. Niemegeers, "IEEE 802.11 ah: Advantages in standards and further challenges for sub 1 GHz Wi-Fi," in *IEEE Int. Conf. on Commun.*, 2012, pp. 6885–6889.

[12] D. Astely, E. Dahlman, G. Fodor, S. Parkvall, and J. Sachs, "LTE release 12 and beyond," *IEEE Commun. Mag.*, vol. 51, no. 7, 2013.

[13] I. Hwang, B. Song, and S. S. Soliman, "A holistic view on hyper-dense heterogeneous and small cell networks," *IEEE Commun. Mag.*, vol. 51, no. 6, pp. 20–27, 2013.

[14] A. Damnjanovic, J. Montojo, Y. Wei, T. Ji, T. Luo, M. Vajapeyam, T. Yoo, O. Song, and D. Malladi, "A survey on 3GPP heterogeneous networks," *IEEE Wireless Commun.*, vol. 18, no. 3, pp. 10–21, 2011.

[15] J. Ramiro and K. Hamied, *Self-Organizing Networks (SON): Self-Planning, Self-Optimization and Self-Healing for GSM, UMTS and LTE.* John Wiley & Sons, 2011.

[16] M. Peng, D. Liang, Y. Wei, J. Li, and H.-H. Chen, "Self-configuration and self-optimization in LTE-Advanced heterogeneous networks," *IEEE Commun. Mag.*, vol. 51, no. 5, pp. 36–45, 2013.

[17] Nokia, "LTE evolution for IoT connectivity (whitepaper)," 2016.

[18] A. Rajandekar and B. Sikdar, "A survey of MAC layer issues and protocols for machine-to-machine communications," *IEEE Internet Things J.*, vol. 2, no. 2, pp. 175–186, 2015.

[19] X. Liang, X. Li, M. Barua, L. Chen, R. Lu, X. Shen, and H. Luo, "Enabling pervasive healthcare through continuous remote health monitoring," *IEEE Wireless Commun.*, vol. 19, no. 6, pp. 10–18, 2012.

[20] M. R. Palattella, M. Dohler, A. Grieco, G. Rizzo, J. Torsner, T. Engel, and L. Ladid, "Internet of things in the 5G era: Enablers, architecture, and business models," *IEEE J. Sel. Areas Commun.*, vol. 34, no. 3, pp. 510–527, 2016.

[21] Researchmoz.us, "Low power wide area Internet of things (LPWA-IoT) market forecasts to 2020 and MNO approaches," Apr. 2016.

[22] Sigfox, https://www.sigfox.com/, Last retrieved on 15th May 2017.

[23] Semtech, https://www.semtech.com/, Last retrieved on 15th May 2017.

[24] J. Petajajarvi, K. Mikhaylov, A. Roivainen, T. Hanninen, and M. Pettissalo, "On the coverage of LPWANs: range evaluation and channel attenuation model for LoRa technology," in *Proc. IEEE 14th Int. Conf. on ITS Telecommun.*, 2015, pp. 55–59.

[25] N. Sornin, M. Luis, T. Eirich, T. Kramp, and O. Hersent, "LoRaWAN specification V1," LoRa Alliance, Tech. Rep., 2015.

[26] Ingenu, "RPMA technology for the Internet of things," Ingenu, Tech. Rep., 2016.

[27] Telensa, http://www.telensa.com/, Last retrieved on 15th May 2017.

[28] Weightless, http://www.weightless.org/, Last retrieved on 15th May 2017.

[29] 802.11 Task Group, "Long range low power (LRLP) operation in 802.11: Use cases and functional requirements: Guidelines for par development," *IEEE P802.11*, 2016.

[30] ETSI, "Low throughput networks (LTN); use cases for low throughput networks," ETSI GS LTN 001 V1.1.1, Sep. 2014.

[31] ——, "Low throughput networks (LTN); functional architecture," ETSI GS LTN 002 V1.1.1, Sep. 2014.

[32] ——, "Low throughput networks (LTN); protocols and interfaces," ETSI GS LTN 003 V1.1.1, Sep. 2014.

[33] R. Ratasuk, S. Iraji, K. Hugl, L. Wang, and A. Ghosh, "Performance of low-cost LTE devices for advanced metering infrastructure," in *Proc. IEEE 77th Veh. Tech. Conf.-Spring*, 2013, pp. 1–5.

[34] Y. Chen and W. Wang, "Machine-to-machine communication in LTE-A," in *Proc. IEEE 72nd Veh. Technol. Conf.-Fall*, 2010, pp. 1–4.

[35] S.-Y. Lien, K.-C. Chen, and Y. Lin, "Toward ubiquitous massive accesses in 3GPP machine-to-machine communications," *IEEE Commun. Mag.*, vol. 49, no. 4, pp. 66–74, 2011.

[36] T. Taleb and A. Kunz, "Machine type communications in 3GPP networks: potential, challenges, and solutions," *IEEE Commun. Mag.*, vol. 50, no. 3, pp. 178–184, 2012.

[37] A. G. Gotsis, A. S. Lioumpas, and A. Alexiou, "M2M scheduling over LTE: Challenges and new perspectives," *IEEE Veh. Technol. Mag.*, vol. 7, no. 3, pp. 34–39, 2012.

[38] F. Ghavimi and H.-H. Chen, "M2M communications in 3GPP LTE/LTE-A networks: Architectures, service requirements, challenges, and applications," *IEEE Commun. Surveys Tuts.*, 2015.

[39] J. J. Nielsen, G. C. Madueño, N. K. Pratas, R. B. Sørensen, C. Stefanovic, and P. Popovski, "What can wireless cellular technologies do about the upcoming smart metering traffic?" *IEEE Commun. Mag.*, vol. 53, no. 9, pp. 41–47, 2015.

[40] G. C. Madueño, J. J. Nielsen, D. M. Kim, N. K. Pratas, Č. Stefanović, and P. Popovski, "Assessment of LTE wireless access for monitoring of energy distribution in the smart grid," *IEEE J. Sel. Areas Commun.*, vol. 34, no. 3, pp. 675–688, 2016.

[41] C.-H. Wei, R.-G. Cheng, and F. M. Al-Taee, "Dynamic radio resource allocation for group paging supporting smart meter communications," in *Proc. IEEE 3rd Int. Conf. on Smart Grid Commun.*, 2012, pp. 659–663.

[42] R. Ratasuk, A. Prasad, Z. Li, A. Ghosh, and M. A. Uusitalo, "Recent advancements in M2M communications in 4G networks and evolution towards 5G," in *Proc. IEEE 18th Int. Conf. on Intelligence in Next Generation Netw.*, 2015, pp. 52–57.

[43] 3GPP, "Study on provision of low-cost machine-type communications (MTC) user equipments (UEs) based on LTE," 3GPP, TR 36.888, Jun. 2013.

[44] ——, "Study on machine-type communications (MTC) and other mobile data applications communications enhancements," 3GPP, TR 23.887, Dec. 2013.

[45] R. Ratasuk, B. Vejlgaard, N. Mangalvedhe, and A. Ghosh, "NB-IoT system for M2M communication," in *Proc. IEEE Wireless Commun. and Netw. Conf.*, 2016, pp. 1–5.

[46] 3GPP TSG RAN, "RP-152284, Revised Work Item: Narrowband IoT (NB-IoT)," 3GPP, Dec. 2015.

[47] ——, "R1-156010, NB-LTE General L1 Concept Description," 3GPP, Oct. 2015.

[48] 3GPP, "Cellular system support for ultra-low complexity and low throughput internet of things (CIoT)," 3GPP, TR 45.820, Dec. 2015.

[49] N. M. Balasubramanya, L. Lampe, G. Vos, and S. Bennett, "Introducing quick sleeping using the broadcast channel for 3GPP LTE MTC," in *Proc. IEEE Global Telecommun. Conf. Wkshps.*, 2014, pp. 606–611.

[50] ——, "DRX with quick sleeping: A novel mechanism for energy-efficient IoT using LTE/LTE-A," *IEEE Internet Things J.*, vol. 3, no. 3, pp. 398–407, 2016.

[51] N. M. Balasubramanya, L. H.-J. Lampe, and G. G. Vos, "Quick paging method and apparatus in LTE," 2015, US Patent App. 14/799,513.

[52] N. M. Balasubramanya, L. Lampe, G. Vos, and S. Bennett, "On timing reacquisition and enhanced primary synchronization signal (ePSS) design for energy efficient 3GPP LTE MTC," *IEEE Trans. Mobile Comput.*, 2016.

[53] G. G. Vos, N. M. Balasubramanya, S. J. Bennett, and L. H.-J. Lampe, "Method and system for providing and using enhanced primary synchronization signal for LTE," 2016, US Patent App. 15/010,192.

[54] N. M. Balasubramanya, L. Lampe, G. Vos, and S. Bennett, "Low snr uplink CFO estimation for energy efficient IoT using LTE," *IEEE Access*, vol. 4, pp. 3936–3950, 2016.

[55] ——, "Method and system for carrier frequency offset estimation in LTE MTC device communication," 2016, US Patent App. 15/010,192.

[56] 3GPP, "Technical specification group services and system aspects; architecture enhancements to facilitate communications with packet data networks and applications (release 13)," 3GPP, TS 23.682, Mar. 2016.

[57] ——, "Evolved universal terrestrial radio access (E-UTRA); physical layer procedures," 3GPP, TS 36.213, Mar. 2014.

[58] H. Holma and A. Toskala, *LTE for UMTS: Evolution to LTE-Advanced*. John Wiley & Sons, 2011.

[59] 3GPP, "Evolved universal terrestrial radio access (E-UTRA); medium access control (MAC) protocol specification," 3GPP, TS 36.321, Mar. 2014.

[60] ——, "Evolved universal terrestrial radio access (E-UTRA); user equipment (UE) procedures in idle mode," 3GPP, TS 36.304, Mar. 2014.

[61] ——, "Evolved universal terrestrial radio access (E-UTRA); physical channels and modulation," 3GPP, TS 36.211, Mar. 2014.

[62] ——, "Evolved universal terrestrial radio access (E-UTRA); multiplexing and channel coding," 3GPP, TS 36.212, Dec. 2013.

[63] J.-J. Van de Beek, M. Sandell, P. O. Borjesson *et al.*, "ML estimation of time and frequency offset in OFDM systems," *IEEE Trans. Signal Process.*, vol. 45, no. 7, pp. 1800–1805, 1997.

[64] M. Speth, F. Classen, and H. Meyr, "Frame synchronization of OFDM systems in frequency selective fading channels," in *Proc. IEEE 47th Veh. Technol. Conf.*, vol. 3, 1997, pp. 1807–1811.

[65] J.-B. Seo, S.-Q. Lee, N.-H. Park, H.-W. Lee, and C.-H. Cho, "Performance analysis of sleep mode operation in IEEE 802.16 e," in *Proc. IEEE 60th Veh. Technol. Conf.-Fall*, vol. 2, 2004, pp. 1169–1173.

[66] Y. Xiao, "Energy saving mechanism in the IEEE 802.16 e wireless MAN," *IEEE Commun. Lett.*, vol. 9, no. 7, pp. 595–597, 2005.

[67] Y. Zhang and M. Fujise, "Energy management in the IEEE 802.16 e MAC," *IEEE Commun. Lett.*, vol. 10, no. 4, pp. 311–313, 2006.

[68] S. Baek, J. J. Son, and B. D. Choi, "Performance analysis of sleep mode operation for IEEE 802.16 m advanced WMAN," in *Proc. IEEE Int. Conf. on Commun. Wkshps.*, 2009, pp. 1–5.

[69] K. De Turck, S. De Vuyst, D. Fiems, S. Wittevrongel, and H. Bruneel, "Performance of the sleep-mode mechanism of the new IEEE 802.16 m proposal for correlated downlink traffic," in *Proc. Int. Conf. on Network Control and Optimization*. Springer, 2009, pp. 152–165.

[70] E. Hwang, K. J. Kim, J. J. Son, and B. D. Choi, "The power-saving mechanism with periodic traffic indications in the IEEE 802.16 e/m," *IEEE Trans. Veh. Technol.*, vol. 59, no. 1, pp. 319–334, 2010.

[71] S. Jin, M. Choi, and S. Choi, "Performance analysis of IEEE 802.16 m sleep mode for heterogeneous traffic," *IEEE Commun. Lett.*, vol. 14, no. 5, pp. 405–407, 2010.

[72] S.-R. Yang and Y.-B. Lin, "Modeling UMTS discontinuous reception mechanism," *IEEE Trans. Wireless Commun.*, vol. 4, no. 1, pp. 312–319, 2005.

[73] S.-R. Yang, "Dynamic power saving mechanism for 3G UMTS system," *Mobile Networks and Applications*, vol. 12, no. 1, pp. 5–14, 2007.

[74] S. Yang, M. Yoo, and Y. Shin, "Adaptive discontinuous reception mechanism for power saving in UMTS," *IEEE Commun. Lett.*, vol. 11, no. 1, pp. 40–42, 2007.

[75] S.-R. Yang, S.-Y. Yan, and H.-N. Hung, "Modeling UMTS power saving with bursty packet data traffic," *IEEE Trans. Mobile Comput.*, vol. 6, no. 12, pp. 1398–1409, 2007.

[76] S.-r. Yang, P. Lin, and P.-t. Huang, "Modeling power saving for GAN and UMTS interworking," *IEEE Trans. Wireless Commun.*, vol. 7, no. 12, pp. 5326–5335, 2008.

[77] C. S. Bontu and E. Illidge, "DRX mechanism for power saving in LTE," *IEEE Commun. Mag.*, vol. 47, no. 6, pp. 48–55, 2009.

[78] L. Zhou, H. Xu, H. Tian, Y. Gao, L. Du, and L. Chen, "Performance analysis of power saving mechanism with adjustable DRX cycles in 3GPP LTE," in *Proc. IEEE 68th Veh. Technol. Conf.-Fall*, 2008, pp. 1–5.

[79] J. Wigard, T. Kolding, L. Dalsgaard, and C. Coletti, "On the user performance of LTE UE power savings schemes with discontinuous reception in LTE," in *Proc. IEEE Int. Conf. on Commun. Wkshps.*, 2009, pp. 1–5.

[80] S. Jin and D. Qiao, "Numerical analysis of the power saving in 3GPP LTE advanced wireless networks," *IEEE Trans. Veh. Technol.*, vol. 61, no. 4, pp. 1779–1785, 2012.

[81] T. Kolding, J. Wigard, and L. Dalsgaard, "Balancing power saving and single user experience with discontinuous reception in LTE," in *Proc. IEEE Int. Symp. on Wireless Commun. Syst.*, 2008, pp. 713–717.

[82] S. C. Jha, A. T. Koc, and R. Vannithamby, "Optimization of discontinuous reception (DRX) for mobile internet applications over LTE," in *Proc. IEEE Veh. Technol. Conf.-Fall*, 2012, pp. 1–5.

[83] Y. Y. Mihov, K. M. Kassev, and B. P. Tsankov, "Analysis and performance evaluation of the DRX mechanism for power saving in LTE," in *Proc. IEEE 26th Convention of Electrical and Electronics Engineers in Israel*, 2010, pp. 000 520–000 524.

[84] S. Fowler, "Study on power saving based on radio frame in LTE wireless communication system using drx," in *Proc. IEEE Global Telecommun. Conf. Wkshps.*, 2011, pp. 1062–1066.

[85] S. Fowler, R. S. Bhamber, and A. Mellouk, "Analysis of adjustable and fixed DRX mechanism for power saving in LTE/LTE-Advanced," in *Proc. IEEE Int. Conf. on Commun.*, 2012, pp. 1964–1969.

[86] A. T. Koc, S. C. Jha, R. Vannithamby, and M. Torlak, "Device power saving and latency optimization in LTE-A networks through DRX configuration," *IEEE Trans. Wireless Commun.*, vol. 13, no. 5, pp. 2614–2625, 2014.

[87] C.-C. Tseng, H.-C. Wang, F.-C. Kuo, K.-C. Ting, H.-H. Chen, and G.-Y. Chen, "Delay and power consumption in LTE/LTE-A DRX mechanism with mixed short and long cycles," *IEEE Trans. Veh. Technol.*, vol. 65, no. 3, pp. 1721–1734, 2016.

[88] K. Zhou, N. Nikaein, and T. Spyropoulos, "LTE/LTE-A discontinuous reception modeling for machine type communications," *IEEE Wireless Commun. Lett.*, vol. 2, no. 1, pp. 102–105, 2013.

[89] T. Tirronen, A. Larmo, J. Sachs, B. Lindoff, and N. Wiberg, "Reducing energy consumption of LTE devices for machine-to-machine communication," in *Proc. IEEE Global Telecommun. Conf. Wkshps.*, 2012, pp. 1650–1656.

[90] S. Kim, K. Jung, J. Choi, and Y. Kwak, "Improving LTE/LTE-A UE power efficiency with extended DRX cycle," in *Proc. IEEE 80th Veh. Technol. Conf.-Fall*, 2014, pp. 1–5.

[91] S. Fowler, A. O. Shahidullah, M. Osman, J. M. Karlsson, and D. Yuan, "Analytical evaluation of extended DRX with additional active cycles for light traffic," *Elsevier - Computer Networks*, vol. 77, pp. 90–102, 2015.

[92] S. C. Jha, A. T. Koc, and R. Vannithamby, "Device power saving mechanisms for low cost MTC over LTE networks," in *Proc. IEEE Int. Conf. on Commun. Wkshps.*, 2014, pp. 412–417.

[93] H. Chao, Y. Chen, and J. Wu, "Power saving for machine to machine communications in cellular networks," in *Proc. IEEE Global Commun. Conf. Wkshps.*, 2011, pp. 389–393.

[94] C.-Y. Tu, C.-Y. Ho, and C.-Y. Huang, "Energy-efficient algorithms and evaluations for massive access management in cellular based machine to machine communications," in *Proc. IEEE Veh. Technol. Conf.-Fall*, 2011, pp. 1–5.

[95] J.-P. Cheng, C.-h. Lee, and T.-M. Lin, "Prioritized random access with dynamic access barring for RAN overload in 3GPP LTE-A networks," in *Proc. IEEE Global Commun. Conf. Wkshps.*, 2011, pp. 368–372.

[96] S. Duan, V. Shah-Mansouri, and V. W. Wong, "Dynamic access class barring for M2M communications in LTE networks," in *Proc. IEEE Global Commun. Conf.*, 2013, pp. 4747–4752.

[97] M. Gerasimenko, V. Petrov, O. Galinina, S. Andreev, and Y. Koucheryavy, "Impact of machine-type communications on energy and delay performance of random access channel in LTE-Advanced," *Wiley Online Library - Transactions on Emerging Telecommunication Technologies*, vol. 24, no. 4, pp. 366–377, 2013.

[98] M. Hasan, E. Hossain, and D. Niyato, "Random access for machine-to-machine communication in LTE-Advanced networks: issues and approaches," *IEEE Commun. Mag.*, vol. 51, no. 6, pp. 86–93, 2013.

[99] C. Y. Ho and C.-Y. Huang, "Energy-saving massive access control and resource allocation schemes for M2M communications in OFDMA cellular networks," *IEEE Wireless Commun. Lett.*, vol. 1, no. 3, pp. 209–212, 2012.

[100] S. Andreev, A. Larmo, M. Gerasimenko, V. Petrov, O. Galinina, T. Tirronen, J. Torsner, and Y. Koucheryavy, "Efficient small data access for machine-type communications in LTE," in *Proc. IEEE Int. Conf. on Commun.*, 2013, pp. 3569–3574.

[101] K. Wang, J. Alonso-Zarate, and M. Dohler, "Energy-efficiency of LTE for small data machine-to-machine communications," in *Proc. IEEE Int. Conf. on Commun.*, 2013, pp. 4120–4124.

[102] H. S. Dhillon, H. C. Huang, H. Viswanathan, and R. A. Valenzuela, "Power-efficient system design for cellular-based machine-to-machine communications," *IEEE Trans. Wireless Commun.*, vol. 12, no. 11, pp. 5740–5753, 2013.

[103] Y. Zhou, T. Zhang, Z. Zeng, Y. Li, and Y. Han, "LTE uplink coverage enhancement techniques based on enhanced TTI bundling," in *Proc. IEEE Int. Conf. on Wireless Commun., Netw. and Mobile Comput.*, 2012, pp. 1–4.

[104] Y. Yuan, Z. Zuo, Y. Guan, X. Chen, W. Luo, Q. Bi, P. Chen, and X. She, "LTE-Advanced coverage enhancements," *IEEE Commun. Mag.*, vol. 52, no. 10, pp. 153–159, 2014.

[105] G. Naddafzadeh-Shirazi, L. Lampe, G. Vos, and S. Bennett, "Coverage enhancement techniques for machine-to-machine communications over LTE," *IEEE Commun. Mag.*, vol. 53, no. 7, pp. 192–200, 2015.

[106] 3GPP, "User equipment (UE) radio transmission and reception." 3GPP, TS 36.101, Mar. 2014.

[107] W. Xu and K. Manolakis, "Robust synchronization for 3GPP LTE system," in *Proc. IEEE Global Telecommun. Conf.*, 2010, pp. 1–5.

[108] C.-L. Chen and S.-G. Chen, "Non-coherent cell identification detection methods and statistical analysis for OFDM systems," *IEEE Trans. Commun.*, vol. 58, no. 11, pp. 3231–3243, 2010.

[109] F. Berggren and B. M. Popović, "A non-hierarchical cell search scheme," in *Proc. IEEE Wireless Commun. and Netw. Conf.*, 2007, pp. 2300–2304.

[110] J.-W. Lee and Y.-H. Lee, "Rapid cell search in OFDM-based cellular systems," in *Proc. IEEE 61st Veh. Technol. Conf.-Spring*, vol. 2, 2005, pp. 1273–1277.

[111] P. Osti, P. Lassila, S. Aalto, A. Larmo, and T. Tirronen, "Analysis of PDCCH performance for M2M traffic in LTE," *IEEE Trans. Veh. Technol.*, vol. 63, no. 9, pp. 4357–4371, 2014.

[112] P. Frenger, H. Koorapaty, and J.-C. Guey, "Evaluation of control channel performance with adaptive radio unit activation in LTE," in *Proc. IEEE 75th Veh. Technol. Conf.-Spring*, 2012, pp. 1–5.

[113] J. Milos and S. Hanus, "Performance analysis of PCFICH and PDCCH LTE control channels," *Radioengineering*, vol. 23, no. 1, 2014.

[114] J. Zhu and H. Li, "On the performance of LTE physical downlink shared channel," in *Proc. IEEE Int. Conf. on Comput. Sci. and Netw. Technol.*, vol. 2, 2011, pp. 983–986.

[115] F. Riehle, *Frequency standards: basics and applications*. John Wiley & Sons, 2006.

[116] Qualcomm Incorporated, "R4-141241 - Reply LS on AGC and frequency error for D2D, GPP TSG-RAN WG2 Meeting 57bis, St. Julians, Malta 26 - 30 March 2007."

[117] S. Ye, S. H. Wong, and C. Worrall, "Enhanced physical downlink control channel in LTE Advanced Release 11," *IEEE Commun. Mag.*, vol. 51, no. 2, pp. 82–89, 2013.

[118] Nokia, "R2-071285 - DRX parameters in LTE, 3GPP TSG-RAN WG4 Meeting 70, San Francisco, USA, 10th-14th Feb., 2014."

[119] M. Morelli and M. Moretti, "Robust frequency synchronization for OFDM-based cognitive radio systems," *IEEE Trans. Wireless Commun.*, vol. 7, no. 12, pp. 5346–5355, 2008.

[120] L. Lu, G. Y. Li, A. L. Swindlehurst, A. Ashikhmin, and R. Zhang, "An overview of massive MIMO: benefits and challenges," *IEEE J. Sel. Topics Signal Process.*, vol. 8, no. 5, pp. 742–758, 2014.

[121] H. Q. Ngo, E. G. Larsson, and T. L. Marzetta, "Energy and spectral efficiency of very large multiuser MIMO systems," *IEEE Trans. Commun.*, vol. 61, no. 4, pp. 1436–1449, 2013.

[122] M. Giordani, M. Mezzavilla, and M. Zorzi, "Initial access in 5G mmwave cellular networks," *IEEE Commun. Mag.*, vol. 54, no. 11, pp. 40–47, 2016.

[123] C. N. Barati, S. A. Hosseini, M. Mezzavilla, T. Korakis, S. S. Panwar, S. Rangan, and M. Zorzi, "Initial access in millimeter wave cellular systems," *IEEE Trans. Wireless Commun.*, vol. 15, no. 12, pp. 7926–7940, 2016.

[124] 3GPP, "Study on new radio (NR) access technology," 3rd Generation Partnership Project (3GPP), TR 38.912, Sep. 2016.

[125] C. Bockelmann, N. Pratas, H. Nikopour, K. Au, T. Svensson, C. Stefanovic, P. Popovski, and A. Dekorsy, "Massive machine-type communications in 5G: Physical and mac-layer solutions," *IEEE Commun. Mag.*, vol. 54, no. 9, pp. 59–65, 2016.

[126] R. Ratasuk, N. Mangalvedhe, and A. Ghosh, "LTE in unlicensed spectrum using licensed-assisted access," in *Proc. IEEE Global Telecommun. Conf. Wkshps.*, 2014, pp. 746–751.

[127] F. M. Abinader, E. P. Almeida, F. S. Chaves, A. M. Cavalcante, R. D. Vieira, R. C. Paiva, A. M. Sobrinho, S. Choudhury, E. Tuomaala, K. Doppler *et al.*, "Enabling the coexistence of LTE and Wi-Fi in unlicensed bands," *IEEE Commun. Mag.*, vol. 52, no. 11, pp. 54–61, 2014.

# Appendix A

# Proof of Cramér-Rao Bound in Eq. (4.13)

In this appendix, we derive the Cramér-Rao bound for our ML based CFO estimator for repeated data. We begin with re-writing Eq. (4.9) for a given subcarrier $m$ and the Gaussian channel as

$$\boldsymbol{Y}(m) = R(m)\boldsymbol{u}(m) + \boldsymbol{W}(m), \tag{A.1}$$

where $\boldsymbol{Y}(m) = [Y_0(m), Y_1(m), \cdots Y_{N-1}(m)]^T$ is the received signal vector on the $m$-th subcarrier and $R(m)$ denotes the data transmitted on the $m$-th subcarrier. The CFO vector is given by $\boldsymbol{u}(m) = [1, \mathrm{e}^{(\frac{j2\pi\epsilon LK}{N_\mathrm{s}})}, \mathrm{e}^{(\frac{j2\pi\epsilon 2LK}{N_\mathrm{s}})}, \cdots \mathrm{e}^{(\frac{j2\pi\epsilon(N-1)LK}{N_\mathrm{s}})}]^T$ and the Gaussian noise vector is indicated by $\boldsymbol{W}(m) = [W_0(m), W_1(m), \cdots W_{N-1}(m)]^T$, which has zero mean and covariance matrix $\sigma^2(m)\boldsymbol{I}_N$ ($\boldsymbol{I}_N$ is the identity matrix of order $N$). The SNR is calculated as

$$\Psi = \frac{1}{M}\sum_{m=0}^{M-1}\frac{|R(m)|^2}{\sigma^2(m)} \tag{A.2}$$

This is similar to the Eq. (4) in [119], for which the Cramér-Rao bound is derived using the Fisher information matrix $\boldsymbol{F}$ (Eq. (42) in [119]). In our case, we obtain

$$\boldsymbol{F} = \begin{bmatrix} \boldsymbol{D} & \boldsymbol{V} \\ \boldsymbol{V}^T & \beta\boldsymbol{R}^H\boldsymbol{P}^{-1}\boldsymbol{R} \end{bmatrix} \tag{A.3}$$

where

$$\boldsymbol{P} = \mathrm{diag}\{\sigma^2(0), \sigma^2(1), \cdots, \sigma^2(M-1)\}, \tag{A.4}$$

$$\boldsymbol{D} = N \cdot \mathrm{diag}\{2\boldsymbol{P}^{-1}, 2\boldsymbol{P}^{-1}, \boldsymbol{P}^{-2}\}, \tag{A.5}$$

$$\boldsymbol{V} = \frac{2\pi LKN(N-1)}{N_\mathrm{s}} \cdot [-\boldsymbol{R}_I^T\boldsymbol{P}^{-1} \quad \boldsymbol{R}_R^T\boldsymbol{P}^{-1} \quad \boldsymbol{0}_M^T], \tag{A.6}$$

with $\boldsymbol{R}_R$ and $\boldsymbol{R}_I$ denoting the real and imaginary parts of $\boldsymbol{R}$ and

$$\beta = \frac{4\pi^2L^2K^2N(N-1)(2N-1)}{3N_\mathrm{s}^2} \,. \tag{A.7}$$

The Cramér-Rao bound is given by

$$CRB_\epsilon = [\boldsymbol{F}^{-1}]_{3M+1,3M+1} \,. \tag{A.8}$$

Similar to Eq. (47) in [119], for our case, we obtain

$$\boldsymbol{b} = \alpha \begin{bmatrix} \boldsymbol{R}_I^T & -\boldsymbol{R}_R^T & \boldsymbol{0}_M^T & \dfrac{3N_\mathrm{s}}{\pi LK} \end{bmatrix} \tag{A.9}$$

as the last column of $\boldsymbol{F}^{-1}$, where

$$\alpha = \frac{N_\mathrm{s}}{2\pi LKN(N-1)(4N-3)\boldsymbol{R}^H\boldsymbol{P}^{-1}\boldsymbol{R}} \,. \tag{A.10}$$

Substituting Eq. (A.9) to Eq. (A.8) and simplifying, we get

$$CRB_\epsilon = \frac{3N_\mathrm{s}^2}{2\pi^2L^2K^2N(N-1)(4N-3)\boldsymbol{R}^H\boldsymbol{P}^{-1}\boldsymbol{R}} \,. \tag{A.11}$$

Given that

$$\boldsymbol{R}^H \boldsymbol{P}^{-1} \boldsymbol{R} = \sum_{m=0}^{M-1} \frac{|R(m)|^2}{\sigma^2(m)} = M\Psi, \tag{A.12}$$

substituting Eq. (A.12) to Eq. (A.11), we obtain the final expression for the Cramér-Rao bound given in Eq. (4.13).